

PULSE FORMATION AND FREQUENCY CONVERSION IN  
DISPERSION-ENGINEERED NONLINEAR WAVEGUIDES AND RESONATORS

A DISSERTATION  
SUBMITTED TO THE DEPARTMENT OF ELECTRICAL ENGINEERING  
AND THE COMMITTEE ON GRADUATE STUDIES  
OF STANFORD UNIVERSITY  
IN PARTIAL FULFILLMENT OF THE REQUIREMENTS  
FOR THE DEGREE OF  
DOCTOR OF PHILOSOPHY

Marc Jankowski

August 2020

© 2020 by Marc P Jankowski. All Rights Reserved.

Re-distributed by Stanford University under license with the author.



This work is licensed under a Creative Commons Attribution-Noncommercial 3.0 United States License.

<http://creativecommons.org/licenses/by-nc/3.0/us/>

This dissertation is online at: <http://purl.stanford.edu/fc692xm6381>

I certify that I have read this dissertation and that, in my opinion, it is fully adequate in scope and quality as a dissertation for the degree of Doctor of Philosophy.

**Martin Fejer, Primary Adviser**

I certify that I have read this dissertation and that, in my opinion, it is fully adequate in scope and quality as a dissertation for the degree of Doctor of Philosophy.

**Robert Byer**

I certify that I have read this dissertation and that, in my opinion, it is fully adequate in scope and quality as a dissertation for the degree of Doctor of Philosophy.

**Olav Solgaard**

I certify that I have read this dissertation and that, in my opinion, it is fully adequate in scope and quality as a dissertation for the degree of Doctor of Philosophy.

**Jelena Vuckovic**

Approved for the Stanford University Committee on Graduate Studies.

**Stacey F. Bent, Vice Provost for Graduate Education**

*This signature page was generated electronically upon submission of this dissertation in electronic format. An original signed hard copy of the signature page is on file in University Archives.*

# Abstract

Recent advances in nonlinear photonics have enabled a new class of broadband ultra-stable light sources known as optical frequency combs. These light sources have given rise to a dizzying array of new optical devices and systems, spanning applications such as spectroscopy, astronomy, remote sensing, frequency synthesis, attoscience, telecommunications, and optical clockwork. At this time, there are a number of unsolved problems within the field. Optical frequency combs are often constrained to wavelengths within the near-infrared (NIR) due to the limited variety of mature laser gain media and host glasses, and many applications such as spectroscopy, sensing, and attoscience would benefit from the development of optical frequency combs at longer wavelength ranges such as the mid-infrared (MIR), which spans wavelengths from 2 to 20  $\mu\text{m}$ . Furthermore, the generation and stabilization of frequency combs often requires rather complicated nonlinear optical systems, which have prevented these light sources from being used outside of dedicated optics labs.

Ultrafast nonlinear dynamics is at the heart of all of these systems, with traditional approaches to comb generation relying on self-phase modulation in devices with cubic ( $\chi^{(3)}$ ) nonlinearities. While the operating regimes of  $\chi^{(3)}$  devices can be controlled by a suitable choice of waveguide group velocity dispersion, such devices are ultimately limited to soliton formation, supercontinuum generation, and, in phase-velocity engineered waveguides, non-degenerate four-wave mixing. In the context of frequency combs, soliton formation and supercontinuum generation are used to produce short pulses of light and broaden their associated optical bandwidth.

This dissertation considers new approaches to frequency comb generation based on recently discovered nonlinear dynamical processes in quasi-phasematched (QPM) devices with quadratic ( $\chi^{(2)}$ ) nonlinearities. In contrast with  $\chi^{(3)}$  nonlinearities, a broader range of nonlinear processes can be accessed in periodically poled  $\chi^{(2)}$  devices, where the desired process can be quasi-phasematched by lithographically patterning the  $\chi^{(2)}$  coefficient of the nonlinear medium. These processes include second harmonic generation (SHG), sum- and difference-frequency generation (SFG and DFG, respectively), optical parametric amplification (OPA), optical parametric oscillation (OPO), and optical rectification. A recurring theme is that the interplay of nonlinear optical effects, such as optical parametric amplification and self-phase modulation, with linear optical effects, such as dispersion, can produce qualitatively new dynamical regimes. In many cases, these dynamical regimes exhibit

favorable features that potentially solve the problems discussed above. The first half of this thesis considers the pulse formation mechanisms present in optical parametric oscillators (OPOs), and discusses new operating regimes that enable the generation of MIR combs with substantially more bandwidth than the NIR comb used to drive the OPO. These devices can produce few-cycle pulses with conversion efficiencies exceeding 50% while also preserving the coherence of the frequency comb. The latter portion of this thesis studies the dynamics of femtosecond pulses in quasi-phasematched nanophotonic waveguides. Here, the geometric dispersion associated with sub-wavelength confinement be used to achieve long interaction lengths with femtosecond pulses. Using these effects we are able to achieve saturated SHG with femtojoules of pulse energy, where state-of-the-art devices previously used picojoules. In the limit of phase-mismatched SHG driven with picojoules of pulse energy we observe the formation of a coherent multi-octave supercontinuum comprised of multiple spectrally broadened harmonics. The mechanisms of spectral broadening in this system are shown to be completely unique to dispersion-engineered nanophotonic QPM devices and exhibit a number of desirable features including i) low power requirements, ii) fewer decoherence mechanisms than traditional approaches, and iii) the formation of carrier-envelope-offset beatnotes in the regions of spectral overlap between the harmonics.

# Acknowledgments

This work would not have been possible without the extraordinary amount of support I have received during my years at Stanford.

First and foremost, I want express my gratitude towards my research adviser, Professor Martin M. Fejer. Marty has an incredible breadth and depth of knowledge, spanning the full spectrum from theory to experiment. He has given me the freedom to pursue a wide variety of projects, and he has always been able to offer me guidance, insight, and new ideas. More importantly, he has been a great model for *how* to think, and I can say with confidence I now approach problem solving rather differently than when I arrived at Stanford.

I am also grateful to the members of my reading committee and orals committee: Professors Robert L. Byer, Jelena Vuckovic, Shanhui Fan, Olav Solgaard, and my committee chair, Brian Cantwell. I greatly value the time you've taken to provide meaningful feedback on this work.

My thesis would not have been the same without the mentorship of Alireza Marandi. In many ways, Alireza was like a second advisor to me throughout the course of my thesis work. I learned a great deal about experimental nonlinear optics during our years working closely together in the lab. Perhaps more importantly, Alireza taught me the importance of putting my work in context. Science never happens in a vacuum, and building connections between your work and the interests of the broader scientific community is an often subtle art.

Chris Phillips has taught me an extraordinary amount about ultrafast nonlinear optics, and I deeply appreciate his mentorship. The work I have pursued throughout my thesis largely follows in his footsteps, and his thoughtful, rigorous, and intuitive approach to nonlinear optics cannot be found in any textbook. I always look forward to the next time we can get stuck in traffic after a conference and spend an hour discussing new ideas.

I had the pleasure of being Prof. Robert L. Byer's teaching assistant for EE 236a: Modern Optics from 2014 - 2016. This was an extraordinary opportunity to learn how to teach from one of the giants in our field, and over the course of those years I got the opportunity to lecture most of the material in the class. It is often said that the best way to learn a topic is to teach it, and the many conversations I've had with the students over the years, in addition to Bob's mentorship, have given me a much deeper foundation of optics knowledge than I would have gotten otherwise.

This work would not have been possible without my friends and co-workers in the Byer-Fejer community. Carsten Langrock, Ken Leedle, and Karel Urbanek have all taught me how to build setups that actually work, and all of my experimental results were made possible with their borrowed time and equipment. Carsten and Alireza first developed the poling recipes for thin film lithium niobate, which made possible all of the work found in the second half of this thesis. More recently, Jatadhari Mishra is carrying the torch both with respect to poling thin films and developing new dispersion-engineered devices, and I look forward to seeing his progress. Vahid Esfandyarpour, Yuwei Lin, and Derek Chang all helped me get up and running in the Fejer lab during my first few years, and they were always available to answer my many questions.

I've had the luck of being involved in a number of fruitful collaborations. Our work with Marko Lončar's group yielded the first periodically poled lithium niobate nanophotonics, and our groups have a number of ongoing projects that aim to push ultrafast nonlinear optics to new dynamical regimes. Cheng Wang and Mian Zhang developed the first low-loss lithium niobate nanophotonic devices, which made all of the successive work in our collaboration possible. Boris Desiatov fabricated all of the waveguides used in our work on ultrafast devices and was able to fabricate devices with rather stringent fabrication tolerances.

In parallel, we've been pursuing a number of projects with Amir Safavi-Naeini's group, including a new platform for nanophotonic devices that can be used to generate MIR light. It's been a pleasure to work with Amir, and his students Timothy McKenna, Hubert Stokowski, and Jason Herrmann. They have all made remarkable progress in developing nanophotonic devices in multiple platforms, and I look forward to seeing these results come out in the literature.

The members of the Mabuchi lab have always been extremely helpful in understanding the quantum optical behavior associated with nonlinear photonic devices and in developing intuitive models of complicated systems. I am very grateful for the late nights discussing potential next generation devices with Tatsuhiro Onodera, Edwin Ng, and Ryotatsu Yanagimoto. They have developed a number of new techniques that can shine light on the complicated quantum behavior of extremely nonlinear waveguides. I also had the pleasure of working on models of the dynamical behavior of optical parametric oscillators (OPOs) with Ryan Hamerly. I learned a great deal about model reduction from Ryan, and the manifold projection approach used to describe the behavior of OPOs that form temporal solitons were one of the many techniques that he developed.

I also worked with Léonard Krueger and Valentin Wittwer in Ursula Keller's group and Thomas Suedemeyer's group, respectively. We worked together with Chris to develop chip-integrated synchronously pumped OPOs based on their recently developed 10-GHz modelocked laser. I was truly impressed by the knowledge, talent, and skill shared by everyone in these labs, and I look forward to our ongoing work together.

Finally, I would like to thank my friends and family. I am lucky to have an incredible community whose support over the years has made me who I am. It would be truly impossible to convey the

depth of my appreciation here. Instead of thanking anyone individually, at the risk of omitting many people who mean a great deal to me, I will simply say: thank you for being in my life.

# Contents

|   |           |
|---|-----------|
| <b>Abstract</b>   | <b>iv</b> |
| <b>Acknowledgments</b>  | <b>vi</b> |
| <b>1 Introduction</b>   | <b>1</b>  |
| 1.1 Short Pulses and Optical Frequency Combs . . . . .              | 1         |
| 1.1.1 Short Optical Pulses . . . . .                                | 2         |
| 1.1.2 Optical Frequency Combs . . . . .                             | 3         |
| 1.1.3 Sources and Applications of Optical Frequency Combs . . . . . | 6         |
| 1.1.4 Linear Propagation of Short Pulses . . . . .                  | 7         |
| 1.2 The Coupled Wave Equations . . . . .                            | 8         |
| 1.2.1 Plane-wave Second Harmonic Generation . . . . .               | 9         |
| 1.2.2 Quasi-phasematching . . . . .                                 | 11        |
| 1.3 Canonical Solutions to the Coupled Wave Equations . . . . .     | 12        |
| 1.3.1 Phase-matched Second harmonic Generation . . . . .            | 12        |
| 1.3.2 Phase-mismatched Second Harmonic Generation . . . . .         | 14        |
| 1.3.3 The Bandwidth of Second Harmonic Generation . . . . .         | 16        |
| 1.4 Nonlinear Pulse Propagation . . . . .                           | 17        |
| 1.4.1 Second Harmonic Generation with Short Pulses . . . . .        | 17        |
| 1.4.2 The Nonlinear Schrödinger Equation . . . . .                  | 19        |
| 1.4.3 f-2f Interferometry . . . . .                                 | 22        |
| 1.5 Numerical Modeling of Nonlinear Interactions . . . . .          | 23        |
| 1.6 Overview of this Dissertation . . . . .                         | 25        |
| <b>2 Synchronously Pumped Optical Parametric Oscillators</b>        | <b>27</b> |
| 2.1 The Theory of Degenerate OPOs . . . . .                         | 28        |
| 2.1.1 Degenerate Operation . . . . .                                | 29        |
| 2.1.2 Frequency Combs in Degenerate OPOs . . . . .                  | 31        |
| 2.1.3 Asynchronous Pumping . . . . .                                | 32        |

|          |  |            |
|----------|--|------------|
| 2.1.4    | High Order Dispersion and the Transition to Non-degeneracy . . . . . | 36         |
| 2.2      | Pulse Formation in OPOs . . . . .                                    | 40         |
| 2.2.1    | Box Pulse Theory . . . . .   | 40         |
| 2.2.2    | Temporal simultons in Optical Parametric Oscillators . . . . .       | 43         |
| 2.3      | OPO Design and Experiment . . . . .                                  | 48         |
| 2.3.1    | OPO Design . . . . .   | 49         |
| 2.3.2    | Experimental Results . . . . .                                       | 51         |
| 2.4      | Numerical Simulations . . . . .                                      | 55         |
| 2.5      | The Bandwidth and Stability Limits of OPOs . . . . .                 | 58         |
| 2.6      | Outlook and Future Work . . . . .                                    | 59         |
| <b>3</b> | <b>Nonlinear Nanophotonic Devices</b>                                | <b>61</b>  |
| 3.1      | The Coupled Wave Equations in Nonlinear Waveguides . . . . .         | 62         |
| 3.2      | Nanophotonic PPLN Waveguides . . . . .                               | 65         |
| 3.3      | Pulsed Second Harmonic Generation . . . . .                          | 70         |
| 3.4      | Cascaded Nonlinearities in Nanophotonic PPLN Devices . . . . .       | 75         |
| 3.5      | Supercontinuum Generation . . . . .                                  | 76         |
| 3.6      | Saturation Broadening in Nanophotonic PPLN Devices . . . . .         | 80         |
| 3.7      | Conclusions and Outlook . . . . .                                    | 84         |
| <b>4</b> | <b>Conclusions</b>   | <b>86</b>  |
| 4.1      | Summary of this Dissertation . . . . .                               | 86         |
| 4.2      | Future Work . . . . .  | 87         |
| <b>A</b> | <b>The Coupled Wave Equations for Gaussian Beams</b>                 | <b>90</b>  |
| A.1      | Gain Induced Diffraction in OPOs . . . . .                           | 93         |
| <b>B</b> | <b>A Brief Review of Optical Waveguide Theory</b>                    | <b>95</b>  |
| B.1      | The Coupled Wave Equations in Nonlinear Waveguides . . . . .         | 100        |
|          | <b>Bibliography</b>  | <b>104</b> |

# List of Tables

2.1 Phase deviations due to higher order dispersion of the cavity mirrors . . . . . 50

# List of Figures

|     |   |    |
|-----|---|----|
| 1.1 | Example of a frequency comb with a repetition period of 5-ns, a sech-pulse envelope with $\tau = 250$ ps, and an absolute frequency of 2.066 GHz. While the low carrier frequency shown here cannot occur in an optics experiment, these parameters are useful for illustrating the characteristic features of a frequency comb. a) The pulse train in the time domain, showing the field envelope given by $\sum_m A_\omega(t + mT_R)$ (dotted orange line), and the instantaneous electric field $E(t)$ (solid blue line). After two pulses, the peak of the carrier has drifted from the peak of the envelope by a phase shift $2\phi_{\text{ceo}}$ . b) The Fourier transform, $\hat{\mathcal{E}}(f - f_0)$ showing discrete frequencies separated by $f_R = 1/T_R$ (solid blue lines), which sample the field envelope $\hat{A}_\omega(f - f_0)$ . The frequency comb does not intersect DC ( $f = 0$ ), but instead has a small RF offset, $f_{\text{ceo}} = f \bmod f_R$ . . . . . | 4  |
| 1.2 | The absorption spectrum of some common molecules potentially used for medical diagnostics, and their overlap with the light sources considered here. GaP can produce wavelengths as long as 10- $\mu\text{m}$ , and GaAs can produce wavelengths as long as 20- $\mu\text{m}$ . . . . .   | 6  |
| 1.3 | The conversion efficiency from fundamental to second harmonic as a function of $z$ for saturated (solid blue) and unsaturated (dotted grey) SHG. 100% conversion in the unsaturated limit corresponds to 60% conversion when pump depletion is accounted for. . . . .   | 13 |
| 1.4 | a) The power in the fundamental (green) and second harmonic (blue) as a function of $z$ for fixed $\Delta k$ . The nonlinear phase (orange) may be approximated by an average Kerr effect, $\phi_{\text{NL}} = -\eta_0 z / \Delta k$ (grey line). b) The SHG conversion efficiency (solid blue) as a function of $\Delta k$ for fixed device length $L$ , showing a $\text{sinc}^2(\Delta k L / 2)$ transfer function. The effective Kerr nonlinearity (solid orange) is well approximated by $\gamma_{\text{SPM}} = -\eta_0 / \Delta k$ (dotted grey) for devices longer than two coherence lengths. . . . .   | 15 |

|     |   |    |
|-----|---|----|
| 1.5 | The two bandwidths associated with SHG. a) The total generated second harmonic bandwidth, $\Omega_{\text{FW}}$ , is limited by $\Delta k'$ . The height of the $\text{sinc}^2$ function at $2\omega + 2\Omega$ denotes the reduction in SHG due to filtering by the SHG transfer function. b) The amount of fundamental bandwidth that can contribute to SHG, $\Omega'_{\text{FW}}$ , is limited by $k''_{\omega}$ . Here, the height of the $\text{sinc}^2$ transfer function denotes a reduced response at $2\omega$ to SFG of the two frequencies at $\omega \pm \Omega'$ . . . . .  | 17 |
| 1.6 | a) Evolution of the pulse shape, $ A_{\omega}(z, t) ^2$ , for an $N = 2$ soliton. The envelope evolves periodically, and compresses to a pulse with a four-fold increase in the peak power every half-period. b) The input soliton (blue) compared to the compressed pulse (orange). . . . .  | 21 |
| 1.7 | f-2f interferometry. a) A short pulse from a modelocked laser is broadened to an octave using supercontinuum generation in a tightly confining waveguide. Orange curve: pulse shape, blue curve: power spectral density. b) After soliton fission the pulse has broken up into several frequency shifted solitons, with a combined spectrum that spans a coherent octave. c) The long-wave portion of the spectrum passes through a long pass filter (LPF), and is delayed. d) The long wavelengths are recombined with the supercontinuum, passed through an SHG crystal, and absorbed by a photodetector (PD). e) Interference between the short wavelengths and the frequency-doubled long wavelengths produces a photocurrent that oscillates at $f_{\text{ceo}}$ . . . . . | 22 |
| 2.1 | Schematic of a typical OPO. A bright pump at $2\omega$ provides gain to a signal at $\omega$ in a nonlinear crystal (PPLN). The signal is partially out-coupled through (M4), with the rest fed back to the nonlinear crystal. M1 has $\sim 100\%$ transmission at the pump wavelength, which out-couples any leftover pump on each round trip. . . . .   | 28 |
| 2.2 | a) Schematic of fundamental comb formed by degenerate OPA. In principle, this process allows for the formation of comb lines with frequencies spaced by $f_R/2$ . b) In the presence of a synchronously pumped cavity, the signal comb is filtered to have the same repetition frequency as the pump. c) Detuning the cavity by half of a free spectral range brings the second frequency comb into resonance. As a result, synchronously pumped OPOs exhibit resonances when the cavity length is detuned by a pump wavelength, not a signal wavelength. . . . .   | 31 |

|     |   |    |
|-----|---|----|
| 2.3 | The role of asynchronization in a degenerate OPO. On the first round trip, a signal pulse initially forms such that it experiences symmetric temporal walk-off from the pump. a) Before the nonlinear crystal, the signal is delayed from the pump by $\Delta k' L/2$ . We note here that a signal on the left corresponds to earlier time, and therefore pulses with higher group velocities move left relative to the others. b) After the nonlinear crystal, the signal is amplified and has a group advance relative to the pump due to temporal walk-off with $\Delta k' > 0$ , which corresponds to $v_{g,s} > v_{g,p}$ . c,d) On the next round trip, the signal acquires a relative delay of $\Delta T_{RT}$ everywhere in the cavity, and now experiences less gain. . . . . | 33 |
| 2.4 | Illustration of the gain clipping function associated with a flat-top pump pulse. In this example, we consider a train of finely spaced signal pulses to better visualize the gain as a function of relative time delay. As the pump walks through the train of signal pulses they are amplified according to Eqn. 2.9. The pulse peaked at $t = 0$ corresponds to the case of symmetric temporal walk-off and experiences the largest field gain. . . . .  | 34 |
| 2.5 | a) Comparison of $\Gamma(L, t)$ for a flat-top pulse (orange) and a sech pulse (blue). The parameters chosen are $\Delta k' L = T_p = 100$ fs, and $\tau = 40$ fs, which corresponds to FWHM pulse duration of 70 fs. This choice of parameters corresponds to the experimental conditions studied in Sec. 2.3. b) The same comparison for $-\tau < t < \tau$ , which shows that $\Gamma(L, t)$ varies slowly for delays comparable to $\tau$ . . . . .   | 36 |
| 2.6 | The OPO eigenvalue, plotted for a) $\gamma_0 L = 0.8$ and b) an extreme limit, $\gamma_0 L = 5$ . The OPO has $k''_{\omega} L = -53$ fs <sup>2</sup> , $\phi''_c = 25$ fs <sup>2</sup> , $\lambda_p = 1045$ nm, and $R = 35\%$ . Dotted lines denote the resonance conditions, Eqn. 2.17 and Eqn. 2.18, respectively. . . . .   | 38 |
| 2.7 | 3-dB bandwidth of $\lambda_+(0)$ as a function of unsaturated OPA gain for the three cavity designs described in the text. Half-compensated cavities with $\phi''_c = -\phi''_x/2$ achieve the most bandwidth for $1 < \gamma_0 L < 4$ . . . . .  | 39 |
| 2.8 | Pulse formation in an OPO with competition between saturation and gain clipping as the dominant pulse formation mechanisms. a) Pulse shape $\bar{A}_s^2(t, p)$ according to Eqn. 2.26, and b) the power spectral density for various times above threshold. For the plots shown here $R = 35\%$ , and $T_p = 1$ ps. We note that the pulse duration grows larger and loses bandwidth with increasing times above threshold, $p$ , defined in the text above Eqn. 2.27. . . . .  | 41 |

|      |   |    |
|------|---|----|
| 2.9  | The role of cavity length detuning in pulse formation. a) Pulse shape $\bar{A}_s^2(t, \ell)$ , and b) the power spectral density for various cavity length detunings. The plots shown have the same parameters as Fig. 2.9, but with the times above threshold fixed at $p = 1.5$ , and with a crystal and cavity group delay dispersion of $k''_\omega L = -53 \text{ fs}^2$ and $\phi''_c = 25 \text{ fs}^2$ , respectively. For $\ell > 0$ , the OPO transitions to nondegenerate operation. We note here that the pump pulse duration of 1 ps was chosen to produce a small bandwidth, such that the frequency splitting for $\ell > 0$ is easily visualized. . . . . | 43 |
| 2.10 | A temporal soliton. The bright sech soliton (blue) at frequency $\omega$ walks through the undepleted $2\omega$ pump (green). The signal depletes the pump, forming a co-propagating tanh dark soliton, and leaving behind a tail of phase-flipped pump. We note here that the signal walks off to the left, since higher velocities correspond to moving earlier in time. . . . .  | 44 |
| 2.11 | Evolution of pump and signal fields in an OPA from the linear to the soliton regimes. a) In the unsaturated regime, the signal initially experiences linear parametric gain. b) Upon reaching the soliton energy, the signal saturates the pump and the pair form a soliton. c) The soliton propagates without extracting any additional gain, but accumulates a total group advance $\Delta T$ due to the increased group velocity of a soliton. Dotted line: the evolution of the signal field undergoing linear temporal walkoff. . . . .  | 45 |
| 2.12 | Soliton formation in a synchronously pumped OPO cavity. (a-b) Displacement of intracavity signal relative to a perfectly synchronous half-harmonic pulse undergoing linear propagation (dotted lines) (a) After M1 the signal acquires a small delay, $\Delta T_{\text{RT}}$ , relative to the incoupled pump due to the timing mismatch. (b) After optical parametric amplification the signal acquires a nonlinear shift in group delay $\Delta T$ due to soliton formation, which compensates the timing mismatch $\Delta T_{\text{RT}}$ . . . . .   | 47 |
| 2.13 | Design of the synchronously pumped OPOs used throughout this chapter[27, 60]. Pump pulses are in-coupled through M1, and the generated signal is out-coupled through M4. Mirrors M2 and M3 focus the pump and resonant signal into the PPLN crystal resulting in $1/e^2$ beam-waists of 10- $\mu\text{m}$ and 14- $\mu\text{m}$ , respectively. Cavity length adjustments are made by mounting M1 on a piezo stage. . . . .   | 48 |
| 2.14 | (Solid Line) The net reflection coefficient of the passive cavity optics and (Dotted Line) the associated group delay dispersion. . . . .   | 49 |
| 2.15 | a) The $1/e^2$ beam radius in the nonlinear crystal as a function of mirror separation and angle. Each angle is offset for clarity, and the cavity achieves a symmetric Gaussian beam for $\theta = 5^\circ$ . Blue: sagittal, orange: transverse. b) The beam waist associated with the fundamental and second harmonic as a function of mirror separation for a $5^\circ$ angle of incidence. . . . .   | 50 |

|      |  |    |
|------|--|----|
| 2.16 | a) The conversion efficiency as a function of cavity length detuning for 550 mW of pump power. Each peak is labeled with $\ell$ relative to the peak with lowest threshold. b) The conversion efficiency of each peak as a function of pump power. Peaks with $\ell = 1$ and $\ell = 2$ exhibit larger slope efficiencies and overall conversion efficiencies than the synchronous resonance. c) The power spectral density as a function of cavity length detuning. The synchronous resonance exhibits box-pulse behavior and transitions from degenerate to non-degenerate operation as the cavity is detuned through $\ell = 0$ . Resonances with $\ell > 0$ only exhibit degenerate operation. . . . . | 52 |
| 2.17 | Power spectra recorded as a function of pump power for a) peak 0 and b) peak +1. Each curve is labeled with the corresponding pump power used in the experiment, with arrows denoting the 3dB bandwidth. c) The scaling with pump power of the transform limited pulsewidth (3 dB) for peaks 0-2, computed from spectra such as those shown in a-b. For large powers, peak 0 shows an increase in pulsewidth in accordance with Eqn. 2.28, while peaks +1 and +2 show a monotonic decrease in pulsewidth, in accordance with Eqn. 2.38. . . . .  | 53 |
| 2.18 | Carrier-envelope-offset detection of the pump comb and OPO. a,b) The overlap of the pump SCG with the parasitic SFG at 700 nm and with the OPO spectrum around 1600-nm, respectively. c) The resulting $f_{ceo}$ beatnotes, $f_0^{2\mu m}$ and $f_0^{2\mu m} - f_0^{1\mu m}$ . d) $f_0^{2\mu m}$ as a function of $f_0^{1\mu m}$ , showing that a degenerate OPO achieves intrinsic frequency locking. Adapted from [27]. . . . .  | 54 |
| 2.19 | Comparison of simulation results to experiment. a) Simulated conversion efficiency (solid color lines) compared to experimental data (filled circles). Grey circles denote non-degenerate operation. b) Experimental and c) simulated power spectral density as a function of cavity length detuning. . . . .  | 56 |
| 2.20 | (a) Simulated evolution of the intracavity pulse intensity over many round trips for $\Delta T_{RT} = -3.5$ fs showing the interference of a distinct signal and idler. The dotted line denotes the trajectory of a linearly propagating half-harmonic signal pulse. (b) Pulse evolution for $\Delta T_{RT} = 0$ fs showing the formation of a half-harmonic pulse synchronized to the pump repetition rate. (c) Simulated pulse evolution for $\Delta T_{RT} = 7$ fs showing the formation of a half-harmonic pulse which, upon depleting the pump, is able to accelerate forward in time and synchronize to the pump repetition rate. . .  | 57 |
| 3.1  | Schematic of typical ridge waveguide, with the associated electric field $E_{x,\mu}$ of the waveguide mode for both the fundamental (left) and second harmonic (right). The top cladding is air, the etched thin film is X-cut MgO:LN, and we approximate the 2- $\mu$ m-thick silica adhesion layer as extending to infinity. . . . .   | 63 |

|     |   |    |
|-----|---|----|
| 3.2 | a) and b) Mode profiles ( $e_{\mu,Z}$ ) at 1550 nm and 775 nm, respectively. Here, $X$ and $Z$ denote the crystal axes of the MgO:LN thin film. c) Numerically calculated quasi-phasematching period (black) and theoretical conversion efficiency (blue) as a function of wavelength for a typical thin-film PPLN waveguide. Figure adapted from [83] . . . . .  | 66 |
| 3.3 | a) Schematic of the poling process, resulting in high fidelity domain inversion with a $\sim 50\%$ duty cycle. b) Waveguides are patterned using an $\text{Ar}^+$ assisted dry etch, resulting in smooth sidewalls. c) The samples are prepared using laser dicing, resulting in optical-quality end-facets. . . . .  | 67 |
| 3.4 | a) Schematic of the characterization setup. b) Measured SHG conversion efficiency versus pump wavelengths for two waveguides with the same poling period but different top widths. (c) Zoom-in view of the SHG spectral response of the 1440-nm-wide device (solid curve), together with the theoretically predicted responses. The green dotted and blue dashed curves correspond to the ideal and corrected transfer functions, respectively. Inset shows a CCD camera image of the scattered SHG light at the output waveguide facet. TLS, tunable laser source; EDFA, erbium-doped fiber amplifier; FPC, fiber polarization controller; OSA, optical spectrum analyzer. . . . . | 68 |
| 3.5 | SHG conversion efficiency as a function of input power in the saturated limit. Inset shows the conversion efficiency in the undepleted limit. . . . .   | 69 |
| 3.6 | a) Waveguide cross-section, showing the normalized electric field associated with the simulated $\text{TE}_{00}$ fundamental (above) and second harmonic (below) modes. The waveguides shown here correspond to a top width of 1850 nm, an etch depth of 350 nm, and a starting film thickness of 700 nm. b,c) Simulated poling period and normalized efficiency, respectively, as a function of waveguide geometry. d,e) Simulated $\Delta k'$ and $k''$ , respectively. The solid black line denotes $\Delta k' = 0$ , and the dashed black contour line shows geometries that achieve $ \Delta k'  < 5\text{fs/mm}$ . . . . .  | 71 |
| 3.7 | SEM image of one of the fabricated waveguides. . . . .  | 72 |
| 3.8 | a) Schematic of experimental setup. ND- variable neutral density filter, OBJ- reflective objective lens, OSA- optical spectrum analyzer. b,c) Measured spectrum of the driving polarization ( $ A_{\omega}(0, \Omega) * A_{\omega}(0, \Omega) ^2$ ) and output second harmonic ( $ A_{2\omega}(L, \Omega) ^2$ ), respectively. d) Measured SHG transfer function (black) for a 6-mm-long nanophotonic waveguide, showing good agreement with theory (blue). The bandwidth of these waveguides exceeds that of bulk PPLN (orange) by more than an order of magnitude. . . . .  | 74 |
| 3.9 | SHG conversion efficiency and pump depletion as a function of input pulse energy, showing 50% conversion efficiency with an input pulse energy of 60-fJ. Inset: Undepleted regime with fit given by Eqn. (3.9) and a heuristic model for saturation, as described in the text. . . . .  | 75 |

|      |  |    |
|------|--|----|
| 3.10 | a) Evolution of power spectral density over an order of magnitude variation of pulse energy. Adjacent traces are displaced by 30 dB for clarity. The different noise floors correspond to the three spectrometers used, and dotted lines have been added to guide the eye where discontinuities in these noise floors are present. b) Photograph of supercontinuum produced with 11-pJ input to the waveguide. . . . . | 76 |
| 3.11 | Measured carrier-envelope-offset beatnotes for three different values of intracavity dispersion in the laser used to pump the OPO. . . . .   | 77 |
| 3.12 | Power spectral density output from the chip as a function of input pulse energy a) Experiment, b) Simulation. The power in dBm is measured in 2-nm-wide spectral bins.   | 78 |
| 3.13 | Simulated coherence of the fundamental and second harmonic generated by a 4-pJ pulse, showing $ g^{(1)}  \sim 1$ . . . . .   | 79 |
| 3.14 | Theoretical evolution of a) the fundamental, $ A_\omega ^2$ and b) the second harmonic $ A_{2\omega} ^2$ . Dotted lines show the in-coupled fundamental pulse, and solid lines show the resulting pulse at the output of the waveguide for each harmonic. . . . .  | 80 |
| 3.15 | Comparison of theory with a full split-step Fourier simulation. a) Theoretical fundamental, b) theoretical second harmonic, c) simulated fundamental, and d) simulated second harmonic. . . . .  | 81 |
| 3.16 | Theoretical phase of a) the fundamental and b) the second harmonic. The fundamental forms plateaus of $\sim$ constant phase in time, and the second harmonic exhibits a phase that is independent of time. . . . .   | 82 |
| 3.17 | Comparison of a) theoretical and b) experimental power spectral density for phase-mismatched SHG in the saturated limit. . . . .   | 83 |
| 3.18 | Beatnote photocurrent as a function of wavelength and pulse energy coupled into the waveguide. For in-coupled pulse energies of 3-, 3.5-, and 4-pJ, the generated beatnotes remain in-phase across 100's of nm of bandwidth. . . . .   | 84 |
| B.1  | Schematic of typical ridge waveguide studied in Ch. 3, with the associated electric field $E_{x,\mu}$ of the waveguide mode for both the fundamental (left) and second harmonic (right). The top cladding is air, the etched thin film is X-cut MgO:LN, and we approximate the 2- $\mu$ m-thick silica adhesion layer as extending to infinity. . . . .  | 95 |

# Chapter 1

## Introduction

The purpose of this chapter is to serve as a review of the fundamental concepts used throughout the following chapters. The primary goal of the devices developed here is to provide novel methods of generating, stabilizing, and frequency converting short pulses of light using nonlinear photonics. Naturally, we begin this chapter with a brief overview of the properties of short optical pulses, which we will use to drive nonlinear media. Then, we establish the concept of an optical frequency comb, which comprises a stable train of short optical pulses. The following sections will review the key concept in nonlinear optics, which will be the building blocks of the nonlinear systems studied in later chapters. We first introduce the coupled wave equations for second harmonic generation, both for continuous-wave (CW) lasers and then for short pulses, before briefly discussing the nonlinear Schrödinger equation. These equations will enable us to describe the propagation of short optical pulses in a wide variety of nonlinear photonic devices. In many cases, these equations can be solved exactly and will allow for simple analytic models of the devices under study. Even in the absence of analytic solutions, many of the limit cases will provide insights that yield simple heuristic design rules. We will close this chapter with a description of full numerical methods, which often exhibit excellent agreement with the observed behavior of nonlinear devices and provide a direct method of verifying our heuristic models.

### 1.1 Short Pulses and Optical Frequency Combs

All of the systems we consider here will be driven by short optical pulses. There are two reasons for this. First, the typical figure of merit for nonlinear processes, such as the efficiency of a frequency converter, or the amount of phase accumulated due to a nonlinear refractive index, increases with the intensity used to drive the nonlinear process. Therefore, the large instantaneous intensity that occurs around the peak of a short optical pulse can be used to achieve dynamical regimes that would otherwise be inaccessible to CW lasers. Second, many of the applications we hope to enable require

large optical bandwidths. This may be achieved either by producing a short optical pulse, which inherently has a large optical bandwidth, or by using a short pulse to drive a process known as supercontinuum generation (SCG). In this section, we will briefly give an overview of the properties of short pulses produced by lasers, both in the time domain and in the frequency domain. We then discuss commonly used sources of short pulses, before describing how they propagate in linear media.

### 1.1.1 Short Optical Pulses

We begin with a canonical example to establish the terminology used throughout the remainder of this chapter. We'll start by defining the electric field,  $E$ , and many convenient associated quantities, such as the field envelope,  $A_\omega$ . The electric field associated with a CW plane wave with frequency  $\omega$  propagating along  $z$  is given by

$$E(z, t) = \frac{1}{2} (E_0 \exp(i\omega t - ikz) + c.c.),$$

where *c.c.* denotes the complex conjugate. It's often convenient to throw away the complex conjugate and consider the evolution of  $\mathcal{E} = E_0 \exp(i\omega t - ikz)$ . We may then reconstruct the field using

$$E = \frac{1}{2} (\mathcal{E} + c.c.).$$

Similarly, we may continue to break this expression down by explicitly removing the carrier frequency to obtain the complex Fourier amplitude,

$$\mathcal{E} = \mathcal{E}_\omega \exp(i\omega t),$$

and remove the spatial dependence to find the complex field envelope,

$$\mathcal{E}_\omega = A_\omega \exp(-ikz).$$

For a CW plane wave,  $A_\omega = E_0$  is trivial. However, for many cases of interest, we will have  $A_\omega(z, t)$  that describes the evolution of a short pulse in space and time. It's often easiest to work with the field envelope, which varies slowly, and then build up to the electric field by reversing the steps taken above.

The simplest train of optical pulses is given by the superposition of two CW lasers with frequencies of  $\omega \pm \Delta\omega$ . For simplicity, we choose  $z = 0$ . In this case, the complex amplitude associated with the field is

$$\begin{aligned} \mathcal{E}(0, t) &= E_0 \exp(i(\omega + \Delta\omega)t) + E_0 \exp(i(\omega - \Delta\omega)t) \\ &= 2E_0 \cos(\Delta\omega t) \exp(i\omega t). \end{aligned}$$

There are two key behaviors in the above relationship: i) the peak amplitude, rather than the peak power, of the waves adds together. Therefore we expect a 4-fold, rather than a 2-fold reduction in the power requirements of many nonlinear optical processes. ii) If we again remove the carrier wave,  $\exp(i\omega t)$ , then the field envelope is  $A_\omega = 2E_0 \cos(\Delta\omega t)$ , where  $\omega \gg \Delta\omega$  by construction. Therefore, the envelope describes a variation of the pulse shape much slower than the carrier frequency, while the carrier wave describes rapid field oscillations associated with the mean frequency of the electric field. In this case, both the carrier wave and the envelope are time-periodic, with a carrier frequency given by  $f = \omega/2\pi = 1/T$  and repetition frequency given by  $f_R = \Delta\omega/2\pi = 1/T_R$ . Typical numbers for  $f$  and  $f_R$  are 300 THz and 100 MHz, respectively.

In the general case, we may construct a pulse train as the product of a carrier wave  $\exp(i\omega t)$  and a sum of envelopes  $\sum_{m=-\infty}^{m=\infty} A_\omega(t + mT_r)$ ,

$$\mathcal{E}(t) = \sum_{m=-\infty}^{m=\infty} A_\omega(t + mT_r) \exp(i\omega t), \quad (1.1)$$

such that the energy contained in a pulse is  $U = \int_0^{T_R} |\mathcal{E}_\omega(t)|^2 dt / (2Z_0) = \int_{-\infty}^{\infty} |A_\omega(t)|^2 dt / (2Z_0)$ , where  $Z_0$  is the impedance of free space. Typical examples of pulse envelopes found in the lab include  $A(t) \propto \sqrt{(\pi/2)^{1/2} U / \tau} \exp(-(t/\tau)^2)$  gaussian pulses such as those formed in AM-modelocked lasers and Q-switched lasers, and the  $A(t) \propto \sqrt{U/(2\tau)} \text{sech}(t/\tau)$  sech pulses such as those found in soliton-modelocked lasers and microresonators[1, 2]. For the systems under study here, typical values of  $\tau$  are on the order of 50-100 fs. When compared to a typical repetition period of  $T_R \sim 10$  ns, this corresponds to an enhancement of the peak power of a pulse by five orders of magnitude relative to the average power.

### 1.1.2 Optical Frequency Combs

We now consider the frequency-domain representation of a pulse train, which is referred to as an optical frequency comb when certain stability criteria are satisfied. The key insight of this section is that the electric field associated with a train of pulses only contains discrete frequencies. This seemingly straightforward result is the basis of the incredible variety of applications enabled by optical frequency combs[3]. Examples include spectroscopy[4, 5], astronomy[6], remote sensing[7], telecommunications[8], attoscience[9, 10], and optical clockwork[11].

If we define the Fourier transform of  $\mathcal{E}(t)$  as  $\mathcal{F}\{\mathcal{E}(t)\} = \hat{\mathcal{E}}(f) = \int_{-\infty}^{\infty} \mathcal{E}(t) \exp(-2\pi i f t) dt$ , then the Fourier transform of Eqn. 1.1 is given by

$$\hat{\mathcal{E}}(f) = \sum_m f_R \hat{A}_\omega(f - f_0) \delta(f - f_0 - m f_R), \quad (1.2)$$

where  $\hat{A}_\omega(f)$  is the Fourier transform of the field envelope  $A_\omega(t)$ ,  $\delta(f)$  is the Dirac delta function,

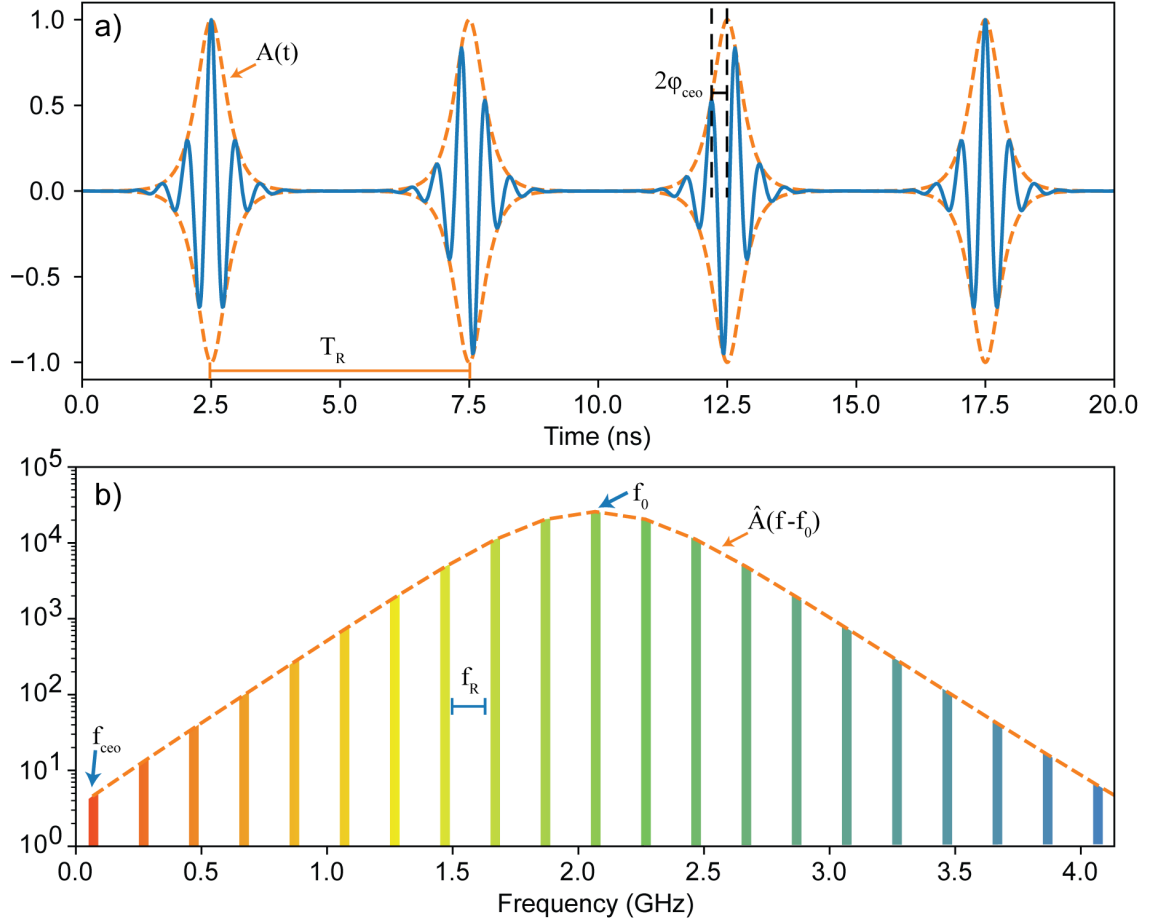


Figure 1.1: Example of a frequency comb with a repetition period of 5-ns, a sech-pulse envelope with  $\tau = 250$  ps, and an absolute frequency of 2.066 GHz. While the low carrier frequency shown here cannot occur in an optics experiment, these parameters are useful for illustrating the characteristic features of a frequency comb. a) The pulse train in the time domain, showing the field envelope given by  $\sum_m A_\omega(t + mT_R)$  (dotted orange line), and the instantaneous electric field  $E(t)$  (solid blue line). After two pulses, the peak of the carrier has drifted from the peak of the envelope by a phase shift  $2\phi_{\text{ceo}}$ . b) The Fourier transform,  $\hat{\mathcal{E}}(f - f_0)$  showing discrete frequencies separated by  $f_R = 1/T_R$  (solid blue lines), which sample the field envelope  $\hat{A}_\omega(f - f_0)$ . The frequency comb does not intersect DC ( $f = 0$ ), but instead has a small RF offset,  $f_{\text{ceo}} = f \bmod f_R$ .

and  $f_0 = \omega_0/2\pi$ . An example of Eqns 1.1-1.2 is shown in Fig. 1.1(a-b) for the case of sech pulse. The main result of Eqn. 1.2 is that the frequency domain representation of a pulse train comprises discrete frequencies given by  $f_m = f_0 + mf_R$  that sample  $\hat{A}_\omega(f - f_0)$  (Fig. 1.1(b)). We note here that for the case where  $f_0 T_R$  is an integer one may arrive at the same result by expanding  $\mathcal{E}(t)$  as a Fourier series, with the  $m^{\text{th}}$  series coefficient given by  $c_m = f_R \hat{A}_\omega(f_m - f_0)$ . In the general case, where  $f_0 T_R$  is not an integer, the peak of the carrier slips relative to the envelope pulses on each successive shot, which corresponds to a small phase shift of the comb that occurs on scales slower than the repetition period. This carrier-envelope phase delay, labeled  $\phi_{\text{ceo}}$  in Fig. 1.1(a), is given by  $\phi_{\text{ceo}} = 2\pi f_0 T_R \bmod 2\pi = 2\pi f_{\text{ceo}} T_R$ , or equivalently, the carrier-envelope offset frequency is given by  $f_{\text{ceo}} = f_0 \bmod f_R$  (Fig. 1.1(b)). The absolute frequency of the comb lines is determined equally well using  $f_R$  and either  $f_0$  or  $f_{\text{ceo}}$ , with both  $f_m = f_{\text{ceo}} + (m + m_0)f_R$  and  $f_m = f_0 + mf_R$  commonly seen in the literature, where  $f_0 = f_{\text{ceo}} + m_0 f_R$ . In many cases, the  $m_0$  is omitted. We note that the Fourier transform conventions defined here are for frequencies, in Hz, instead of the angular frequencies typically used in optics. We have adopted this convention for two reasons: i) frequency units (e.g. MHz for  $f_{\text{ceo}}$  and  $f_R$ ) are typically used in describing frequency combs, and ii) this convention renders the Fourier transform a unitary operator with  $\mathcal{F}\{\mathcal{F}\{\mathcal{F}\{\mathcal{E}(t)\}\}\} = \mathcal{F}^{-1}\{\mathcal{E}(t)\}$ , which is convenient in many contexts[12]. In Sec. 1.4, where we describe the propagation of short pulses, we will switch to using angular frequencies, as this notation is common, but we will leave the definition of the Fourier transform unchanged. Therefore, we will Fourier transform functions using  $\hat{\mathcal{E}}(f) = \int_{-\infty}^{\infty} \mathcal{E}(t) \exp(-2\pi i f t) dt$ , and evaluate  $\hat{\mathcal{E}}(\omega)$  by substituting  $\omega = 2\pi f$ .

Many of the applications of frequency combs rely on measuring and stabilizing the absolute frequencies of the comb lines[3], and in practice free-running mode-locked lasers do not produce optical frequency combs. Instead, both  $f_R$  and  $f_{\text{ceo}}$  exhibit a non-zero linewidth, and drift slowly in time. A simple heuristic for whether or not a laser can be considered a comb is whether or not the comb lines have been locked with a stability comparable to a CW single-frequency laser (1-10 KHz) across the bandwidth of the comb. Typical soliton-modelocked lasers have free-running linewidths of  $\sim 1$  MHz and  $\sim 10$  KHz for  $f_{\text{ceo}}$  and  $f_R$ , respectively, and therefore require active feedback.  $f_R$  can be stabilized by actuating the cavity to lock either the beatnote detected by a photodiode to an RF reference, or the beatnote between one of the comb lines and an optical reference.  $f_{\text{ceo}}$  is similarly stabilized to an RF reference by actuating the laser-diode current used to drive the laser. We will discuss the measurement of  $f_{\text{ceo}}$  in more detail after establishing a toolbox of common nonlinear devices. We close this section by noting that for some applications  $\phi_{\text{ceo}}$  must be locked to zero. Slow drifts of  $\phi_{\text{ceo}}$  on the scale of many round trips can be actively compensated using an adjustable wedge-pair. Translating two wedges in close contact effectively creates a dielectric with an adjustable thickness, which varies the relative delay between the carrier and envelope as  $\Delta\phi_{\text{ceo}} = 2\pi(n_g - n_p)L/\lambda$ , where  $n_g$  and  $n_p$  refer to the group index and the phase index respectively.

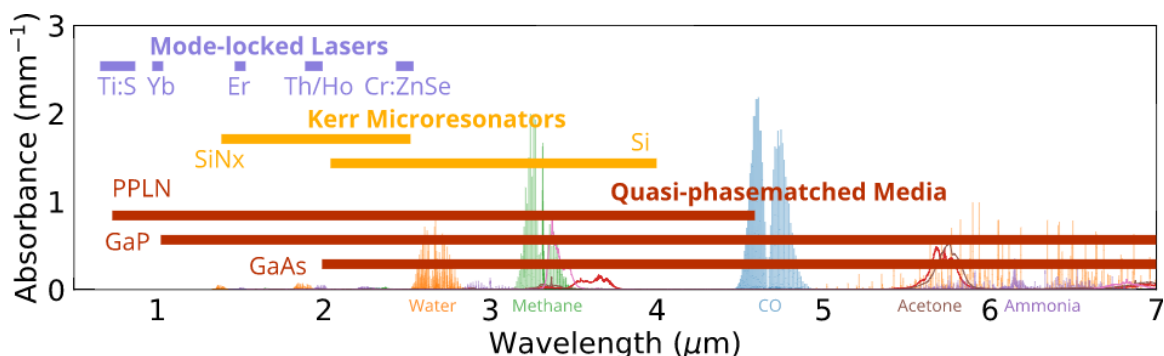


Figure 1.2: The absorption spectrum of some common molecules potentially used for medical diagnostics, and their overlap with the light sources considered here. GaP can produce wavelengths as long as 10- $\mu\text{m}$ , and GaAs can produce wavelengths as long as 20- $\mu\text{m}$ .

### 1.1.3 Sources and Applications of Optical Frequency Combs

The most common source of optical frequency combs is the stable train of pulses that form as a consequence of soliton modelocking in both lasers and microresonators. These techniques are well established at near- to mid-infrared frequencies spanning 800-nm - 3000-nm. An ongoing challenge in the field is the generation of optical frequency combs at long wavelengths (2-20  $\mu\text{m}$ )[13]. In this range frequency combs can be used as chemical diagnostics by measuring the optical transitions associated with molecular rotation and vibration. When compared to conventional spectroscopic techniques, frequency-comb-based molecular fingerprinting can achieve excellent resolution and sensitivity, and unprecedented speed[5]. Furthermore, these systems can potentially be scaled to small footprints with low power consumption, which would allow them to be used in tabletop and medical settings.

Fig. 1.2 illustrates the current status of several approaches for generating short optical pulses at various wavelengths of interest, overlaid with the absorption spectra of some common molecules of interest[14, 15]. Soliton mode-locking is well developed in materials such as Ti:Sapphire, Yb:fiber, Er:fiber, Th/Ho:fiber[16], and Cr:ZnSe[17] (Fig. 1.2, blue bars), with the typical range of wavelengths covered by these systems denoted by the width of the bar. The primary challenge of scaling these approaches to longer wavelengths is the availability of suitable host glasses and laser gain media. Undoubtedly, mode-locked lasers will eventually exist at any wavelength of interest, but each of these currently existing systems has taken on the order of a decade to develop. Kerr microresonators are a recent addition to the field, which are commonly developed using either SiNx[18, 19], or silicon nanoresonators[20] (Fig. 1.2, yellow bars). These nonlinear resonators can form mode-locked pulses at any wavelength where the resonator can be engineered to have small anomalous dispersion and low loss. The width of these bars denotes the range of wavelengths spanned by current demonstrations, with silicon successfully reaching as far as 3  $\mu\text{m}$ .

A compelling alternative to mid-infrared laser development is simply to shift well developed near-infrared frequency combs to long wavelengths using frequency conversion in materials with quadratic nonlinearities[21, 22, 23, 24, 25, 26, 27]. Many of these crystals are mature and commercially available, and only a handful of them are needed to convert near-infrared wavelengths to any wavelength in the mid-infrared. Periodically poled lithium niobate (PPLN), with orientation-patterned GaP and GaAs, (Fig. 1.2, red bars) together allow for the generation of any wavelength between 500-nm and 20- $\mu\text{m}$ [28, 29, 30]. Furthermore, many devices based on frequency conversion inherit the coherence properties of the pump laser[31], resulting in a mid-infrared frequency comb when the device is pumped with a near-infrared frequency comb. We consider such devices in Ch. 2.

### 1.1.4 Linear Propagation of Short Pulses

Before we consider nonlinear propagation of short pulses and optical frequency combs, we briefly treat the linear case. For a CW wave, the field evolution in a linear medium (dropping the complex conjugate) is given as

$$\mathcal{E}(z, t) = A_\omega \exp(i\omega_0 t - ik(\omega_0)z),$$

or in the frequency domain as

$$\hat{\mathcal{E}}(z, \omega) = \hat{A}_\omega \delta(\omega - \omega_0) \exp(-ik(\omega_0)z).$$

The propagation constant is given by  $k = n(\omega)\omega/c$ , where  $n(\omega)$  is the refractive index of the medium, and  $c$  is the speed of light in vacuum.

Propagation in the frequency domain naturally generalizes to a short pulse with each angular frequency  $\omega$  acquiring phase as  $-k(\omega)z$ . We begin with a short pulse at  $z = 0$ ,

$$\mathcal{E}(0, t) = A_\omega(0, t) \exp(i\omega_0 t),$$

and again Fourier transform to find

$$\hat{\mathcal{E}}(0, \omega) = \hat{A}_\omega(0, \omega - \omega_0).$$

Now, we propagate each frequency component with a propagation constant given by  $k(\omega)$ ,

$$\hat{\mathcal{E}}(z, \omega) = \hat{A}_\omega(0, \omega - \omega_0) \exp(-ik(\omega)z). \quad (1.3)$$

We may rewrite the left hand side of Eqn. 1.3 in terms of envelopes,  $\hat{\mathcal{E}}(z, \omega) = \hat{A}_\omega(z, \omega - \omega_0) \exp(-ik(\omega_0)z)$ , to convert this to a propagation equation for  $\hat{A}_\omega(\omega - \omega_0)$ ,

$$\hat{A}_\omega(z, \Omega) = \hat{A}_\omega(0, \Omega) \exp(-ik(\omega)z + ik(\omega_0)z), \quad (1.4)$$

where  $\Omega = \omega - \omega_0$  is the frequency detuning around  $\omega_0$ .

In many cases, including nonlinear propagation, the time evolution of  $A_\omega(z, t)$  is useful. We may find this first by differentiating both sides of Eqn. 1.4 with respect to  $z$ , and Taylor series expanding  $k(\omega)$  around  $\omega_0$  to find

$$\partial_z \hat{A}_\omega(z, \Omega) = \left( -ik'_\omega \Omega + \hat{D}_\omega(\Omega) \right) \hat{A}(z, \Omega), \quad (1.5)$$

where  $\hat{D}_\omega(\Omega) = -i \sum_{m=2}^{\infty} \left( k_\omega^{(m)} \Omega^m \right) / m!$  is the frequency-domain dispersion operator,  $k'_\omega = \partial_\omega k|_{\omega_0} = v_{g,\omega}^{-1}$  is the inverse group velocity at frequency  $\omega_0$ , and  $k_\omega^{(m)} = \partial_\omega^m k|_{\omega_0}$  is the  $m^{\text{th}}$  derivative of  $k$  with respect to angular frequency evaluated at  $\omega_0$ . We inverse Fourier transform Eqn. 1.5 using  $i\Omega \hat{A} \rightarrow \partial_t A$  to obtain the time-domain evolution of the envelope

$$\partial_z A(z, t) = -k'_\omega \partial_t A(z, t) + \hat{D}_\omega(t) A(z, t), \quad (1.6)$$

where  $\hat{D}_\omega(t) = \sum_{m=2}^{\infty} (-i)^{(m+1)} \left( k_\omega^{(m)} \partial_t^m \right) / m!$  is the time-domain dispersion operator. Hereafter, we will drop the argument of the dispersion operators  $\hat{D}_\omega$ , with the time-domain and frequency-domain implied by whether  $\hat{D}_\omega$  is acting on  $A(z, t)$  or  $\hat{A}(z, \Omega)$ . The first order term,  $k'_\omega$ , can be eliminated by moving into a reference frame co-moving with the pulse at its group velocity  $v_g = 1/k'_\omega$ . Therefore, the leading contribution of dispersion to the evolution of a pulse envelope is the second order term, which causes pulse spreading and chirp.

We close this section by noting that care must be taken when using terms beyond second order. In some cases, the series expansion of  $k(\omega)$  may have a small radius of convergence since the Sellmeier form used to express  $k(\omega)$  has poles for real frequencies. As a result, the number of terms needed to accurately model propagation can vary depending on the wavelength range under consideration. For example, when studying the formation of few-cycle pulses around 2- $\mu\text{m}$  in  $\text{LiNbO}_3$ , the Taylor series expansion of  $k(\omega)$  to third order is sufficient to describe all of the relevant pulse dynamics since the pulses achieve 3-dB bandwidths on the order of 10's of THz. However, when studying supercontinuum generation in the band between 1- $\mu\text{m}$  and 0.5- $\mu\text{m}$ , accurate simulations require the full dispersion relation  $k(\omega)$  across this 300-THz-wide band, since no Taylor series expansion can accurately capture  $k(\omega)$  over this range. In the following sections, we will discuss nonlinear pulse propagation and address how to model propagation with both nonlinearity and an arbitrary  $k(\omega)$ .

## 1.2 The Coupled Wave Equations

All of the nonlinear dynamics studied here arise due to the influence of the nonlinear polarization. We'll largely focus on two cases, i) the coupled wave equations for second harmonic generation, which describe both SHG and degenerate optical parametric amplification, and ii) the nonlinear Schrödinger equation (NLSE), which describes the formation of solitons and supercontinua. For the contexts studied here, the NLSE will arise as a special case of phase-mismatched SHG, but it

occurs in much broader contexts in nonlinear optics. Therefore, the resulting dynamics will inform both our discussions of conventional approaches used by the nonlinear optics community as well as some of the dynamical regimes studied here. Throughout this section we'll use a coupled-mode approach to nonlinear optics, which will always yield a system of equations with the same form as the plane-wave case. Accordingly, we will begin by deriving the coupled wave equations for second harmonic generation with plane-waves, and then address the case of Gaussian beams and nonlinear waveguides. These cases will represent the devices under study in Ch. 2 and Ch. 3, respectively.

### 1.2.1 Plane-wave Second Harmonic Generation

We begin by deriving the coupled wave equations for SHG, starting from Maxwell's equations,

$$\nabla \cdot \mathbf{D} = \rho \quad (1.7a)$$

$$\nabla \cdot \mathbf{B} = 0 \quad (1.7b)$$

$$\nabla \times \mathbf{E} = -\partial_t \mathbf{B} \quad (1.7c)$$

$$\nabla \times \mathbf{H} = \mathbf{J} + \partial_t \mathbf{D} \quad (1.7d)$$

For all of the contexts studied here, we will consider dielectric media ( $\rho = 0, \mathbf{J} = 0$ ) which are nonlinear, anisotropic, and non-magnetic ( $\mu_0 \mathbf{H} = \mathbf{B}$ ). In general, the constitutive relations for such a medium are given by

$$\mathbf{D} = \epsilon_0 \epsilon \cdot \mathbf{E} + \mathbf{P}_{\text{NL}} \quad (1.8a)$$

$$\mu_0 \mathbf{H} = \mathbf{B}. \quad (1.8b)$$

Furthermore, while all of the nonlinear media used in the following chapters are anisotropic, in many of these contexts the field will be polarized along a principle axis of the crystal. Therefore we may treat  $\epsilon = n^2$  as a scalar, and note here that the form of the resulting equations will not change when we consider the general case later. We treat the cases of Gaussian beams in cavities and guided modes in tightly-confining anisotropic waveguides in Appendix A.1 and A.2, respectively. For the case considered here, combining Maxwell's curl equations, we find the driven wave equation

$$\nabla^2 E - \frac{\epsilon}{c^2} E = \mu_0 \partial_t^2 P_{\text{NL}}. \quad (1.9)$$

Next, we assume the fields and the nonlinear polarization may all be described by plane-waves with slowly varying envelopes. In this case, the electric field is given by  $E = (A_\omega(z) \exp(i\omega t - ik_\omega z) + c.c.) / 2$ , and similarly  $P_{\text{NL},\omega} = (P_\omega(z) \exp(i\omega t - ik_\omega z) + c.c.) / 2$ , where  $k_\omega = n_\omega \omega / c$  is the propagation constant at frequency  $\omega$ . If the envelope varies slowly compared to the carrier,  $|\partial_z A_\omega| \ll |k_\omega A_\omega|$ , then

we may use the slowly varying envelope approximation,

$$\begin{aligned}\partial_z^2 E &= (\partial_z^2 A - 2ik\partial_z A_\omega - k_\omega^2 A_\omega) \exp(i\omega t - ik_\omega z)/2 + c.c. \\ &\approx (-2ik\partial_z A_\omega - k_\omega^2 A_\omega) \exp(i\omega t - ik_\omega z)/2 + c.c.\end{aligned}\quad (1.10)$$

Eqn. 1.10 is formally equivalent to neglecting the backwards propagating component of  $E$ , which is valid for almost every case of interest[32]. Eqns. 1.9-1.10 reduce to the slowly-varying envelope equation,

$$\partial_z A_\omega(z) = -i \frac{\omega \mu_0 c}{2n_\omega} P_\omega. \quad (1.11)$$

For second harmonic generation, the constitutive relations for the nonlinear polarization envelope are given by

$$P_{2\omega} = \frac{1}{2} \epsilon_0 \chi^{(2)} A_\omega^2 \exp(i(k_{2\omega} - 2k_\omega)z), \quad (1.12a)$$

$$P_\omega = \epsilon_0 \chi^{(2)} A_{2\omega} A_\omega \exp(-i(k_{2\omega} - 2k_\omega)z), \quad (1.12b)$$

where  $\chi^{(2)}$  is the nonlinear susceptibility of the medium,  $P_{\text{NL}}(\omega_m + \omega_n) = \epsilon_0 \sum_{m,n} \chi^{(2)} E(\omega_m) E(\omega_n)$ . Substituting Eqn. 1.12a-1.12b into Eqn. 1.11 yields the coupled wave equations for SHG

$$\partial_z A_\omega(z) = -i\kappa_\omega A_{2\omega}(z) A_\omega^*(z) \exp(-i\Delta k z) \quad (1.13a)$$

$$\partial_z A_{2\omega}(z) = -i\kappa_{2\omega} A_\omega^2(z) \exp(i\Delta k z), \quad (1.13b)$$

where  $\kappa_{j\omega} = \omega \chi^{(2)} / 2cn_{j\omega}$  is the nonlinear coupling between the fields, and  $\Delta k = k_{2\omega} - 2k_\omega$  is the phase-mismatch. Equations 1.13a-1.13b conserve the total intensity,  $I = I_\omega + I_{2\omega}$ , where  $I_\omega = n_\omega |A_\omega|^2 / 2Z_0$ . We may symmetrize these equations by renormalizing the fields by  $\sqrt{2Z_0/n_\omega}$ , to yield

$$\partial_z \bar{A}_\omega(z) = -i\kappa \bar{A}_{2\omega}(z) \bar{A}_\omega^*(z) \exp(-i\Delta k z) \quad (1.14a)$$

$$\partial_z \bar{A}_{2\omega}(z) = -i\kappa \bar{A}_\omega^2(z) \exp(i\Delta k z), \quad (1.14b)$$

where  $\kappa = \omega \chi^{(2)} \sqrt{Z_0} / (n_\omega c \sqrt{2n_{2\omega}})$ , and  $|\bar{A}_\omega|^2$  represents the intensity in units of W/m<sup>2</sup>.

Coupled wave equations with the form given by 1.14a-1.14b will be used to model  $\chi^{(2)}$  interactions throughout the following chapters. While this treatment assumed plane-waves as modes, which conserve intensity, these equations are unchanged when we consider either waveguide modes or Gaussian beams. In these cases, the field is distributed over a finite area, and  $A_\omega$  is normalized to represent the power in the mode, rather than the intensity. Similarly, the nonlinear coupling is now given by  $\kappa = \omega \chi^{(2)} \sqrt{Z_0} / (n_\omega c \sqrt{2n_{2\omega} A_{\text{eff}}})$ , where  $A_{\text{eff}}$  is the effective area for the nonlinear interaction. Small effective areas correspond to tightly confined modes with large field intensities and strong nonlinear interactions. For the remainder of this chapter we will drop the overbar on  $A$ , and

assume  $A$  has units of  $W^{-1/2}$  without concerning ourselves with what modes are being studied. In later chapters, where we study resonators and waveguides, we will derive the coupled wave equations and the effective area using the relevant spatial modes for each system.

### 1.2.2 Quasi-phasematching

As the fields associated with  $A_\omega$  and  $A_{2\omega}$  propagate in a nonlinear medium, they accumulate phase as  $\exp(-ik_\omega z)$  and  $\exp(-ik_{2\omega} z)$ , respectively. These phase velocities differ from that of the nonlinear polarization driving each field, giving rise to the phase mismatch  $\Delta k$ . Phase-mismatch limits the length over which energy may be transferred from one harmonic to the other, with energy converting back from the desired harmonic when it falls out of phase with the driving nonlinear polarization. As a result,  $\Delta k$  is one of the most crucial parameters in the coupled wave equations, and the vast majority of nonlinear optical devices achieve efficient operation by engineering  $\Delta k = 0$ .

As an example, we consider the buildup of the power contained by the second harmonic,  $P_{2\omega} = |A_{2\omega}|^2$ . The evolution of  $P_{2\omega}$  is given by

$$\partial_z P_{2\omega} = 2\text{Re}(A_{2\omega}^* \partial_z A_{2\omega}) = 2\kappa A_{2\omega} A_\omega^2 \sin(\Delta k z + \Delta\phi_0),$$

where  $\Delta\phi_0 = \phi_{2\omega} - 2\phi_\omega$  is the relative phase of the waves input to the crystal. One can readily show that  $\partial_z P_\omega = -\partial_z P_{2\omega}$ . As the fields propagate,  $P_{2\omega}$  initially builds up for  $z \in [0, \pi/\Delta k]$ . At a distance  $\Delta k z_{\text{coh}} = \pi$ , hereafter referred to as a coherence length, the sign of  $\partial_z P_{2\omega}$  becomes negative and power flows back into the fundamental harmonic. At  $z = 2z_{\text{coh}}$ , the second harmonic will be completely back-converted to fundamental and this process repeats.

One of the most common approaches for preventing back-conversion is to change the sign of  $\chi^{(2)}$  at every  $z = m\pi/\Delta k$ , such that  $\partial_z P_{2\omega} \geq 0$  for all  $z$ . This technique is referred to as quasi-phasematching[33], and the sign change of  $\chi^{(2)}$  may be achieved using crystallographic orientation inversions in semiconductors such as GaAs[34], or ferroelectric domain inversions in media such as LiNbO<sub>3</sub>[35]. For the periodic modulation of  $\chi^{(2)}(z)$  described above, we have

$$\chi^{(2)}(z) = \chi^{(2)} \text{sgn}(\cos(2\pi z/\Lambda_G) - \cos(\pi D)), \quad (1.15)$$

where  $\Lambda_G$  is the spatial period of the modulation, and  $D$  is the duty cycle. We may Fourier-series expand  $\chi^{(2)}(z)$  to find

$$\chi^{(2)}(z) = \chi^{(2)} \sum_m \frac{2}{m\pi} \exp\left(2\pi i m \frac{z}{\Lambda_G}\right) \sin(\pi m D), \quad (1.16)$$

and substitute Eqn. 1.16 into Eqns. 1.14a-1.14b to find

$$\partial_z A_\omega = -i\kappa A_{2\omega} A_\omega^* \sum_m \frac{2}{m\pi} \sin(\pi m D) \exp(-i\Delta k + 2\pi i m z / \Lambda_G), \quad (1.17a)$$

$$\partial_z A_{2\omega} = -i\kappa A_\omega^2 \sum_m \frac{2}{m\pi} \sin(\pi m D) \exp(i\Delta k + 2\pi i m z / \Lambda_G). \quad (1.17b)$$

When the period  $\Lambda_G$  is given by  $2\pi/(\Delta k)$ , the  $m = \pm 1$  orders in the Fourier series expansion will cancel the phase-mismatch, and the effective nonlinear coefficient is given by  $\chi_{\text{eff}}^{(2)} = 2\chi^{(2)} \sin(\pi D)/\pi$ . The higher order terms of the Fourier series contribute small, rapidly varying oscillations of  $P_{2\omega}$  and  $P_\omega$  and can often be neglected or approximated as an effective cubic nonlinearity. In general, the period may be patterned to vary as a function of space such that the local grating k-vector is given by  $k_G(z) = 2\pi/\Lambda(z)$ . In this case,  $\chi^{(2)}(z) = \chi^{(2)} \text{sgn}(\cos(\phi(z)) - \cos(\pi D))$ , where  $\phi_z = \int k_G(z) dz$ . The series expansion of the nonlinear coefficient is given by

$$\chi^{(2)}(z) = \sum_m \frac{2}{m\pi} \sin(\pi m D) \exp(im\phi(z)).$$

These aperiodic patterns are often used to apodize nonlinear interactions, as discussed in [36].

We close this section by noting that all of the devices studied here will rely on quasi-phasematching to engineer  $\Delta k$ . This restricts our choice of nonlinear materials to those that can achieve quasi-phasematching, namely, LiNbO<sub>3</sub>, LiTaO<sub>3</sub>, KTP, GaAs, GaP, and ZnSe. For ferroelectrics such as LiNbO<sub>3</sub>, LiTaO<sub>3</sub>, and KTP,  $\chi^{(2)}(z)$  is modulated using ferroelectric domain inversions, which occur when an electric field in excess of the coercive field is applied to lithographically patterned electrodes on the surface of the material[35]. For epitaxially grown crystals, such as GaAs, GaP, and ZnSe[37], domain inversions are achieved by growing layers of opposite orientation on patterned templates.

## 1.3 Canonical Solutions to the Coupled Wave Equations

In this section, we derive the key behaviors associated with SHG that will be recurring throughout this thesis. We will begin with continuous-wave second harmonic generation, and consider the undepleted, depleted, and phase-mismatched limits. In the undepleted limit we will arrive at the concept of the transfer function of a nonlinear interaction, which will quantify the limitations on the bandwidth attainable when converting frequency combs to long wavelengths. The behavior of the saturated limit will be important when we study pulse formation mechanisms in Ch. 2.

### 1.3.1 Phase-matched Second harmonic Generation

We begin with the simple case of phase-matched undepleted SHG, and drop the overbar such that  $|A_\omega|^2$  is now the power contained in a mode at  $\omega$ . In this case, both  $A_\omega(z) = A_\omega(0)$  and  $\Delta k = 0$ .

Therefore,  $A_{2\omega}$  evolves as

$$\partial_z A_{2\omega}(z) = -i\kappa A_\omega^2(0) \quad (1.18)$$

which is integrated to  $A_{2\omega} = -i\kappa A_\omega^2 z$ , or  $P_{2\omega} = \eta_0 P_\omega^2 z^2$  for the power contained in the second harmonic, where  $\eta_0 = \kappa^2$ . The key insight is that the efficiency of a nonlinear device grows linearly with the amount of power used to drive a process, and quadratically with propagation length.  $\eta_0$ , reported in units of  $\%/W\text{-cm}^2$ , is the typical figure of merit for a nonlinear device. Devices with large  $\eta_0$  may achieve efficient nonlinear interactions in a small footprint or with low power requirements.

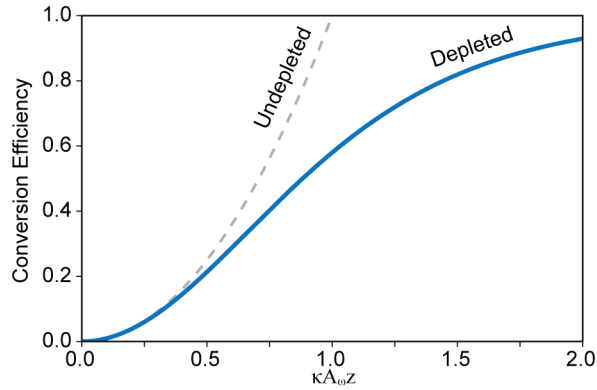


Figure 1.3: The conversion efficiency from fundamental to second harmonic as a function of  $z$  for saturated (solid blue) and unsaturated (dotted grey) SHG. 100% conversion in the unsaturated limit corresponds to 60% conversion when pump depletion is accounted for.

For saturated SHG, we shift the phase of the second harmonic envelope by  $-\pi/2$  to make the coupled wave equations and their solutions real, and use power conservation to reduce the coupled wave equations to a nonlinear ordinary differential equation

$$\partial_z A_{2\omega}(z) = \kappa(A_\omega^2(0) - A_{2\omega}^2(z)). \quad (1.19)$$

Eqn. 1.19 admits sech-tanh solutions for the fundamental and second harmonic, respectively,

$$A_\omega(z) = A_\omega(0)\text{sech}(\kappa A_\omega(0)z), \quad (1.20a)$$

$$A_{2\omega}(z) = A_\omega(0)\tanh(\kappa A_\omega(0)z). \quad (1.20b)$$

Eqns. 1.20a-1.20b exhibit a number of intuitive properties. In the limit of low depletion, they recover the undepleted result, and in the limit of high depletion they asymptote to 100% conversion efficiency. The sech-tanh behavior seen here will reappear in Ch. 2 when we study pulse formation mechanisms in optical parametric oscillators. We will find that under suitable conditions, such systems can reduce to the coupled wave equations with time replacing the position coordinate, resulting in the formation of a sech pulse at  $\omega$  and a tanh dark-pulse at  $2\omega$ . We close this section by noting that whether one

considers the depleted or the undepleted limit, the power requirements for efficient phase-matched SHG devices scales with  $\eta_0^{-1}$  and  $L^{-2}$ .

### 1.3.2 Phase-mismatched Second Harmonic Generation

We now consider the phase-mismatched case. There are largely two major insights from this treatment. First, we will see that the SHG conversion efficiency exhibits a  $\text{sinc}^2(\Delta kL/2)$  transfer function, which provides a useful tool for characterizing device performance. Second, we will see that in the limit of a large  $\Delta k$  the resulting dynamics will effectively contribute a nonlinear phase shift to the fundamental. This effect will be revisited when we study the nonlinear Schrödinger equation. In the limit of an undepleted fundamental, the second harmonic evolves as

$$\partial_z A_{2\omega}(z) = -i\kappa A_\omega^2(0) \exp(i\Delta kz). \quad (1.21)$$

Eqn. 1.21 can be integrated to find

$$A_{2\omega}(z) = -i\kappa A_\omega^2(0)z \exp(i\Delta kz/2) \text{sinc}(\Delta kz/2). \quad (1.22)$$

In the phase-matched limit, Eqn. 1.22 recovers the  $A_{2\omega} = -i\kappa A_\omega^2(0)z$  result from our previous analysis. However, for  $\Delta k \neq 0$  the second harmonic envelope oscillates sinusoidally in  $z$ , with an amplitude given by  $2\kappa A_\omega^2(0)/\Delta k$ . In terms of conversion efficiency,  $\eta = P_{2\omega}/P_\omega$ , Eqn. 1.22 takes the form

$$\eta(L) = \eta_0 P_\omega(0) L^2 \text{sinc}^2(\Delta kL/2). \quad (1.23)$$

The SHG transfer function given by Eqn. 1.23, along with  $\eta_0$ , characterizes the performance of a nonlinear device. Device inhomogeneities and loss mechanisms cause the transfer function to deviate from an ideal  $\text{sinc}^2$  shape[38]. Phase errors due to inhomogeneities generally broaden transfer function, with the total area of the transfer function conserved. Loss mechanisms give rise to a wide variety of behaviors; broadened transfer functions, either a suppression or an enhancement of the measured normalized efficiency when associating  $P_\omega$  and  $P_{2\omega}$  with the power output from the waveguide, and an overall reduction of total device efficiency. Furthermore, we will see in later sections that the width of the transfer function with respect to frequency determines the interaction length of short pulses input to the device. The SHG transfer function ultimately measures how short the pulses used to drive a device may be, and therefore how much the energy requirements of a device may be reduced.

We close this section by considering the evolution of the fundamental envelope during phase-mismatched SHG. The evolution of the fundamental can be found by reducing the coupled wave equations to a second-order ordinary differential equation in  $A_\omega$  [39], by using multiscale methods [40], or by substituting Eqn. 1.21 into  $\partial_z A_\omega = -i\kappa A_{2\omega} A_\omega^* \exp(-i\Delta kz)$  and assuming  $|A_\omega| \approx |A_\omega(0)|$

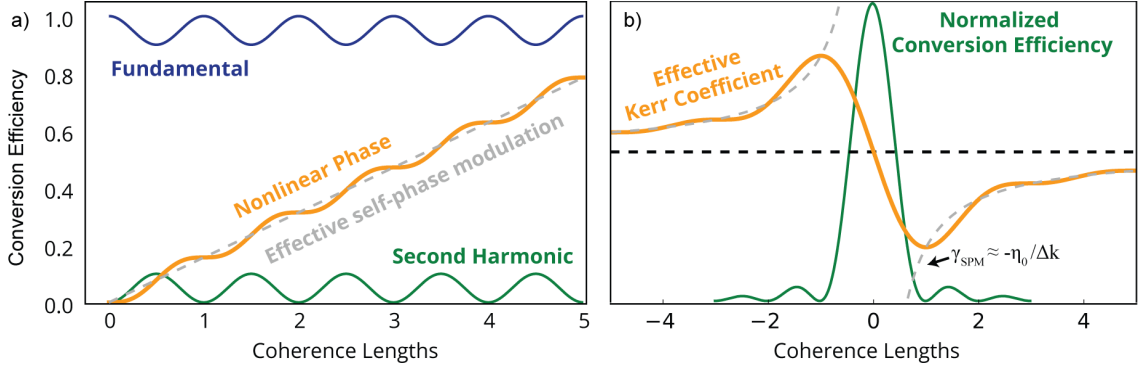


Figure 1.4: a) The power in the fundamental (green) and second harmonic (blue) as a function of  $z$  for fixed  $\Delta k$ . The nonlinear phase (orange) may be approximated by an average Kerr effect,  $\phi_{\text{NL}} = -\eta_0 z/\Delta k$  (grey line). b) The SHG conversion efficiency (solid blue) as a function of  $\Delta k$  for fixed device length  $L$ , showing a  $\text{sinc}^2(\Delta k L/2)$  transfer function. The effective Kerr nonlinearity (solid orange) is well approximated by  $\gamma_{\text{SPM}} = -\eta_0/\Delta k$  (dotted grey) for devices longer than two coherence lengths.

[41]. For illustrative purposes we adopt the latter approach, which yields

$$\partial_z A_\omega = i \frac{\eta_0}{\Delta k} |A_\omega|^2 A_\omega (1 - \exp(-i\Delta k z)). \quad (1.24)$$

While the amplitude of  $A_\omega$  is unchanged during propagation, Eqn. 1.24 can be integrated to show that the phase of the fundamental evolves as

$$\phi_\omega = \frac{\eta_0}{\Delta k} |A_\omega|^2 \left( z - \frac{\sin(\Delta k z)}{\Delta k} \right), \quad (1.25)$$

which is linear in both  $P_\omega$  and  $z$  for large  $\Delta k$ . Given the small contribution of  $\sin(\Delta k z)/\Delta k$  for large  $\Delta k$ , the  $\exp(-i\Delta k z)$  is typically neglected in Eqn. 1.24. We will see later that when considering the propagation of short pulses in the presence of large  $\Delta k$  Eqn. 1.24 reduces to the nonlinear Schrödinger equation, which allows  $\chi^{(2)}$  systems to access many of the dynamical processes normally associated with  $\chi^{(3)}$  systems.

Equations 1.23 and 1.25 comprise the main results of this section, and are summarized in Fig. 1.4. In short, we find that in the phase-mismatched limit the second harmonic oscillates sinusoidally with propagation length, and the resulting conversion efficiency decays rapidly with the phase-mismatch  $\Delta k$  as determined by the  $\text{sinc}^2(\Delta k L/2)$  transfer function for SHG. This illustrates that achieving phase-matching is crucial for efficient frequency conversion, and the existence of such a transfer function will lead us to the notion of the bandwidth of a nonlinear process. Finally, we find that back-action of the generated second harmonic on the fundamental results in phase modulation of the fundamental,  $\phi_{\text{NL}} \approx \eta_0 |A_\omega|^2 z/\Delta k$ .

### 1.3.3 The Bandwidth of Second Harmonic Generation

As discussed above, the existence of an SHG transfer function that filters the conversion efficiency,  $\eta(L)$ , naturally gives rise to the notion of a bandwidth associated with a nonlinear interaction. In the case of SHG we are interested two quantities, namely, the amount of second harmonic bandwidth that can be generated by a nonlinear device, and the amount of fundamental bandwidth that may contribute to SHG. First, we show that the generated second harmonic bandwidth is ultimately determined by the group velocity mismatch between the interacting waves. Then, we show that the amount of fundamental bandwidth that may contribute to SHG is limited by the group velocity dispersion of the fundamental.

We begin by considering the the amount of angular frequency detuning,  $\Omega$ , that we can impart on the fundamental wave before the generated second harmonic power at  $2\omega + 2\Omega$  drops to zero (Fig. 1.5(a)). The dispersion of the refractive index as  $\Omega$  is varied gives rise to a variation of the phase-mismatch,

$$\Delta k(\Omega) = k(2\omega + 2\Omega) - 2k(\omega + \Omega). \quad (1.26)$$

Given an arbitrary  $\Delta k(\Omega)$ , we define the bandwidth as the full width between the zeroes of the  $\text{sinc}^2(\Delta k(\Omega)L/2)$  transfer function, which occur at  $\Delta k(\Omega)L = \pm 2\pi$ . For many commonly encountered nonlinear media, the bandwidth of the SHG transfer function is determined, to first order, by the mismatch of the group velocities of the interacting waves. To see this, we Taylor series expand  $\Delta k$  with respect to  $\Omega$  to find

$$\Delta k(\Omega) = \Delta k_0 + 2\Delta k'\Omega, \quad (1.27)$$

where  $\Delta k_0 = \Delta k(0)$  is the phase-mismatch at  $\Omega = 0$  and  $\Delta k' = v_{g,2\omega}^{-1} - v_{g,\omega}^{-1}$  represents the group-velocity-mismatch between the interacting waves. For an interaction phase-matched at  $\Omega = 0$ , and neglecting terms of order  $\mathcal{O}(\Omega^2)$ , we find that  $\Delta kL = \pm 2\pi$  when  $2\Delta k'\Omega L = \pm 2\pi$ . If we define the accumulated delay between the fundamental and second harmonic as  $\tau_d = \Delta k'L$ , then the full width between the zeros of the SHG transfer function is given by

$$\Omega_{\text{FW}} = \frac{2\pi}{\tau_d}. \quad (1.28)$$

Equation 1.28 implies that the bandwidth of an SHG device is determined by the total amount of temporal walk-off that would be accumulated between an interacting fundamental and second harmonic. While we treat pulsed interactions later in this chapter, Eqn. 1.28 already allows us to develop some intuition about pulsed nonlinear processes. We see here that as long as the pulses used in a nonlinear interaction are long compared to the accumulated delay,  $\tau \gg \tau_d$ , or alternatively  $\Delta\Omega \ll \Omega_{\text{FW}}$ , the generated second harmonic pulse will not be filtered by the SHG transfer function.

We now consider how much fundamental bandwidth may be used to contribute to a generated

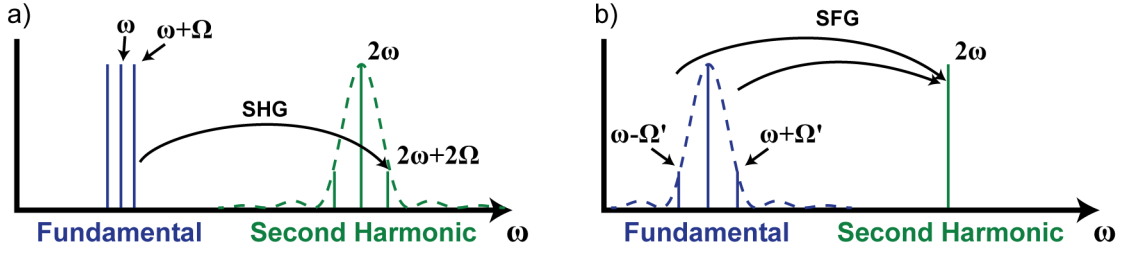


Figure 1.5: The two bandwidths associated with SHG. a) The total generated second harmonic bandwidth,  $\Omega_{\text{FW}}$ , is limited by  $\Delta k'$ . The height of the  $\text{sinc}^2$  function at  $2\omega + 2\Omega$  denotes the reduction in SHG due to filtering by the SHG transfer function. b) The amount of fundamental bandwidth that can contribute to SHG,  $\Omega'_{\text{FW}}$ , is limited by  $k''_{\omega}$ . Here, the height of the  $\text{sinc}^2$  transfer function denotes a reduced response at  $2\omega$  to SFG of the two frequencies at  $\omega \pm \Omega'$ .

second harmonic. In this case, we consider a three-wave interaction where  $2\omega = (\omega + \Omega') + (\omega - \Omega')$ , as shown in Fig. 1.5(b). In other words, we are considering sum-frequency generation (SFG) between two CW-lasers detuned from  $\omega$  by  $\pm\Omega'$ . While we haven't explicitly treated this case above, the functional form of Eqn. 1.23 is the same for sum frequency generation with minor modifications,

$$P_{2\omega}/P_{\omega+\Omega'} = 4\eta_0 P_{\omega-\Omega'} \text{sinc}^2(\Delta k L/2), \quad (1.29)$$

where  $\Delta k = k(2\omega) - k(\omega + \Omega') - k(\omega - \Omega')$ . We may again Taylor series expand with respect to the detuning  $\Omega'$  to find the frequency dependence of the phase-mismatch,

$$\Delta k(\Omega') = \Delta k_0 - k''_{\omega}(\Omega')^2. \quad (1.30)$$

For a phasematched interaction, the full-width of the fundamental bandwidth that can contribute to SHG is  $\Omega'_{\text{FW}} = 2\sqrt{(2\pi)/(k''_{\omega}L)}$ . This implies that all of the bandwidth associated with a fundamental pulse may contribute to SHG when the total chirp accumulated over the length of the device is small. We will see later that for pulsed SHG devices both  $\Delta k'$  and  $k''_{\omega}$  contribute to the dynamics. Remarkably, the phase-mismatch used to calculate the transfer function of a pulsed interaction will decompose into the two cases considered here.

## 1.4 Nonlinear Pulse Propagation

### 1.4.1 Second Harmonic Generation with Short Pulses

In previous sections, we saw that the efficiency of nonlinear interactions scales with the power they are driven with. For this reason nonlinear processes are often driven using short optical pulses,  $A(z, t)$ , so that the large field near the peak of the pulse can be used to achieve efficient interactions. In this

section we'll derive the coupled wave equations for SHG of a short pulse and treat the simplest case, which is undepleted SHG. Each of the following chapters will consider different operating regimes of the equations considered here, and we'll see that many different kinds of dynamics are possible. This section relies on a number of assumptions. First, we assume that both self-steepening and Raman effects are negligible. Second, we assume that the  $\chi^{(2)}$  nonlinearity is sufficiently dispersionless that the nonlinear polarization given by  $P_{\text{NL}}(2\omega) = \epsilon_0 \int \chi^{(2)}(2\omega; \omega', 2\omega - \omega') E(\omega') E(2\omega - \omega') d\omega'$  can be evaluated in the time domain  $P_{\text{NL},2\omega}(t) = 2\epsilon_0 d_{\text{eff}} E_\omega^2(t)$ . In this case, we may add the contributions to  $\partial_z A_\omega(z, t)$  from the dispersion operator in Eqn. 1.6 and the nonlinear coupling in Eqns. 1.14a-1.14b to find

$$\partial_z A_\omega(z, t) = -i\kappa A_{2\omega}(z, t) A_\omega^*(z, t) \exp(-i\Delta k z) + \hat{D}_\omega A_\omega(z, t), \quad (1.31a)$$

$$\partial_z A_{2\omega}(z, t) = -i\kappa A_\omega^2(z, t) \exp(i\Delta k z) - \Delta k' \partial_t A_{2\omega}(z, t) + \hat{D}_{2\omega} A_{2\omega}(z, t). \quad (1.31b)$$

One may still solve these equations for the case of unsaturated second harmonic generation using a transfer function approach [42, 43]. In this case, Eqn. 1.31a becomes

$$\partial_z A_\omega(z, t) = \hat{D}_\omega A_\omega(z, t), \quad (1.32)$$

which is readily solved in the frequency domain,  $\hat{A}(z, \Omega) = \hat{A}(0, \Omega) \exp(\hat{D}_\omega(\Omega)z)$ . Similarly, in the frequency domain Eqn. 1.31b becomes

$$\begin{aligned} \partial_z \hat{A}_{2\omega}(z, 2\Omega) &= -i\kappa \int \hat{A}_\omega(z, \Omega + \Omega') \hat{A}_\omega(z, \Omega - \Omega') \exp(i\Delta k z) d\Omega' \\ &\quad - i2\Omega \Delta k' \hat{A}_{2\omega}(z, 2\Omega) + \hat{D}_{2\omega}(2\Omega) \hat{A}_{2\omega}(z, 2\Omega). \end{aligned} \quad (1.33a)$$

Defining  $\tilde{A}_{2\omega}(z, 2\Omega) = \hat{A}_{2\omega}(z, 2\Omega) \exp(i\Delta k' 2\Omega z - \hat{D}_{2\omega}(2\Omega)z)$ , and multiplying both sides of Eqn. 1.35 by  $\exp(i\Delta k' 2\Omega z - \hat{D}_{2\omega}(2\Omega)z)$ , we have

$$\partial_z \tilde{A}_{2\omega}(z, 2\Omega) = -i\kappa \int \hat{A}_\omega(0, \Omega + \Omega') \hat{A}_\omega(0, \Omega - \Omega') \exp(i\Delta k(\Omega, \Omega')z) d\Omega' \quad (1.34)$$

where the phase mismatch is given by  $\Delta k(\Omega, \Omega') = k(2\omega + 2\Omega) - k(\omega + \Omega + \Omega') - k(\omega + \Omega - \Omega')$ . As with CW undepleted SHG, Eqn. 1.34 can be integrated to yield the resulting second harmonic,

$$\tilde{A}_{2\omega}(z, 2\Omega) = -i\kappa z \int \hat{A}_\omega(0, \Omega + \Omega') \hat{A}_\omega(0, \Omega - \Omega') \exp(i\Delta k(\Omega, \Omega')z/2) \text{sinc}(\Delta k(\Omega, \Omega')z/2) d\Omega'. \quad (1.35)$$

The response of the second harmonic to the input fundamental can still be understood in terms of a transfer function, but in this case we need to know  $\text{sinc}(\Delta k(\Omega, \Omega')z/2)$  for every pair of interacting frequencies. We again study the frequency dependence of the phase-mismatch by Taylor series

expanding  $\Delta k(\Omega, \Omega')$  to second order in  $\Omega$  and  $\Omega'$ , which yields

$$\Delta k(\Omega, \Omega') = \Delta k_0 + 2\Delta k'\Omega + (2k''_{2\omega} - k''_{\omega})\Omega^2 - k''_{\omega}(\Omega')^2. \quad (1.36)$$

The main feature of Eqn. 1.36 is that to second order  $\Omega$  and  $\Omega'$  enter independently, which allows us to interpret of the resulting dynamics using our insights from the CW case. We see that the amount of bandwidth of the fundamental that can contribute to SHG,  $\Omega'$ , is determined to leading order by  $k''_{\omega}$ . Similarly, we see that the amount of bandwidth generated at the second harmonic is limited to leading order by the temporal walk-off between the waves,  $\Delta k'$ . Finally we note that for narrowband pulses, or materials with small  $k''_{\omega}$ , we can neglect the  $\Omega'$  term. This renders  $\Delta k(\Omega, \Omega')$  a function only of  $\Omega$ , and Eqn. 1.35 reduces to

$$\tilde{A}_{2\omega}(z, 2\Omega) = -i\kappa z \exp(i\Delta k(\Omega)z/2) \text{sinc}(\Delta k(\Omega)z/2) \int \hat{A}_{\omega}(0, \Omega + \Omega') \hat{A}_{\omega}(0, \Omega - \Omega') d\Omega'. \quad (1.37)$$

Eqn. 1.37 yields an intuitive understanding of pulsed SHG for many case of interest. In essence, Eqn. 1.37 suggests that the nonlinear polarization generated by the fundamental is simply filtered by the CW SHG transfer function. Therefore, a semi-analytical calculation of the second harmonic may be achieved in two steps. First we calculate the second harmonic envelope that would be generated in the absence of dispersion,  $A_{2\omega}^{\text{ND}}(z, t) = -i\kappa A_{\omega}^2(0, t)z$ . Then, the power spectral density associated with this envelope is filtered in the frequency domain by the CW transfer function for SHG,

$$|\hat{A}_{2\omega}(z, 2\Omega)|^2 = \text{sinc}^2(\Delta k(\Omega)z/2) |\hat{A}_{2\omega}^{\text{ND}}(z, \Omega)|^2. \quad (1.38)$$

We will revisit this problem in Ch. 3, where we consider pulsed SHG in nanophotonic devices. Throughout the coming chapters, where we consider a variety of systems, simple analytic solutions will be few and far between. Instead, we will resort to finding approximate solutions to the coupled wave equations in various limits and attempt to stitch them together into simple heuristic pictures. In every case these heuristic models will be compared to full numerical simulations, which we discuss at the end of this chapter.

## 1.4.2 The Nonlinear Schrödinger Equation

In this section, we consider pulsed SHG in the presence of a large  $\Delta k$ . In this case, the coupled wave equations will reduce to an effective Nonlinear Schrödinger equation (NLSE) that describes the evolution of the fundamental envelope. The NLSE describes a wide variety of behaviors, and we will not attempt a comprehensive review of the dynamics of the NLSE here[44]. Instead, we will summarize a few technologically relevant regimes of interest, and give references for further reading where appropriate. For many of these regimes simple analytic models fail, and we often resort to heuristics and numerical modeling.

We begin by considering the coupled wave equations in the limit where the coherence length for SHG is much shorter than every other relevant scale in the problem. Typically, we consider this to be the case when two conditions are satisfied:  $|\Delta k| \gg \kappa A_0$ , where  $A_0 = \max(|A_\omega(0, t)|)$ , and  $|\Delta k| \gg 4\pi|\Delta k'/\tau|$ , where  $\tau$  is the transform-limited duration of the pulse input to the waveguide. Under these conditions, we may assume that  $|A_\omega(z, t)| = |A_\omega(0, t)|$  and the second harmonic is given by

$$A_{2\omega}(z, t) = -i\kappa A_\omega(0, t)^2 [\exp(i\Delta k z) - 1] / \Delta k. \quad (1.39)$$

As with the CW case (Eqn. 1.24), we substitute Eqn. 1.39 into the coupled wave equations for the fundamental and neglect dispersion beyond second order to find

$$i\partial_z A_\omega(z, t) + \frac{k''_\omega}{2} \partial_t^2 A_\omega + \gamma_{\text{SPM}}^{(2)} |A_\omega(z, t)|^2 A_\omega(z, t) = 0. \quad (1.40)$$

Equation 1.40 is known as the NLSE with a nonlinear coefficient for self-phase modulation given by  $\gamma_{\text{SPM}}^{(2)} = -\eta_0/\Delta k$  in rad/W-m. Typically, the NLSE occurs in the context of third order nonlinearities, with  $\gamma_{\text{SPM}}^{(3)} = 2\pi n_2/\lambda$  for plane-waves and  $\gamma_{\text{SPM}}^{(3)} = 2\pi n_2/(\lambda A_{\text{eff}}^{(3)})$  for guided modes, where  $n_2$  is the nonlinear refractive index of the medium in m<sup>2</sup>/W. We note here that since  $\chi^{(3)}$  nonlinearities are always present, the net self-phase modulation experienced by the fundamental is  $\gamma_{\text{SPM}} = \gamma_{\text{SPM}}^{(2)} + \gamma_{\text{SPM}}^{(3)}$ . The NLSE exhibits a broad array of behaviors spanning modulation instabilities, pulse formation and compression, breathers, solitons, and supercontinuum generation[44, 45]. Furthermore, generalizations of the NLSE that include any combination of gain, loss, driving terms, Raman scattering, and higher order dispersion have all been studied and found to exhibit useful dynamical regimes[46, 47]. Of all of these regimes, the two most relevant to the work presented here are soliton formation and supercontinuum generation. We begin with the former, which exhibits a simple closed form solution, and then give a heuristic description of the latter.

The fundamental soliton is a solution to the NLSE that propagates without distortion due to a balance between nonlinearity and dispersion,  $A_{\text{sol}}(z, t) = A_{\text{sol}}(0, t) \exp(i\phi(z))$ . The condition that  $\phi(z)$  is a function only of  $z$  guarantees the power spectral density of the pulse is conserved in addition to the instantaneous power,  $|A_\omega(z, t)|^2$ . Bright solitons can only occur when  $k''_\omega$  and  $\gamma_{\text{SPM}}$  have opposite signs. Given the assumptions made here, the NLSE can be integrated directly[44] to find

$$A_{\text{sol}}(z, t) = \sqrt{\frac{U_{\text{sol}}}{2\tau}} \text{sech}(t/\tau) \exp\left(\frac{ik''_\omega z}{2\tau^2}\right), \quad (1.41)$$

where  $U_{\text{sol}} = 2k''_\omega/(\gamma_{\text{SPM}}\tau)$ . Solitons exhibit a number of desirable properties, which make devices that produce optical solitons useful light sources. In addition to propagating without distortion, solitons are stable to perturbations and collisions, and in many cases the soliton state exists as a stable attractor with a large capture window. These features all contribute to the stability of

soliton-modelocked systems. The most common sources of solitons are modelocked lasers and Kerr microresonators, which regularly produce stable trains of soliton pulses with durations shorter than 100-fs. While a full understanding of these systems requires the addition of gain, loss, and a resonance condition to the NLSE, we simply remark here that these states occur as a double balance of two conditions: the gain cancels the loss, and the nonlinearity cancels the dispersion[2, 18].

Higher order solitons occur when  $A_\omega(0, t) = NA_{\text{sol}}(0, t)$ . For the case of  $N=2$ , the NLSE may be solved using an inverse scattering transform[44] to find

$$A_\omega(z, t) = 4\sqrt{\frac{U_s}{2\tau}} \left( \frac{\cosh(3t/\tau) + 3 \exp(4ik''_\omega z/\tau^2) \cosh(t/\tau)}{\cosh(4t/\tau) + 4\cosh(2t/\tau) + 3 \cos(4k''_\omega z/\tau^2)} \right) \exp\left(\frac{ik''_\omega z}{2\tau^2}\right). \quad (1.42)$$

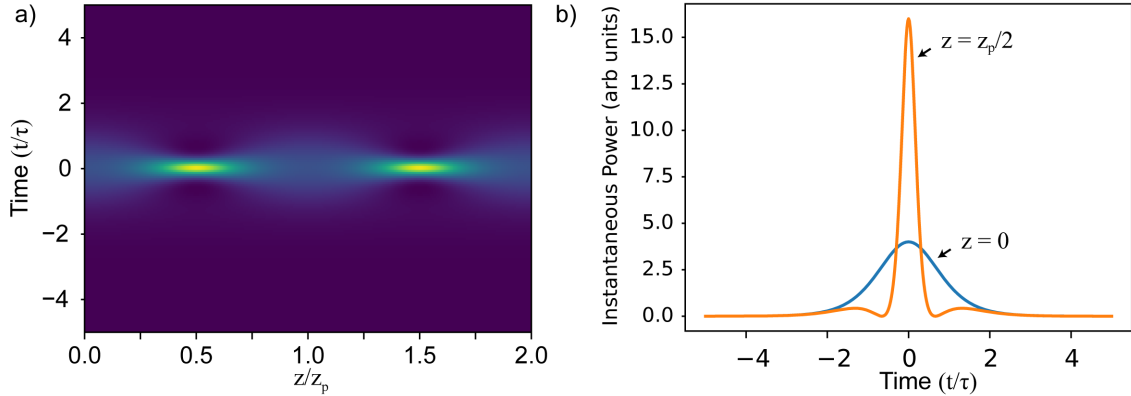


Figure 1.6: a) Evolution of the pulse shape,  $|A_\omega(z, t)|^2$ , for an  $N = 2$  soliton. The envelope evolves periodically, and compresses to a pulse with a four-fold increase in the peak power every half-period. b) The input soliton (blue) compared to the compressed pulse (orange).

$|A_\omega(z, t)|^2$  is shown in Fig. 1.6(a). There are two key features of the  $N=2$  soliton. First, this soliton exhibits periodic oscillations of the pulse envelope, with  $|A_\omega(z, t)|^2$  repeating with a period of  $z_p = \pi\tau^2/(2k''_\omega)$ . Second, the pulse envelope compresses to the smallest duration and the largest field intensity ( $4\sqrt{U_s/(2\tau)}$ ) at  $z_p/2$  (Fig. 1.6(b)). Pulse compression generally occurs for  $N > 1$ , and periodicity occurs for all  $N \geq 2$ . Furthermore, when periodic oscillation occurs, the shortest pulses form at  $z_p/N$ . Nonlinear fibers are often driven with  $1 < N < 3$  to compress pulsed lasers, and 5-fold enhancements of the input bandwidth are common in suitably designed fibers [48].

For solitons driven with  $N > 3$  the pulse formed at  $z_p/N$  tends to exhibit qcsufficiently large bandwidth that the NLSE breaks down. Instead, accurate models require the inclusion of higher order dispersion, Raman scattering, and self-steepening. Qualitatively, in the presence of these perturbations the pulse formed at  $z_p/N$  undergoes a process hereafter referred to as soliton fission. Following the treatment of [49], the pulse breaks up into  $N$  independent frequency-shifted solitons, each given by  $A_j = \sqrt{P_j} \text{sech}(t/\tau_j)$ , where  $P_j = \sqrt{U_s(2N - 2j + 1)^2/(2\tau N^2)}$  and  $\tau_j = \tau/(2N -$

$2j + 1$ ). When  $N > 6$ , the resulting spectrum may span more than an octave, and this process is referred to as supercontinuum generation. Remarkably, for  $N < 10$  and  $\tau < 200$ -fs, the coherence of the laser used to drive supercontinuum generation is preserved[45]. Under these conditions, the generated bandwidth can be used for spectroscopy and f-2f interferometry.

### 1.4.3 f-2f Interferometry

Having discussed frequency conversion and supercontinuum generation, we now give a brief overview of f-2f interferometry, which incorporates both of these effects. f-2f interferometers are the most commonly used method for detecting the  $f_{\text{ceo}}$  of a mode-locked laser, and the output of an f-2f interferometer can be used to provide a feedback signal to stabilize a frequency comb. The purpose of this section is two-fold. First, we explain how mode-locked lasers can be stabilized to form frequency combs. Second, when we consider that such a system is necessary to convert any mode-locked laser discussed in Sec. 1.1 into a frequency comb, this will motivate us to consider alternatives approaches both to comb generation and carrier envelope offset detection.

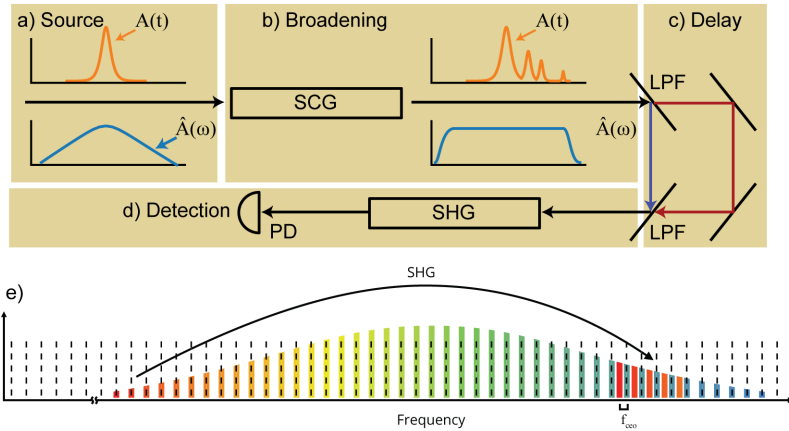


Figure 1.7: f-2f interferometry. a) A short pulse from a modelocked laser is broadened to an octave using supercontinuum generation in a tightly confining waveguide. Orange curve: pulse shape, blue curve: power spectral density. b) After soliton fission the pulse has broken up into several frequency shifted solitons, with a combined spectrum that spans a coherent octave. c) The long-wave portion of the spectrum passes through a long pass filter (LPF), and is delayed. d) The long wavelengths are recombined with the supercontinuum, passed through an SHG crystal, and absorbed by a photodetector (PD). e) Interference between the short wavelengths and the frequency-doubled long wavelengths produces a photocurrent that oscillates at  $f_{\text{ceo}}$ .

A schematic of a typical f-2f interferometer is shown in Fig. 1.7(a-d). A short pulse from a mode-locked laser is spectrally broadened to span a full octave, and then the low-frequency half is delayed, recombined with the comb, and is frequency doubled to overlap with the high-frequency half. The comb lines of the frequency doubled portion are given by  $f_n = 2f_{\text{ceo}} + nf_R$ , which interfere with

the lines associated with the original frequency comb (Fig. 1.7(e)). The resulting radio frequency beatnotes occur at  $\pm f_{\text{ceo}} + mf_R$ .

While the f-2f interferometer is the current gold-standard for  $f_{\text{ceo}}$  detection, it has several challenges. First, supercontinuum generation requires pulse energies comparable to 1-nJ in commercially available photonic crystal fibers, and  $\sim 10$ -pJ for state of the art SiNx nanowaveguides[50]. These pulse energies can consume a substantial amount of the power budget available for many modelocked lasers, especially ones with high repetition frequencies. Second, the delay arm used to correct the relative phase between the f and 2f can inject phase noise that is not shared between the comb lines. In many cases fluctuations in the length of this non-common-path section can ultimately limit the absolute frequency stability that may be achieved by the comb. Finally, stabilization requires a detector that is fast enough to see the f-2f beatnote and has sufficiently high gain to achieve a 25-dB signal to noise ratio. While these requirements are regularly achieved with silicon and InGaAs detectors, typical mid-infrared detectors tend to compromise between a low bandwidth and a weak responsivity. These limitations can make direct f-2f detection difficult at longer wavelengths. Many of the alternative approaches considered in later chapters will overcome these challenges. In Ch. 2, we will consider systems that generate mid-infrared frequency combs from near-infrared frequency combs, which will remove the need for a MIR f-2f interferometer entirely. In Ch. 3, we will demonstrate a nanophotonic device that achieves all of the functions of an f-2f interferometer using a single 6-mm-long waveguide.

## 1.5 Numerical Modeling of Nonlinear Interactions

There are many cases of interest where no closed form solution to the coupled wave equations exists. Examples explored in later chapters will include high-gain low-finesse synchronously pumped optical parametric oscillators (OPOs), saturated SHG with temporal walk-off, and supercontinuum generation with multiple interacting harmonics. In all of these cases we will rely on numerical simulations to model the underlying dynamics of the systems under study, and wherever possible we will use the insights gained from these simulations to build simple heuristic models that capture the behavior seen in both experiment and simulation. Remarkably, while analytic solutions to the coupled wave equations and the NLSE are often rather involved, the numerical methods used to solve these equations are relatively simple and work in an extremely broad range of contexts.

The key to our approach is that the nonlinear coupling is easily integrated in the time domain, while the dispersion operator is easily integrated in the frequency domain. The resulting algorithm is known as the split-step Fourier method, which alternates between solving the nonlinear coupling in the time domain and dispersive propagation in the frequency domain, taking small steps between each. The boundary values input to and output from the integrator are the frequency domain envelopes given by the fast Fourier transform (FFT) of the temporal envelope, e.g.  $\hat{A}_\omega(0, \Omega) =$

$\text{FFT}(A_\omega(0, t))$ . We describe the iterative steps of the split-step Fourier method used throughout this thesis below, following a treatment similar to [51]. The presentation here includes the  $\gamma_{\text{SPM}}$  due to the natural  $\chi^{(3)}$  of the medium. In many cases, we will compare the evolution of a pulse with and without  $\chi^{(3)}$  to determine how much the two nonlinearities contribute to the underlying dynamics. Each loop of the split-step Fourier method proceeds as follows:

1. Propagate to the current position in the nonlinear medium, accounting for temporal walk-off and dispersion beyond first order

$$\begin{aligned}\hat{A}_\omega(z_n, \Omega) &= \hat{A}_\omega(z_{n-1}, \Omega) \exp[-i(k(\omega + \Omega) - k(\omega) - k'(\omega)\Omega)z_n] \\ \hat{A}_{2\omega}(z_n, \Omega) &= \hat{A}_{2\omega}(z_{n-1}, \Omega) \exp[-i(k(2\omega + \Omega) - k(2\omega) - k'(\omega)\Omega)z_n]\end{aligned}$$

2. Evaluate the time-domain envelopes using the inverse fast Fourier transform (iFFT)

$$\begin{aligned}A_\omega(z_n, t) &= \text{iFFT}(\hat{A}_\omega(z_n, \Omega)) \\ A_{2\omega}(z_n, t) &= \text{iFFT}(\hat{A}_{2\omega}(z_n, \Omega))\end{aligned}$$

3. Evaluate the nonlinear coupling using the time-domain envelopes

$$\begin{aligned}\partial_z \hat{A}_\omega(z_n, \Omega) &= -i\kappa(\Omega) \text{FFT}[A_{2\omega}(z_n, t)A_\omega^*(z_n, t)] \exp(-i\Delta k z_n) \\ &\quad - i\gamma_{\text{SPM}}^{(3)}(\Omega) \text{FFT}[|A_\omega(z_n, t)|^2 A_\omega(z_n, t)], \\ \partial_z \hat{A}_{2\omega}(z_n, \Omega) &= -i\kappa(\Omega) \text{FFT}[A_\omega^2(z_n, t)] \exp(i\Delta k z_n) \\ &\quad - i\gamma_{\text{SPM}}^{(3)}(\Omega) \text{FFT}[|A_{2\omega}(z_n, t)|^2 A_{2\omega}(z_n, t)],\end{aligned}$$

where, for an Euler step, we would evaluate the change in the field envelope due to the nonlinear coupling using  $\Delta \hat{A}_\omega(z_n, \Omega) = \partial_z \hat{A}_\omega \Delta z$ .

4. Remove the linear phase associated with the current position, in preparation for the next loop

$$\begin{aligned}\hat{A}_\omega(z_n, \Omega) &= \left( \hat{A}_\omega(z_n, \Omega) + \Delta \hat{A}_\omega(z_n, \Omega) \right) \exp[i(k(\omega + \Omega) - k(\omega) - k'(\omega)\Omega)z_n] \\ \hat{A}_{2\omega}(z_n, \Omega) &= \left( \hat{A}_{2\omega}(z_n, \Omega) + \Delta \hat{A}_{2\omega}(z_n, \Omega) \right) \exp[i(k(2\omega + \Omega) - k(2\omega) - k'(\omega)\Omega)z_n]\end{aligned}$$

The net effect of steps 1 and 4 is to linearly propagate the generated fields a distance  $\Delta z_n = z_n - z_{n-1}$ ,

$$\hat{A}_\omega(z_n, \Omega) = \left( \hat{A}_\omega(z_{n-1}, \Omega) + \Delta \hat{A}_\omega(z_{n-1}, \Omega) \right) \exp[-i(k(\omega + \Omega) - k(\omega) - k'(\omega)\Omega)\Delta z_n].$$

When the split-step Fourier method is performed this way, each loop is agnostic to the size of the

step,  $\Delta z_n$ . This flexibility allows us to solve the coupled wave equations using standard adaptive ordinary differential equation solvers; we will use MATLAB's adaptive Runge-Kutta routine ODE45. We also note here that we have allowed  $\kappa$  and  $\gamma$  to be functions of the envelope frequency  $\Omega$ , which allows for corrections to the nonlinear coupling that occur for frequency detunings comparable to  $\omega$ . As an example, for a plane wave  $\kappa$  and  $\gamma_{\text{SPM}}$  both vary as  $(\omega + \Omega)$ , while for Gaussian beams  $\kappa$  and  $\gamma_{\text{SPM}}$  both vary as  $(\omega + \Omega)^{3/2}$ . This variation is usually negligible for narrowband pulses, but has been confirmed in pulsed SHG experiments where the input fundamental has a pulse duration comparable to two optical cycles[52]. To first order in  $\Omega$ , this effect contributes an effective self-steepening term in the time domain,  $\kappa \approx \kappa_0(1 - i\omega^{-1}\partial_t)$  for plane waves, and  $\kappa \approx \kappa_0(1 - i\frac{3}{2\omega}\partial_t)$  for Gaussian beams.

## 1.6 Overview of this Dissertation

This thesis broadly addresses the nonlinear dynamics of short optical pulses, and is focused on two topics: the formation of short optical pulses and frequency combs in synchronously pumped optical parametric oscillators, and frequency conversion with short pulses in nonlinear nanophotonic devices.

Ch. 2 addresses the pulse formation mechanisms of optical parametric oscillators in six sections. In Sec. 2.1 we review the theory of degenerate optical parametric oscillators, and provide an overview of how these tools may be used to generate optical frequency combs. In Sec. 2.2, we discuss the main pulse formation mechanisms that occur in synchronously pumped optical parametric oscillators, including the box-pulse model and the recently discovered simulton regime. In Sec. 2.3, we present an experimental characterization of the operating regimes of an OPO, which agrees well with the models proposed in Sec. 2.2. Sec. 2.4 ties together our heuristic models and the experimental results using numerical methods, and provides a detailed study of how optical parametric oscillators build up from noise to the steady-state behaviors observed in experiment. Sec. 2.5 discusses the limits of optical parametric oscillators in terms of the dispersion required to achieve stable operation and the resulting limitations of the generated optical bandwidth. Many of these questions are unresolved and we provide a summary of potential approaches that may yield further insights. Sec. 2.6 summarizes the results of Ch. 2 and discusses future work.

Ch. 3 discusses our work on ultrafast nonlinear optics in nanophotonic PPLN devices. Sec. 3.1 briefly summarizes the relevant aspects of nonlinear waveguides. Sec. 3.2 discusses our work developing the first nanophotonic PPLN devices, and presents an experimental characterization of such devices. In Sec. 3.3, we address the role of dispersion engineering in broadband nonlinear interactions, and includes an experimental characterization of ultrabroadband SHG in a phase-matched nanophotonic waveguide. We extend this work to phase-mismatched interactions in Sec. 3.4, and show that cascaded nonlinearities in these devices can realize an effective  $n_2$  orders of magnitude stronger than the natural  $n_2$  associated with  $\chi^{(3)}$  interactions in lithium niobate. Motivated by these

results, we study supercontinuum generation in nanophotonic PPLN devices in Sec. 3.5. These devices were able to generate coherent octaves of bandwidth spanning several harmonics with less pulse energy than previous demonstrations in state-of-the-art nonlinear waveguides. In Sec. 3.6 we provide a detailed heuristic model that describes the dynamics of the devices studied in Sec. 3.5 based on saturated SHG. This simple analytic model provides a great deal of insight about the observed behaviors of the generated supercontinuum, and is the first example of a novel dynamical regime that can only be accessed using nanophotonic devices. We summarize this work in Sec. 3.7.

The theoretical treatments in Ch. 2 - Ch. 3 all intentionally forgo the lengthy derivation of the nonlinear coupling for the systems under study and instead focus on the resulting nonlinear dynamics. These derivations are useful to readers who are interested in designing and building the systems studied throughout this thesis, but are not necessary to understand the dynamical processes presented throughout the thesis. For these reasons, we treat the nonlinear coupling for Gaussian beams and nonlinear waveguides in Appendix A and B, respectively.

In Ch. 4 we highlight ongoing research directions. An extremely promising direction for this work is chip-integrated optical parametric oscillators, which build on the results from both Ch. 2 and Ch. 3. In particular, we show that synchronously pumped optical parametric oscillators based on the platforms discussed in Ch. 3 can operate with thresholds approaching a single photon. These extremely nonlinear devices may open up entirely new directions for the field, and the application of such devices for both quantum and classical computation is a topic of ongoing research.

## Chapter 2

# Synchronously Pumped Optical Parametric Oscillators

### Introduction

As discussed in Ch. 1, conventional approaches to generating femtosecond pulses and phase-locked frequency combs are difficult to scale to long wavelengths due to the challenges associated with developing new broadband laser gain media and mid-infrared compatible host glasses. In contrast with  $\chi^{(3)}$  nonlinearities, the  $\chi^{(2)}$  associated with quadratic nonlinearities may be patterned to quasi-phasematch a rich variety of multi-wave interactions, and readily available  $\chi^{(2)}$  materials are frequently used to produce pulses at otherwise inaccessible wavelengths. Of particular interest are  $\chi^{(2)}$  resonators, such as OPOs, which allow for a resonant signal to efficiently extract power from the pump laser. The regimes of operation in OPOs are a subject of ongoing research, and there are likely untapped opportunities to develop new broadband light sources. Many pulse formation mechanisms have been proposed in continuous-wave-pumped degenerate OPOs[54, 53, 55, 56], however to date these systems have not yet achieved mode-locked femtosecond pulses by using such dynamics[57, 58]. Conversely, synchronously pumped degenerate OPOs have been used successfully to generate broadband frequency combs, but understanding the operating regimes of these systems requires one to untangle many competing pulse formation mechanisms[59]. Key results include the demonstration of octave-spanning-spectra[22], few-cycle pulses[26], intrinsic phase and frequency locking[31] (which translates the coherence properties of the pump source onto the half-harmonic signal), and conversion efficiencies as high as 64%[27]. In this chapter, we study pulse formation mechanisms in synchronously pumped degenerate OPOs, which comprise a  $\chi^{(2)}$  resonator pumped at  $2\omega$  that generates a resonant half-harmonic at  $\omega$  (Fig. 2.1). We will see that this route is a complementary approach to modelocked lasers that allows efficient conversion of near-infrared combs to

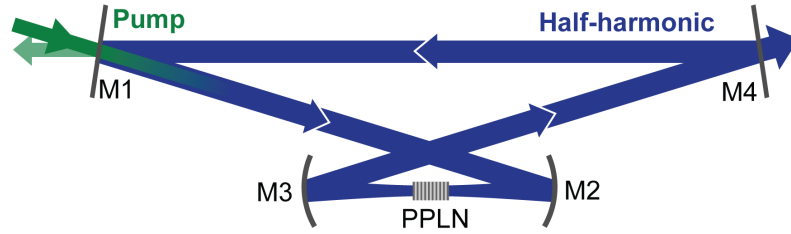


Figure 2.1: Schematic of a typical OPO. A bright pump at  $2\omega$  provides gain to a signal at  $\omega$  in a nonlinear crystal (PPLN). The signal is partially out-coupled through (M4), with the rest fed back to the nonlinear crystal. M1 has  $\sim 100\%$  transmission at the pump wavelength, which out-couples any leftover pump on each round trip.

long wavelengths. Furthermore, we will see that OPOs support unique pulse formation mechanisms that can be used to generate frequency combs with substantially more bandwidth than the pump comb input to the OPO.

This chapter proceeds in six parts. In Sec. 2.1 we review the theory of degenerate OPOs and show that degenerate operation enables both large conversion efficiencies and intrinsic phase-locking to the pump laser. We also discuss the role of cavity length detuning, dispersion, and synchronization between the pump laser and the cold-cavity round trip time. In Sec. 2.2, we review several of the pulse formation mechanisms that have been found to exist in OPOs. The treatment presented here largely follows that reported in [59]. Particular focus will be given to the soliton regime[60], in which the formation of bright-dark solitons in the cavity results in the efficient generation of phase-locked few-cycle pulses. Sec. 2.3 discusses the practical aspects of OPO design, and presents an experimental characterization of an OPO. These results are interpreted in terms of the steady-state operating regimes presented in Sec. 2.2. We consider full numerical simulations of the operating regimes of an OPO in Sec. 2.4. These numerical models enable us to study the dynamical behavior of each regime as the resonant fundamental builds up from semi-classical vacuum noise to steady-state, and further validate the reduced models discussed in Sec. 2.2-2.3. In Sec. 2.5, we discuss potential limits to the maximum bandwidth achievable in the soliton regime. Sec. 2.6 summarizes these results and discusses avenues of further research.

## 2.1 The Theory of Degenerate OPOs

This section covers the theory of pulse formation in degenerate OPOs. Since we will occasionally contrast this case with non-degenerate operation, where pump photons at  $\omega_p$  split into signal and idler photons at  $\omega_s$  and  $\omega_i$ , we will use  $s$  and  $p$  as our nomenclature instead of the  $\omega$  and  $2\omega$  used in Ch. 1. First, we treat the continuous-wave (CW) theory of OPO operation, which will yield a number of crucial insights about the properties of degenerate OPOs. These insights will extend

naturally to a frequency-domain picture of comb formation in OPOs. The latter portion of this section will treat the roles of synchronous pumping and intracavity dispersion.

### 2.1.1 Degenerate Operation

All of the interactions considered in this chapter occur between Gaussian beams in a free-space cavity. We review the coupled wave equations for Gaussian beams in Appendix A.1, and simply remark that for the cases considered here the coupled wave equations for degenerate OPA are the same as those for SHG, but driven with a bright pump at the second harmonic instead of the fundamental. For simplicity, we consider the case where the fundamental and second harmonic are given by TE<sub>00</sub> Gaussian beams with confocal parameters much larger than the nonlinear medium. Minor corrections due to the variation of the nonlinear coupling and phase mismatch along the crystal are included in Sec. 2.4, and do not substantially modify the behavior discussed here. In this case, for a phase-matched interaction with  $\Delta k = 0$ , the coupled wave equations are given by

$$\partial_z A_s = -i\kappa A_p A_s^*, \quad (2.1a)$$

$$\partial_z A_p = -i\kappa A_s^2, \quad (2.1b)$$

where  $\kappa = \sqrt{2Z_0\omega d_{\text{eff}}}/(w_0 n_\omega \sqrt{\pi n_{2\omega} c})$ , and  $w_0$  is the waist of the focused Gaussian beam at  $\omega$ . We note that the evolution of  $A_s$  and  $A_p$  depends only on the relative phase between the pump and signal,  $\phi_p - 2\phi_s$ , rather than the absolute phase of each envelope. Therefore, we may assume  $\phi_p = \pi/2$  without loss of generality. Assuming an undepleted pump,  $A_p(z) = A_p(0)$ , these equations reduce to

$$\partial_z A_s = \gamma_0 A_s^* \quad (2.2)$$

where  $\gamma_0 = \kappa |A_p(0)|$ . This phase convention for the pump wave is chosen such that a signal with 0 phase grows exponentially,  $A_s(z) = A_s(0) \exp(\gamma_0 z)$ . In a crystal of length  $L$ , this corresponds to a power gain of  $G = P_s(L)/P_s(0) = \exp(2\gamma_0 L)$ . In the general case, where the signal may have an arbitrary phase, we decompose the signal into a real and imaginary part  $A_s = x_s + ip_s$ . In this case the real part grows exponentially, as described above, while the imaginary part is de-amplified  $p_s(z) = p_s(0) \exp(-\gamma_0 z)$ . Since only the in-phase component is amplified, we expect that any signal generated by a degenerate OPO above threshold will be phase-locked to the pump laser, with offset  $\phi_p - 2\phi_s = \pi/2 + 2n\pi$ . We will see later that this behavior guarantees that the signal formed by a degenerate OPO synchronously pumped by an optical frequency comb is itself an optical frequency comb that is phase- and frequency-locked to the pump.

We now consider the role of the cavity in a degenerate OPO, and derive the conditions for resonance and threshold. After one round trip, the signal input to the crystal is given by

$$A_{s,n+1}(0) = r \exp(i\phi_c) A_{s,n}(L) \quad (2.3)$$

where  $r = \sqrt{R}$  is the feedback coefficient of the cavity.  $R$  may contain loss due to mirror reflectivities, absorption, and an effective nonlinear loss due to gain induced diffraction[61, 62]. This latter effect will become important when we consider high gain OPOs; for a detailed discussion we refer the reader to Appendix A.1.  $\phi_c$  is the accumulated phase per round trip,  $\phi_c = \sum_j k_j(\omega_s)L_j + \phi_G$ , where,  $k_j(\omega_s)$  is the propagation constant of the  $j$ th component in the cavity at frequency  $\omega_s$  and  $\phi_G$  is the Guoy phase accumulated by the cavity mode. Since equation 2.2 is symmetric under the transformation  $\phi_s \rightarrow \phi_s + \pi$  the signal is amplified on successive round trips,

$$A_{s,n+1}(0) = r \exp(i\phi_c) \exp(\gamma_0 L) A_{s,n}(0), \quad (2.4)$$

provided that  $\phi_c = -\ell\pi$ , where  $\ell \in Z$ . The sign convention of  $\ell$  is chosen such that increasing  $\ell$  corresponds to a longer cavity. For the CW case, resonance occurs when  $\ell$  is a multiple of 2, such that successive round trips constructively interfere. We note here that in general the OPOs under study in this chapter will be pumped by pulsed lasers, and we will see in later sections that this will relax the resonance condition such that typically only  $\ell \in Z$  is necessary for resonance to occur.

When the resonance condition is satisfied, threshold is then set by the condition that the power gain exceeds the cavity loss

$$R \exp(2\gamma_0 L) > 1 \quad (2.5)$$

or equivalently,  $P_{\text{th}} = \ln(R)^2 / (4\kappa^2 L^2)$ , where  $P_{\text{th}} = |A_p|^2$  at threshold. For a high finesse cavity  $\ln(R)^2 \approx T^2$ . This gives an intuitive definition of threshold in an OPO; the amount of pump power at the second harmonic needed to achieve oscillation,  $P_{\text{th}}$ , is the same as the amount pump power at the fundamental,  $P_s$ , needed to achieve an SHG conversion efficiency of  $(T/2)^2$  in a single pass through the nonlinear crystal. As an example, for 10% outcoupling, the amount of pump power needed to achieve oscillation is the same as that needed to achieve an SHG conversion efficiency of 0.25%. In contrast, for singly resonant OPOs (SROs) where a distinct signal and idler are formed and only one is fed back, threshold is given by  $P_{\text{th}} = T/\kappa^2 L^2$ , which exceeds the threshold of a degenerate ORO by  $4/T$ .

We close this section by discussing the conversion efficiency of a degenerate OPO and comparing this against other approaches. In steady state, for a high finesse cavity, it can be shown that the conversion efficiency is

$$\eta = \frac{4}{M} \left( \sqrt{M} - 1 \right) \quad (2.6)$$

where  $M = |A_p|^2 / P_{\text{th}}$  is the times above threshold. Perfect conversion occurs when  $M = 4$ . In contrast, the conversion efficiency for an SRO is ultimately limited by the Manley-Rowe relations,  $|A_p|^2 / \omega_p = |A_s|^2 / \omega_s = |A_i|^2 / \omega_i$ . In other words, the condition that each pump photon splits into a signal photon and an idler photon ultimately limits the conversion efficiency,  $|A_s|^2 / |A_p|^2$ , to  $\omega_s / \omega_p$ . In the degenerate case, where  $\omega_s = \omega_p / 2$ , this constraint is lifted and one may achieve perfect conversion from the pump to the signal.

### 2.1.2 Frequency Combs in Degenerate OPOs

The three features shown in the previous section, namely, low threshold, high conversion efficiency, and intrinsic phase-locking suggest that degenerate OPOs are a promising approach for producing optical frequency combs in the mid-infrared. Instead of developing femtosecond mode-locked lasers, supercontinuum generators, and f-2f interferometers at mid-infrared frequencies, one need only to synchronously pump a degenerate OPO with a near-infrared frequency comb. In this section, we will discuss the formation of frequency combs in degenerate OPOs in more detail using a frequency domain approach. This approach will make explicit many of the notions suggested throughout the previous section. In particular, we will derive the resonance condition for an optical frequency comb in a degenerate OPO, and show that when an OPO achieves degenerate operation the resulting comb is intrinsically phase- and frequency-locked to the pump comb.

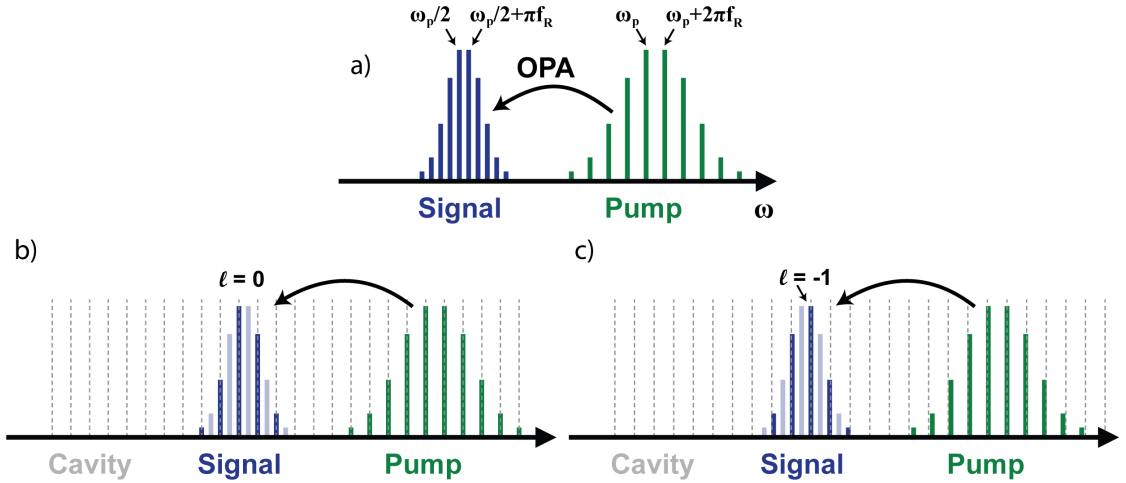


Figure 2.2: a) Schematic of fundamental comb formed by degenerate OPA. In principle, this process allows for the formation of comb lines with frequencies spaced by  $f_R/2$ . b) In the presence of a synchronously pumped cavity, the signal comb is filtered to have the same repetition frequency as the pump. c) Detuning the cavity by half of a free spectral range brings the second frequency comb into resonance. As a result, synchronously pumped OPOs exhibit resonances when the cavity length is detuned by a pump wavelength, not a signal wavelength.

We begin by considering a heuristic picture of degenerate OPA pumped by a frequency comb. In this case, the pump contains frequencies given by  $f_{m,p} = f_{\text{ceo},p} + 2\pi m f_R$ . Assuming that the degenerate OPA divides each pump frequency in half, this results in a comb with frequencies given by  $f_{m,s} = f_{\text{ceo},p}/2 + 2\pi m f_R/2$ , as shown schematically in Fig. 2.2(a). There are two main implications of this approach. First, we expect the signal comb to have a carrier envelope offset frequency of half the pump comb,  $f_{\text{ceo},s} = f_{\text{ceo},p}/2$ , since every frequency in the comb has been divided by two. Second, the OPA can apparently generate a comb with a frequency spacing given by  $f_R/2$ . In

practice, we expect the signal pulses to share the same spacing in time as the input pump pulses, and therefore expect that the comb formed by degenerate OPA will still have a frequency spacing of  $f_R$ . This apparent contradiction is resolved by considering a synchronously pumped OPO, where the cavity is chosen to have the same round-trip time as the repetition period of the pump laser.

Fig. 2.2(b) illustrates the formation of an optical frequency comb in a synchronously pumped OPO. The dotted grey lines denote the cavity resonances, where we have assumed a dispersionless cavity with a frequency spacing of  $f_R$ . For convenience, we now redefine our phase convention such that  $\ell = 0$  corresponds to the case where the cavity is both on resonance with the signal and perfectly synchronous with the pump comb. This corresponds to choosing a coordinate system that is co-propagating with the pump pulses incoupled to the resonator on every round trip. In this case, the cavity resonances align with frequencies given by  $\Omega_{m,s} = \omega_p/2 + 2\pi m f_R$ . Every other comb line is filtered off, resulting in a signal comb with the same repetition frequency as the pump comb. The signal comb has a carrier-envelope-offset frequency given by  $f_{ceo,s} = f_{ceo,p}/2$ , as above. In contrast with CW OPOs, oscillation also occurs when  $\ell = -1$ , as shown in Fig. 2.2(c). In this case, the cavity resonances align with frequencies given by  $\Omega_{m,s} = \omega_p/2 + 2\pi(m + 1/2)f_R$ , and the signal comb is now formed with a carrier envelope offset given by  $f_{ceo,s} = f_{ceo,p}/2 + f_R/2$ . While both cases are resonant, with the cavity modes aligning with the comb lines of the signal, resonances with  $\ell \in \text{odd}$  will form with the carrier envelope offset frequency shifted by  $f_R/2$ . For a pump comb with  $f_{ceo,p} = 0$ , and  $\phi_p = \pi/2$ , this means that the signal pulses formed by the OPO will have a phase of 0 or  $\pi$  when  $\ell \in \text{even}$ . In contrast, for  $\ell \in \text{odd}$ , the pulses will successively alternate between phases of 0 and  $\pi$ . In either case, the comb formed by the OPO is frequency-locked to the pump comb used to drive it, and phase-locked with an offset of either 0 or  $\pi$ . In the general case, the signal satisfies  $\phi_p - 2\phi_s = \pi/2 + m\pi$ , and the carrier envelope offset frequency of the two possible signal combs is shifted by  $f_{ceo,p}/2$ . Therefore, the coherence properties of the resulting pulse train are entirely determined by the pump comb; if the pump comb has a stabilized repetition frequency, carrier envelope offset frequency, and carrier envelope offset phase, then the signal comb generated by the OPO also has a stabilized repetition frequency, carrier envelope offset frequency, and carrier envelope offset phase.

### 2.1.3 Asynchronous Pumping

While the treatment throughout the previous section has assumed the cavity and pump to be synchronous, in practice OPOs oscillate for many of the resonances near perfect synchronization. We consider the role of asynchronous pumping here. If we again consider a cavity length detuning such that  $\ell = -1$ , the cavity length is now reduced by one pump wavelength and therefore has a slightly larger mode-spacing than the pump comb,  $f_R - \Delta f_{cav} = -c\lambda_p/L^2$ , where  $\Delta f_{cav}$  is the frequency spacing of the cold cavity resonances, and  $L$  is the optical path length of the cavity for  $\ell = 0$ . In general, the mismatch between the mode spacing for the cavity and the pump comb is

given by

$$f_R - \Delta f_{\text{cav}} = c\lambda_p \ell / L^2.$$

The role of this mismatch between the cavity resonances and the pump repetition frequency is best understood in the time domain. In this case, the offset between the pump repetition period and the round-trip time of the cold cavity can be understood as a small group delay or advance accumulated by the intracavity signal pulse on every round trip (Fig. 2.3). On every round trip, as a new pump pulse enters the cavity through the input coupler, we shift the coordinate system to co-propagate with the in-coupled pump pulse and the signal effectively accumulates a small timing shift  $\Delta T_{\text{RT}} = 2\pi\ell/\omega_p$ , such that  $\ell = 1$  corresponds to a group delay of an optical cycle of the pump carrier frequency.  $\Delta T_{\text{RT}}$ , hereafter referred to as the timing mismatch, corresponds to a group delay when  $\ell > 0$  and a group advance when  $\ell < 0$ .

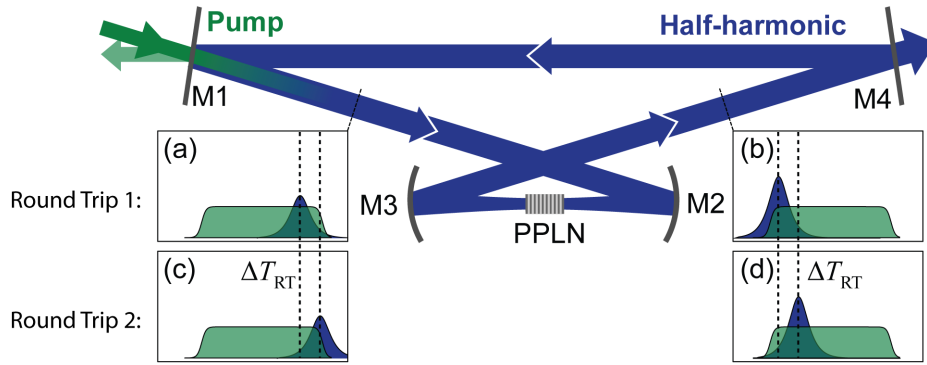


Figure 2.3: The role of asynchronization in a degenerate OPO. On the first round trip, a signal pulse initially forms such that it experiences symmetric temporal walk-off from the pump. a) Before the nonlinear crystal, the signal is delayed from the pump by  $\Delta k' L/2$ . We note here that a signal on the left corresponds to earlier time, and therefore pulses with higher group velocities move left relative to the others. b) After the nonlinear crystal, the signal is amplified and has a group advance relative to the pump due to temporal walk-off with  $\Delta k' > 0$ , which corresponds to  $v_{g,s} > v_{g,p}$ . c,d) On the next round trip, the signal acquires a relative delay of  $\Delta T_{\text{RT}}$  everywhere in the cavity, and now experiences less gain.

This effect is negligible unless the accumulated delay is sufficiently large to reduce the gain experienced by the signal due to a poor temporal overlap with the pump. We can treat this effect quantitatively by considering the solution to the coupled wave equations in the time domain by neglecting dispersion beyond first order, and assuming a coordinate system moving with the group

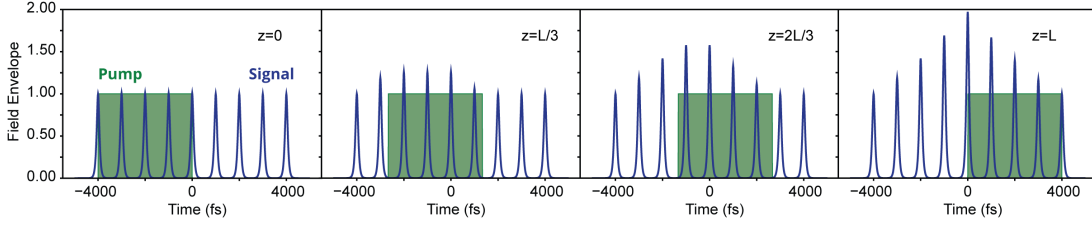


Figure 2.4: Illustration of the gain clipping function associated with a flat-top pump pulse. In this example, we consider a train of finely spaced signal pulses to better visualize the gain as a function of relative time delay. As the pump walks through the train of signal pulses they are amplified according to Eqn. 2.9. The pulse peaked at  $t = 0$  corresponds to the case of symmetric temporal walk-off and experiences the largest field gain.

velocity of the signal,

$$\partial_z A_s(z, t) = \kappa A_p(z, t) A_s^*(z, t) \quad (2.7a)$$

$$\partial_z A_p(z, t) = -\Delta k' \partial_t A_p(z, t) - \kappa A_s^2(z, t). \quad (2.7b)$$

The temporal walkoff is given by  $\Delta k' = k'_p - k'_s$ . For an undepleted pump, the pump is simply given by  $A_p(z, t) = A_p(0, t - \Delta k' z)$ , and the amplification of the fundamental is given by

$$A_s(z, t) = \exp\left(\int_0^z \kappa A_p(0, t - \Delta k' z') dz'\right) A(0, t). \quad (2.8)$$

Following the treatment of [59], we define the gain clipping function as  $\Gamma(z, t) = \int_0^z \kappa A_p(0, t - \Delta k' z') dz'$  such that the field gain is given by  $g(z, t) = \exp(\Gamma(z, t))$ , with corresponding power gain  $G(z, t) = g^2(z, t)$ . The gain clipping function gives rise to a field gain that depends on the relative timing between the pump and the signal input to the crystal. A fictitious example of this process is shown in Fig. 2.4, where the spacing of the signal pulses is chosen to be sufficiently small that many of them are amplified by the same pump pulse. The field gain is maximized for the signal pulse peaked at  $t = 0$  when the input pump pulse is peaked at  $t = -\Delta k' L/2$ .

The gain clipping function  $\Gamma(L, t)$  ultimately determines both the threshold of a synchronously pumped OPO, as well as how critical synchronization is. When the OPO is perfectly synchronized, threshold is given by the condition that the peak of the power gain balances the cavity loss,  $\max(G(L, t)) = 1/R$ . For asynchronous pumping, the field gain decays on successive round trips. As an example, for a flat-top pump pulse with a full-width of  $T_p$ , a relative delay of  $-T_p/2$ , and a total temporal walk-off given by  $\Delta k' L = T_p$ , the gain clipping function is  $\Gamma(L, t) = \kappa L(1 - |t|/T_p) A_{2\omega, 0}$ , where  $|A_{2\omega, 0}|^2$  is the peak power of the flat-top pump pulse of duration  $T_p$ . The resulting field gain experienced by a signal pulse decays exponentially with the relative timing,  $\Delta T$ , between the pump

and the signal

$$g(L, t) = \exp(\kappa L) \exp(-\kappa L |t - \Delta T| / T_p). \quad (2.9)$$

For an asynchronous cavity the relative delay between the signal pulse circulating in the cavity and the pump pulse injected into the cavity grows with every round trip,  $\Delta T(m) = m\Delta T_{\text{RT}}$ , where  $m$  is the round trip number. The resulting field gain decays on successive round trips. Therefore, when  $\Delta T_{\text{RT}}$  is comparable to  $T_p$  no signal pulse can form in the cavity. When  $\Delta T_{\text{RT}} \ll T_p$ , effects such as gain saturation or higher order dispersion can reshape the signal pulse and compensate for these delays, leading to steady-state oscillation. We discuss these cases in later sections.

While all of the OPOs considered in [59] used flat-top pulses as the pump, many of the experimental conditions considered later use the  $\text{sech}((t)/\tau)$  pulses produced by modelocked lasers. In this case, the gain clipping function of Eqn. 2.8 is given by

$$\Gamma(L, t) = \kappa A_{2\omega, 0} L \frac{2\tau}{\Delta k L} \left[ \tan^{-1}(\exp((t - \Delta T)/\tau)) - \tan^{-1}(\exp((t - \Delta T - \Delta k' L)/\tau)) \right], \quad (2.10)$$

where  $\Delta T$  is the relative delay between the pump and signal pulses input to the nonlinear crystal. Eqn. 2.10 is plotted in Fig. 2.5 for  $\Delta T = -\Delta k' L/2$ , and compared to the  $\sim 1 - |t|/T_p$  gain clipping function associated with flat-top pulses. Both functions are normalized by the gain associated with the peak of the field,  $\kappa A_{2\omega, 0} L$ . The essential difference between these two gain clipping functions is the slow variation of Eqn. 2.10 for  $|t| < \tau$  (Fig. 2.5(b)). This renders the reduction of the field gain due to timing mismatch negligible for small accumulated delays, which will become relevant in Sec. 2.5. We also note that for the example shown in Fig. 2.5 the peak of the gain clipping function is reduced to  $\sim 80\%$  of the peak value for a flat-top pulse of the same peak amplitude.

We close this section by addressing some subtle points about timing conventions that are greatly simplified using the gain clipping functions explored in this section. For all of the cases considered here, the gain clipping function is maximized at  $t = 0$  for the case of  $\Delta T = -\Delta k' L/2$ . Hereafter, this case will be referred to as symmetric temporal walk-off, where the unsaturated gain experienced by the fundamental at position  $z$  has even parity about  $L/2$ , given a pump pulse with even parity. This case serves as a natural reference point when considering the interplay between the fast dynamics that occur within the nonlinear crystal and the slow dynamics that occur over the course of a cavity round-trip. When considering propagation in the nonlinear crystal the signal pulse is most commonly used as a timing reference since this choice often simplifies the techniques used to solve the coupled wave equations. In the lab, and when considering the role of the timing mismatch, it is common to use the pump laser as the timing reference since this is the most readily available signal to compare any relative delay against. Accordingly, we define our origin of the slow cavity time coordinate in terms of the relative timing between the signal and the peak of the gain clipping function,  $T = \Delta T + \Delta k' L/2$ , which allows us to move seamlessly between these scales. For example, as described above, inside the nonlinear crystal  $T = 0$  corresponds to the case where the peaks of

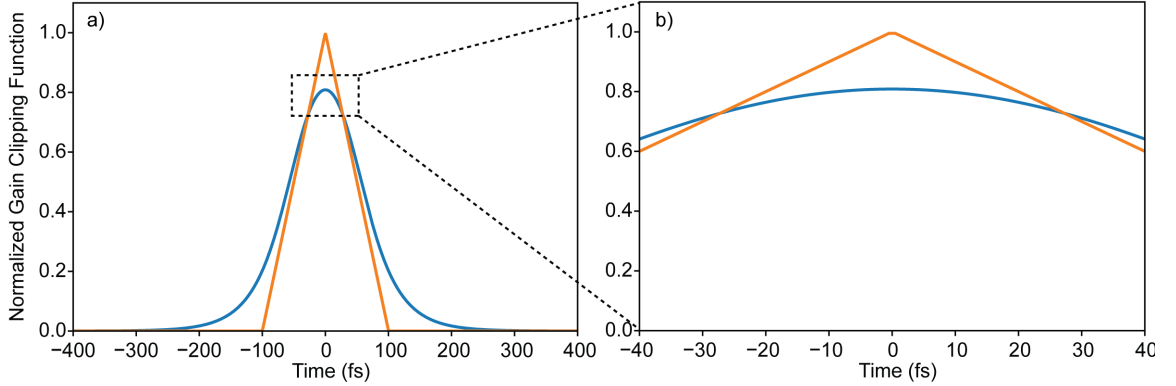


Figure 2.5: a) Comparison of  $\Gamma(L, t)$  for a flat-top pulse (orange) and a sech pulse (blue). The parameters chosen are  $\Delta k' L = T_p = 100$  fs, and  $\tau = 40$  fs, which corresponds to FWHM pulse duration of 70 fs. This choice of parameters corresponds to the experimental conditions studied in Sec. 2.3. b) The same comparison for  $-\tau < t < \tau$ , which shows that  $\Gamma(L, t)$  varies slowly for delays comparable to  $\tau$ .

the pump and signal begin with a relative delay of  $-\Delta k' L/2$ , and the signal gain is maximized. In the cavity, the synchronized case  $\ell = 0$  corresponds to zero shift of the relative timing on each round trip. Therefore, for an OPO with perfect synchronization and Eqn. 2.10 with  $T = 0$ , we expect the signal to form with a peak centered around  $t = 0$ .

#### 2.1.4 High Order Dispersion and the Transition to Non-degeneracy

Having established the role of synchronization and the pump pulses, we now consider the role of dispersion beyond the first order. There are two key results of this section, both determined largely by the second order dispersion of the linear feedback cavity and the nonlinear crystal. First, we will find that second order dispersion will determine the values of  $\ell$  that achieve degenerate operation. Second, we will find that for a degenerate resonance, second order dispersion will determine the amount of bandwidth that the OPO can generate. The analysis found here relies entirely on CW interactions, and will yield heuristic insights into the behavior of pulsed OPOs. We begin by solving the coupled wave equations for an arbitrary three wave interaction, assuming that the pump wave  $\omega_p = \omega_s + \omega_i$  is undepleted. The evolution of the signal and idler are given as

$$\partial_z A_s = -i \left( \frac{k''_\omega}{2} \Omega^2 + \frac{k'''_\omega}{6} \Omega^3 \right) A_s + \gamma_0 A_i^* \quad (2.11a)$$

$$\partial_z A_i = -i \left( \frac{k''_\omega}{2} \Omega^2 - \frac{k'''_\omega}{6} \Omega^3 \right) A_i + \gamma_0 A_s^* \quad (2.11b)$$

where  $\omega_s = \omega_p/2 + \Omega$ ,  $\omega_i = \omega_p/2 - \Omega$ , and we have assumed phase-matching at  $\Omega = 0$ . As before, the unsaturated gain coefficient is  $\gamma_0 = \kappa|A_p(0)|$  and we have chosen the phase convention of the pump wave such that  $\gamma_0$  is real.  $k''_\omega$ , and  $k'''_\omega$  are phase contributions from the first two terms of the dispersion operator  $\hat{D}_\omega$ , both of which are evaluated at  $\omega_p/2$ . This system of linear ordinary differential equations for  $A_s$  and  $A_i$  is solved using a matrix exponent,

$$\begin{bmatrix} A_s(L) \\ A_i^*(L) \end{bmatrix} = \exp(i\phi_{o,x}) \exp \begin{pmatrix} i\phi_{e,x} & \gamma_0 L \\ \gamma_0 L & -i\phi_{e,x} \end{pmatrix} \begin{bmatrix} A_s(0) \\ A_i^*(0) \end{bmatrix}, \quad (2.12)$$

where  $\phi_{e,x}$  contains even dispersion orders of the nonlinear crystal and  $\phi_{o,x}$  contains the odd dispersion orders.  $\phi_{e,x} = -k''_\omega L \Omega^2/2$  to second order in  $\Omega$ , and  $\phi_{o,x} = -k'''_\omega L \Omega^3/6$  to third order in  $\Omega$ . Adding in the cavity, after one trip  $A_s$  and  $A_i^*$  are mapped by the matrix

$$\begin{bmatrix} A_s^{n+1}(0) \\ (A_i^{n+1})^*(0) \end{bmatrix} = r e^{i\phi_o} \begin{pmatrix} e^{i\phi_{e,c}} & 0 \\ 0 & e^{-i\phi_{e,c}} \end{pmatrix} \exp \begin{pmatrix} i\phi_{e,x} & \gamma_0 L \\ \gamma_0 L & -i\phi_{e,x} \end{pmatrix} \begin{bmatrix} A_s^n(0) \\ (A_i^n)^*(0) \end{bmatrix}. \quad (2.13)$$

$\phi_{e,c} = -\pi\ell - \phi''_c \Omega^2/2$  contains the even dispersion orders of the cavity, and  $\phi_o = \phi_{o,x} + \phi_{o,c}$  contains the odd dispersion orders of both the cavity and crystal, with  $\phi_{o,x} = -\Delta T_{\text{RT}} \Omega - \phi'''_c \Omega^3/6$ . We can solve for the eigenvalues of  $M$  using the trace  $2T$  and determinant  $D$ ,

$$\lambda_{\pm} = T(1 \pm \sqrt{1 - (D/T)^2}), \quad (2.14)$$

where the determinant is given by

$$\lambda_+ \lambda_- = r^2 e^{2i\phi_o} = D^2. \quad (2.15)$$

We remark that since  $|D|^2 < 1$ , only one of  $\lambda_{\pm}$  may be greater than 1. Oscillation is then determined by the range of  $\Omega$  and  $\ell$  that exhibit  $\lambda_+ > 0$ . The trace is

$$T = \frac{\lambda_+ + \lambda_-}{2} = r e^{i\phi_o} \left[ \cos(\phi_{e,c}) \cosh(\gamma L) - \frac{\phi_{e,x}}{\gamma L} \sin(\phi_{e,c}) \sinh(\gamma L) \right] \quad (2.16)$$

Where  $\gamma L = \sqrt{(\gamma_0 L)^2 - \phi_{e,x}^2}$ . Since  $D/T$  is real, the roles of the even and odd cavity phase decouple into two distinct effects, as determined by Eqn. 2.14. The role of the even dispersion orders is to determine the frequency dependence of the gain, which in turn determines both the operating regime of the OPO and the bandwidth that the OPO may oscillate with. We consider these effects in two limits, low and high gain. For a low gain OPA ( $\gamma_0 L \leq 1$ )

$$\lambda_+(\ell, \Omega) \approx \lambda_{+,0} \cos(\pi\ell + (\phi''_c + k''_\omega L)\Omega^2/2), \quad (2.17)$$

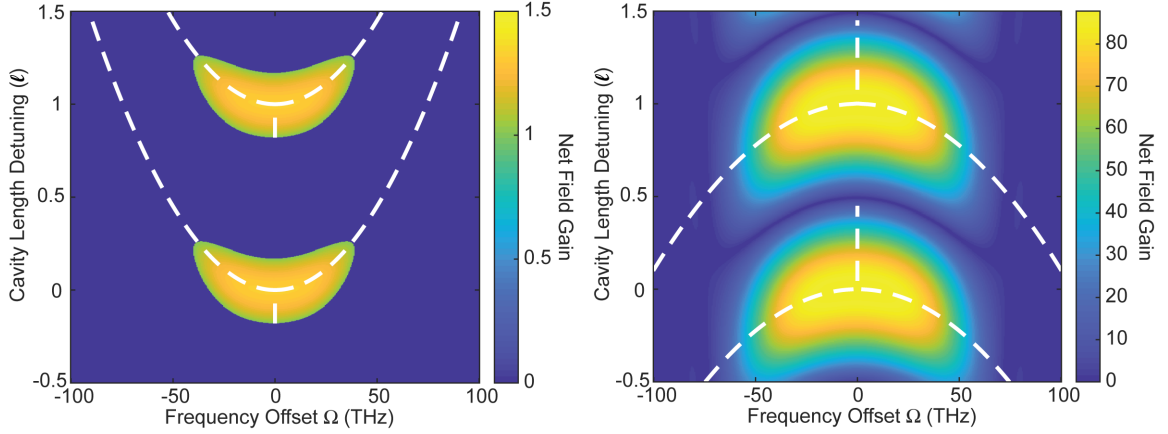


Figure 2.6: The OPO eigenvalue, plotted for a)  $\gamma_0 L = 0.8$  and b) an extreme limit,  $\gamma_0 L = 5$ . The OPO has  $k''_\omega L = -53 \text{ fs}^2$ ,  $\phi''_c = 25 \text{ fs}^2$ ,  $\lambda_p = 1045 \text{ nm}$ , and  $R = 35\%$ . Dotted lines denote the resonance conditions, Eqn. 2.17 and Eqn. 2.18, respectively.

where  $\lambda_{+,0} = r \exp(\gamma_0 L + i\phi_o)$ . For a high gain OPA, where  $\gamma_0 L \geq 1$ , Eqn. 2.14 becomes

$$\lambda_+(\ell, \Omega) \approx \lambda_{+,0} \cos \left( \pi\ell + \left( \phi''_c + \frac{k''_\omega L}{\gamma_0 L} \right) \Omega^2 / 2 \right). \quad (2.18)$$

Eqns. 2.14-2.18 contain the main results of this section, which can be used to determine the OPO operation regime and bandwidth. The operating regime is determined by the number of global maxima for a given  $\ell$  in equations 2.17 and 2.18. For a low gain OPO, nondegenerate operation occurs when  $\text{sgn}(\ell) = -\text{sgn}(\phi''_c + k''_\omega L)$ , which results in two local maxima around  $\Omega^2 = -2\pi\ell / (\phi''_c + k''_\omega L)$ . A similar condition exists for a high gain OPO, where the phase-matching bandwidth of the nonlinear crystal is now modified due to gain narrowing,  $k''_\omega \rightarrow k''_\omega / (\gamma_0 L)$ . The gain of the OPO as determined by the eigenvalue  $\lambda_+(\ell, \Omega)$  is plotted in Fig. 2.6, as a function of cavity detuning and optical frequency. The dotted white lines denote the signal frequency derived from equations 2.17 and 2.18, which show strong agreement with the local maxima determined numerically. Degenerate operation is favored for cavity lengths where the gain around  $\Omega = 0$  exceeds that of the signal and idler frequencies denoted by the white lines. We note here that the effect of the odd dispersion orders of the cavity is to give an opposite rotation to the signal and idler phases on every round trip, which renders their carrier-envelope-offset frequencies a function of cavity length detuning. When the gain favors splitting off into a signal/idler with carrier frequencies given by  $\pm\Omega_{\text{max}}$ , the signal and idler comb acquire a phase shift on each round trip that offsets their combs lines from the degenerate comb by a frequency splitting  $\Delta_{\pm} = \pm\phi_o(\ell, \Omega_{\text{max}})f_R / (2\pi)$ .

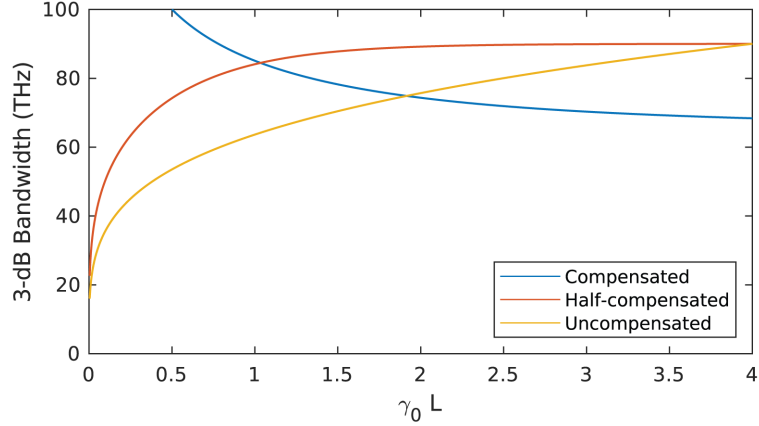


Figure 2.7: 3-dB bandwidth of  $\lambda_+(0)$  as a function of unsaturated OPA gain for the three cavity designs described in the text. Half-compensated cavities with  $\phi_c'' = -\phi_x''/2$  achieve the most bandwidth for  $1 < \gamma_0 L < 4$ .

Eqs. 2.14 - 2.16 also determine the possible bandwidth that the OPO can generate. In the center of each resonance,  $\ell \in Z$ , Eqn. 2.14 can be approximated to lowest order in  $\Omega$  as

$$\lambda_+(\ell, \Omega) = r e^{\gamma_0 L} \left( 1 - \left( \frac{\Omega^2}{2} \right)^2 \frac{(\phi_c'' + \phi_x'')^2 + \phi_c''^2 [\gamma_0 L \coth(\gamma_0 L) - 1]}{2\gamma_0 L} \right). \quad (2.19)$$

This suggests three useful heuristics for the design of the intracavity dispersion. In the limit of low gain, where  $\gamma_0 L \ll 1$ , a dispersion-compensated cavity with  $\phi_c'' = -\phi_x''$  gives unlimited phase-matching bandwidth. This suppresses the effects of dispersion in a high finesse cavity operating near threshold, but results in a bandwidth that decreases with increasing gain. For moderate to high gain OPOs, where  $\gamma_0 L > 1$ , a half-compensated cavity with  $\phi_c'' = -\frac{1}{2}\phi_x''$  results in broadband gain that is invariant for increasing  $\gamma_0 L$ . Finally, for extraordinarily high gain OPOs ( $\gamma_0 L > 5$ ) the bandwidth increases monotonically with increasing  $\gamma_0 L$  when  $\phi_c'' = 0$ . The 3-dB bandwidth of  $\lambda_+(\ell, \Omega)$  is plotted in Fig. 2.7 for each of the three cavity designs considered here. Dispersion compensated cavities achieve the most bandwidth for  $\gamma_0 L \leq 1$ , half-compensated cavities achieve the most bandwidth when  $1 \leq \gamma_0 L \leq 4$ , and uncompensated cavities achieve the most bandwidth for  $\gamma_0 L > 4$ . The OPOs we study experimentally in Sec. 2.3 correspond to  $1 \leq \gamma_0 L \leq 3$ , and employ half-compensated cavities.

We close this section by noting that the range of  $\Omega$  that satisfies  $\lambda_+(\ell, \Omega) > 1$  constrains the possible bandwidth that an OPO may generate. In practice, this criterion alone is not sufficient to determine the bandwidth generated by OPOs. For example, all of the cases considered here suggest that OPOs produce more bandwidth with increasing times above threshold, but in practice many OPOs produce less bandwidth as they are driven further above threshold. To better understand

these behaviors we need to model pulse formation mechanisms in OPOs.

## 2.2 Pulse Formation in OPOs

The pulses formed during steady state operation in an OPO occur as a balance between competing effects such as gain clipping, dispersion, saturation, and asynchronization. In steady state, the pulse circulating in the cavity must reproduce itself on every round trip of the cavity  $A_s^{m+1}(0, t) = A_s^m(0, t) = rA_s^m(L, t)$ , where 0 and  $L$  refer to the input and output of the nonlinear crystal. Our task is to find the pulse profile  $A_s(0, t)$  such that the equations for steady state and the coupled wave equations in the OPA crystal are satisfied. In this section, we consider the theory of pulse formation in two experimentally relevant regimes: box pulses and simultons. Box pulses are the most common operating regime in OPOs and form due to balance between saturation and gain clipping. Simultons represent a recently discovered operating regime in OPOs, and form due to a balance between asynchronization and saturation. We will see that these two regimes exhibit rather different scaling laws, with box pulses losing bandwidth as the pump power increases, whereas simultons achieve more bandwidth with increasing pump power.

### 2.2.1 Box Pulse Theory

This section considers the most common example of pulse formation, which occurs as a balance between gain clipping and saturation. The pulses that form in this limit are typically flat-top in profile, and accordingly this model is called the box pulse theory[59]. This section will yield a number of insights about common OPO behaviors, including the typical shape of the output optical spectrum as a function of cavity length detuning. Most importantly, we will find that when an OPO operates in the box pulse regime the bandwidth output from the OPO decreases with increasing pump power.

The process used here is as follows. First, we assume gain without distortion  $A_s(z, t) = \exp(\gamma_{av}z)\bar{A}_s(z, t)$ , such that  $\bar{A}_s$  is slowly varying in  $z$  and  $r \exp(\gamma_{av}L) = 1$ . Then, we use the gain-without-distortion ansatz to solve the coupled wave equation for the second harmonic, accounting for both saturation and temporal walk-off. This solution is then used in the coupled wave equation for the fundamental to generate a system of linear equations that can be solved for the steady-state pulse shape  $\bar{A}_s(z, t)$ .

We begin by solving Eqn. 2.7b from Sec. 2.1.3 to account for pump depletion. Using the method of characteristics, we find

$$A_p(z, t) = A_p(0, t - \Delta k'z) - \kappa \int_0^z A_s^2(z', t + \Delta k'(z - z')) dz'. \quad (2.20)$$

We now invoke the gain-without-distortion ansatz to relate the signal at  $z'$  to the signal at  $z$ ,

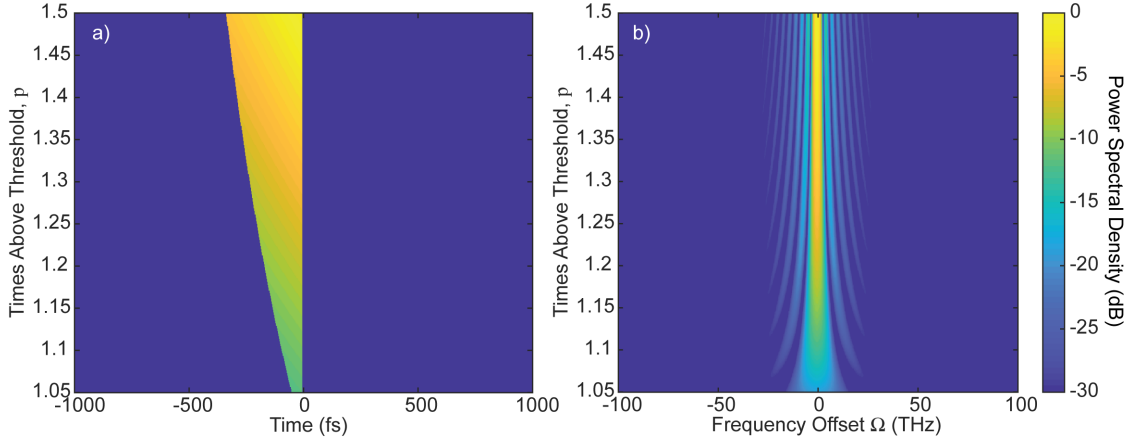


Figure 2.8: Pulse formation in an OPO with competition between saturation and gain clipping as the dominant pulse formation mechanisms. a) Pulse shape  $\bar{A}_s^2(t, p)$  according to Eqn. 2.26, and b) the power spectral density for various times above threshold. For the plots shown here  $R = 35\%$ , and  $T_p = 1$  ps. We note that the pulse duration grows larger and loses bandwidth with increasing times above threshold,  $p$ , defined in the text above Eqn. 2.27.

$A_s(z', t) = \exp(\gamma_{\text{av}}(z' - z)) A_s(z, t)$ , and make the change of variables  $t' = t + \Delta k'(z - z')$  to find

$$A_p(z, t) = A_p(0, t - \Delta k'z) - \frac{\kappa}{\Delta k'} \int_{t - \Delta k'z}^t \exp\left(\frac{\gamma_{\text{av}}}{\Delta k'}(t' - t)\right) A_s^2(z, t') dt'. \quad (2.21)$$

We can often take the lower bound of the integral in Eqn. 2.21 to be  $-\infty$  since the integrand decays rapidly as  $t' \rightarrow -\infty$ . Substituting Eqn. 2.21 into Eqn. 2.7a for the fundamental, and assuming  $A_s(z, t)$  is real yields

$$\partial_z A_s(z, t) = \kappa A_s \left[ A_p(0, t - \Delta k'z) - \frac{\kappa}{\Delta k'} \int_{-\infty}^t \exp\left(\frac{\gamma_{\text{av}}}{\Delta k'}(t' - t)\right) A_s^2(z, t') dt' \right]. \quad (2.22)$$

We note here that for a flat-top pump, the signal experiences gain when  $\Delta k'z$  is smaller than the pulse duration of the pump  $T_p$ . When  $\Delta k'z > T_p$ , the signal begins to experience loss due to back-conversion. For these reasons, we typically choose  $\Delta kL = T_p$  for a flat-top and  $\Delta k'L \sim 2\tau - 3\tau$  for a sech-pulse. Assuming the gain-without-distortion ansatz,  $A_s(z, t) = \exp(\gamma_{\text{av}}z) \bar{A}_s$ , we find

$$\frac{\partial_z \bar{A}_s(z, t)}{\bar{A}_s(z, t)} = \kappa A_p(0, t - \Delta k'z) - \gamma_{\text{av}} - \frac{\kappa^2 \exp(2\gamma_{\text{av}}z)}{\Delta k'} \int_{-\infty}^t \exp\left(\frac{\gamma_{\text{av}}}{\Delta k'}(t' - t)\right) \bar{A}_s^2(z, t') dt'. \quad (2.23)$$

Integrating both sides with respect to  $z$  and approximating  $\bar{A}_s(z, t') \approx \bar{A}_s(0, t') = \bar{A}_s(t')$  on the

right hand side yields

$$\bar{A}_s(t) = \bar{A}_s(t) \exp \left[ F(L, t) - C \int_{-\infty}^t \exp \left( \frac{\gamma_{\text{av}}}{\Delta k'} (t' - t) \right) \bar{A}_s^2(z, t') dt' \right], \quad (2.24)$$

where  $F(L, t) = \Gamma(L, t) - \gamma_{\text{av}}L$  is the gain clipping function minus the saturated gain, and we introduce  $C = \kappa^2 (\exp(2\gamma_{\text{av}}L) - 1) / (2\gamma_{\text{av}}\Delta k')$  to make Eqn. 2.24 more readable. There are two ways for Eqn. 2.24 to be satisfied for a given value of  $t$ . If  $F(L, t) < 0$  or  $\partial_t F(L, t) < 0$ , then there is no way to set the argument of the exponent to zero since the integral on the right hand side of Eqn. 2.24 is both positive and increasing. In this case,  $\bar{A}_s(t) = 0$ . If  $F(L, t) > 0$  and  $\partial_t F(L, t) > 0$ , then we may set both the argument of the exponential and its time derivative to zero to generate a system of linear equations for  $A_s^2(t)$ ,

$$0 = F(L, t) - C \exp \left( \frac{-\gamma_{\text{av}}t}{\Delta k'} \right) \int_{-\infty}^t \exp \left( \frac{\gamma_{\text{av}}t'}{\Delta k'} \right) \bar{A}_s^2(z, t') dt', \quad (2.25a)$$

$$C\bar{A}_s^2(z, t) = \partial_t F(L, t) + \frac{C\gamma_{\text{av}}}{\Delta k'} \exp \left( \frac{-\gamma_{\text{av}}t}{\Delta k'} \right) \int_{-\infty}^t \exp \left( \frac{\gamma_{\text{av}}t'}{\Delta k'} \right) \bar{A}_s^2(z, t') dt', \quad (2.25b)$$

Solving Eqns. 2.25a-2.25b yields

$$\bar{A}_s^2(t) = \frac{2\gamma_{\text{av}}^2}{\kappa^2(\exp(2\gamma_{\text{av}}L) - 1)} \left[ F(L, t) + \frac{\Delta k'}{\gamma_{\text{av}}} \partial_t F(L, t) \right]. \quad (2.26)$$

Eqn. 2.26 is the main result of this section, which allows for the calculation of  $\bar{A}_s(t)$  in the limit where saturation and gain clipping are the dominant pulse shaping mechanisms.

As an example, we now consider an OPO driven by flat-top pulses with  $T_p = \Delta k' L$ , such that  $\Gamma(L, t) = \kappa L(1 - |t|/T_p)A_{2\omega, 0}$ . In this case, when  $\bar{A}(z, t)$  is nonzero we have  $F(L, t) = \kappa L(1 - |t|/T_p)A_{2\omega, 0} - \gamma_{\text{av}}L$  and  $\Delta k' \partial_t F(L, t)/\gamma_{\text{av}} = \kappa A_{2\omega, 0}/\gamma_{\text{av}}$ . If we define  $\kappa A_{2\omega, 0} = p\gamma_{\text{av}}$ , where  $p^2 = M$  is the usual times above threshold for a CW OPO with pump power equal to the peak power of the pump pulse and a field loss coefficient equal to  $\gamma_{\text{av}}$ , then

$$\bar{A}_s^2(t) = \frac{2\gamma_{\text{av}}^2}{\kappa^2(\exp(2\gamma_{\text{av}}L) - 1)} \left[ p + \gamma_{\text{av}}L \left( (p-1) - p \frac{|t|}{T_p} \right) \right], \quad (2.27)$$

for  $-T_p(1 - p^{-1}) < t < 0$ , and  $\bar{A}_s(t) = 0$  otherwise. In terms of  $\gamma_{\text{av}}L = -\ln(r)$ ,

$$\bar{A}_s^2(t) = \frac{2r^2 \ln^2(r)}{(\kappa L)^2(1 - r^2)} \left[ p - \ln(r) \left( (p-1) - p \frac{|t|}{T_p} \right) \right]. \quad (2.28)$$

Eqn. 2.28 is shown in Fig. 2.8(a) for varying  $p$ . The power spectral density associated with each pulse is shown in Fig. 2.8(b). As the OPO is driven further above threshold, the range of  $t$  that is above threshold increases, resulting in longer pulses with less bandwidth.

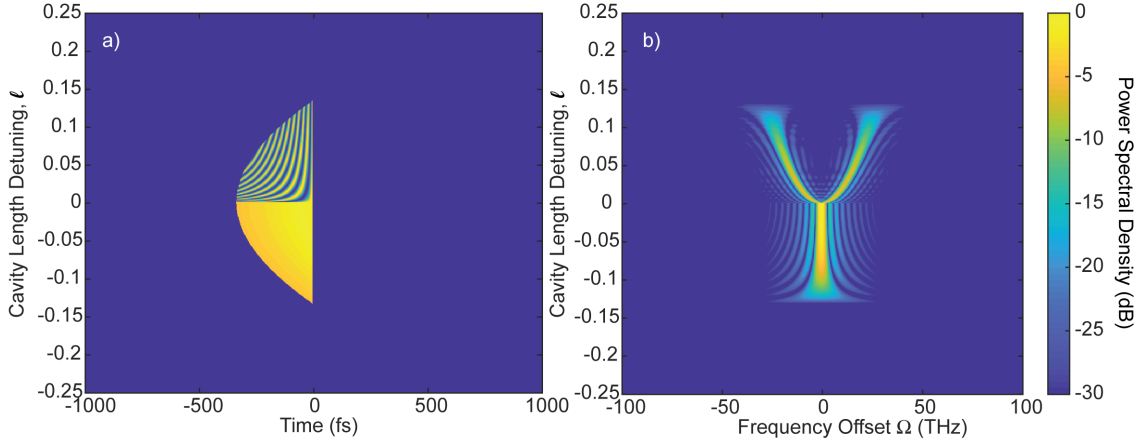


Figure 2.9: The role of cavity length detuning in pulse formation. a) Pulse shape  $\bar{A}_s^2(t, \ell)$ , and b) the power spectral density for various cavity length detunings. The plots shown have the same parameters as Fig. 2.9, but with the times above threshold fixed at  $p = 1.5$ , and with a crystal and cavity group delay dispersion of  $k''_{\omega}L = -53 \text{ fs}^2$  and  $\phi''_c = 25 \text{ fs}^2$ , respectively. For  $\ell > 0$ , the OPO transitions to nondegenerate operation. We note here that the pump pulse duration of 1 ps was chosen to produce a small bandwidth, such that the frequency splitting for  $\ell > 0$  is easily visualized.

We may also consider pulse formation in a detuned cavity simply by modifying the gain according to Eqn. 2.17, in which case  $F(L, T)$  appearing in Eqns. 2.25a-2.25b becomes  $F(L, T) = \kappa LA_{2\omega, 0} (\cos(\pi\ell + (\phi''_c + k''_{\omega}L)\Omega^2/2) - |t|/T_p) - \gamma_{\text{av}}L$ , and  $\bar{A}_{s, \Omega}(t) = \bar{A}_s(t) \cos(\Omega t)$ . The results are plotted in Fig. 2.9 as a function of  $\ell$  for  $p = 1.5$ . As the cavity length detuning crosses  $\ell = 0$ , the OPO transitions from degenerate to non-degenerate operation, resulting in a bimodal spectrum. While we have used a 1 ps pump pulse in these calculations to exaggerate the features of a box pulse, the behaviors seen here are general of any OPO operating in the box pulse regime.

## 2.2.2 Temporal solitons in Optical Parametric Oscillators

When gain clipping and dispersion are negligible, the dominant pulse formation mechanisms are due to asynchronization and gain saturation. In this limit, where an OPO is intentionally operated with a timing mismatch, steady state may occur when the fundamental and second harmonic form temporal solitons, i.e. coupled bright-dark signal-pump solitons. Remarkably, OPOs operating in the soliton regime achieve higher conversion efficiencies and more bandwidth than similar OPOs operating in the box pulse regime. This runs contrary to the conventional wisdom that OPOs achieve the highest conversion efficiencies and broadest bandwidths when perfectly synchronized. We treat soliton formation in three steps. First, we derive the steady state soliton, which is a co-propagating bright-dark soliton that forms in saturated OPAs. We will see that temporal solitons propagate with larger group velocities than either the pump or the signal in the absence

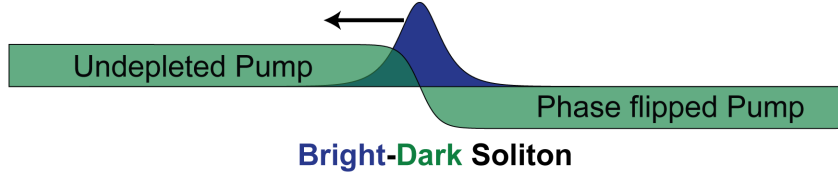


Figure 2.10: A temporal simulton. The bright sech soliton (blue) at frequency  $\omega$  walks through the undepleted  $2\omega$  pump (green). The signal depletes the pump, forming a co-propagating tanh dark soliton, and leaving behind a tail of phase-flipped pump. We note here that the signal walks off to the left, since higher velocities correspond to moving earlier in time.

of gain saturation. Then, we generalize this solution to allow for gain and loss. Finally, we formulate steady state as a double balance: the saturated gain equals the intracavity loss, and the total group advance accumulated by the simulton cancels the timing mismatch between the pump and the cavity.

In the absence of loss temporal simultons are simultaneous bright-dark solitons of the signal at  $\omega$  and the pump at  $2\omega$ , which occur in a degenerate traveling wave OPA due to group velocity mismatch and gain saturation[63, 64]. As with Sec. 2.1.3, we consider coupled wave equations for phase-matched OPA, neglecting dispersion beyond first order

$$\partial_z A_\omega(z, t) = \kappa A_{2\omega} A_\omega^*, \quad (2.29a)$$

$$\partial_z A_{2\omega}(z, t) = -\Delta k' \partial_t A_{2\omega} - \kappa A_\omega^2, \quad (2.29b)$$

where we have again shifted the time coordinate to be co-moving with the group velocity of the signal wave, and include a  $\pi/2$  phase in the pump envelope to make the equations of motion and their solutions real. We may find the simulton solution by assuming a solitary wave with inverse group velocity  $\nu$ , such that  $A_\omega(z, t) = A_\omega(t + \nu z)$  and  $A_{2\omega}(z, t) = A_{2\omega}(t + \nu z)$ . This ansatz yields a system of equations with the same form as the CW coupled wave equations for SHG,

$$\nu \partial_t A_\omega(t) = \kappa A_{2\omega} A_\omega^*, \quad (2.30a)$$

$$(\nu + \Delta k') \partial_t A_{2\omega}(t) = -\kappa A_\omega^2. \quad (2.30b)$$

The simulton solution of a traveling wave OPA is given by [63, 64]

$$A_\omega(z, t) = \frac{a}{\sqrt{2\tau}} \operatorname{sech} \left( \frac{t - T}{\tau} \right), \quad (2.31a)$$

$$A_{2\omega}(z, t) = -A_{2\omega,0} \tanh \left( \frac{t - T}{\tau} \right), \quad (2.31b)$$

where  $a^2 = 2(\Delta k' + \gamma_0 \tau) \gamma_0 / \kappa^2$  is the signal pulse energy,  $\tau$  is the pulse duration,  $T = -\gamma_0 \tau z$  represents a time shift in the signal pulse relative to linear propagation due to gain saturation, and

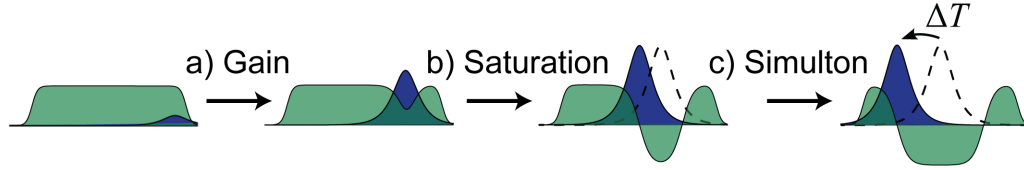


Figure 2.11: Evolution of pump and signal fields in an OPA from the linear to the simulton regimes. a) In the unsaturated regime, the signal initially experiences linear parametric gain. b) Upon reaching the simulton energy, the signal saturates the pump and the pair form a simulton. c) The simulton propagates without extracting any additional gain, but accumulates a total group advance  $\Delta T$  due to the increased group velocity of a simulton. Dotted line: the evolution of the signal field undergoing linear temporal walkoff.

$\gamma_0 = \kappa A_{2\omega,0}$  is the small-signal gain coefficient. Simultons occur when the leading edge of a bright  $\text{sech}^2$  signal pulse depletes a quasi-continuous wave pump, and the trailing edge converts back to the pump frequency through second harmonic generation with a  $\pi$  phase relative to the undepleted pump (Fig. 2.10). The pump forms a  $\tanh^2$  dark soliton coupled to the bright  $\text{sech}^2$  signal pulse, and the pair co-propagate with an intensity-dependent velocity that exceeds that of either wave,  $\nu \equiv v_{g,\text{sim}}^{-1} = v_{g,\omega}^{-1} - \gamma_0 \tau$ .

We now generalize this solution to include gain and loss using the manifold projection method described in [59]. First, we assume  $A_{\text{sim}}(z, t)$  is described by Eqn. 2.31a, where  $a(z)$ ,  $T(z)$ , and  $\tau(z)$  are now allowed to evolve during propagation. We follow the same assumptions as the gain clipped case to account for saturation. Starting from Eqn. 2.21,

$$\partial_z A_\omega(z, t) = \kappa A_{2\omega}(0, t - \Delta k' z) A_\omega(z, t) - \frac{\kappa^2}{\Delta k'} A_\omega(z, t) \int_{-\infty}^t A_\omega^2(z, t') dt', \quad (2.32)$$

we may substitute our ansatz for  $A_\omega(z, t)$  and assume small gain per walk-off. We also approximate the pump envelope as a constant that yields the same gain per walk-off as the peak of the gain clipping function,  $A_{2\omega}(z, t) = \Gamma(L, 0)/\kappa L$ , with the definition of  $\Gamma(L, 0)$  from Eqn. 2.10. In this case, the coupled wave equations reduce to

$$\partial_z A_\omega(z, t) = \kappa A_{2\omega,0} \frac{a(z)}{\sqrt{2\tau(z)}} \text{sech}\left(\frac{t - T(z)}{\tau(z)}\right) - \frac{\kappa^2 a^3(z)}{2\Delta k' \sqrt{2\tau(z)}} \left(\tanh\left(\frac{t - T(z)}{\tau(z)}\right) - 1\right). \quad (2.33)$$

We define  $f(z, t) = \partial_z A_\omega(z, t)$  from Eqn. 2.33 for notational clarity. To obtain the evolution of the parameters  $a(z)$ ,  $\tau(z)$ , and  $T(z)$ , we need to find  $\partial_z a$ ,  $\partial_z T$ , and  $\partial_z \tau$  that minimize the error function,  $\int |f(z, t) - d_z A_{\text{sim}}|^2 dt$ , where the total derivative of our ansatz with respect to  $z$  is given by

$$d_z A_{\text{sim}}(z, t) = \partial_a A_{\text{sim}} \partial_z a + \partial_T A_{\text{sim}} \partial_z T + \partial_\tau A_{\text{sim}} \partial_z \tau. \quad (2.34)$$

We may find equations for  $\partial_z \xi$ , where  $\xi \in \{a, T, \tau\}$ , by approximating  $\partial_z A_{\text{sim}}$  in Eqn. 2.34 as  $f(z, t)$ ,

multiplying by  $\partial_\xi A_{\text{sim}}$ , and integrating with respect to time to generate a system of equations for  $\partial_z a$ ,  $\partial_z T$ , and  $\partial_z \tau$ . The derivatives of  $A_{\text{sim}}$  with respect to the parameters  $a$ ,  $T$ , and  $\tau$  are orthogonal to one another given the inner product defined above, which leads us to the projection rules

$$\partial_z \xi = \frac{\int f(z, t) \partial_\xi A_{\text{sim}}(z, t) dt}{\int \partial_\xi A_{\text{sim}}(z, t) \partial_\xi A_{\text{sim}}(z, t) dt}. \quad (2.35)$$

Using Eqn. 2.33 with Eqn. 2.35 results in the evolution of  $a$ ,  $T$ , and  $\tau$

$$\partial_z a = \gamma_0 a \left[ 1 - \frac{a^2}{a_{\text{sim}}^2} \right], \quad (2.36a)$$

$$\partial_z T = -\gamma_0 \tau \frac{a^2}{a_{\text{sim}}^2}, \quad (2.36b)$$

$$\partial_z \tau = 0, \quad (2.36c)$$

where  $a_{\text{sim}}^2 = 2\Delta k' \gamma_0 / \kappa^2$  is the simulton energy. Eqns. 2.36a-2.36c can be understood in two limits. When  $a \ll a_{\text{sim}}$  we recover the evolution of a degenerate OPA with an undepleted pump. The signal is amplified as  $a(z) = a(0)e^{\gamma_0 z}$ , and propagates with a linear group velocity, i.e.  $\partial_z T = 0$ . When  $a = a_{\text{sim}}$  we recover the simulton solution given by Eqns. 2.31a-2.31b. In the limit of the approximations made here, the simulton solution is a stable attractor. If a sech signal pulse is seeded into a degenerate OPA such that  $a > a_{\text{sim}}$ , it will transfer energy to the pump through SHG until the simulton solution is reached. Eqns. 2.36a-2.36b can be solved for the full evolution of a dissipative simulton, resulting in:

$$a(z) = \frac{a(0)e^{\gamma_0 z}}{\sqrt{1 + \frac{a^2(0)}{a_{\text{sim}}^2} (e^{2\gamma_0 z} - 1)}}, \quad (2.37a)$$

$$\Delta T(z) = \tau \ln \left( \frac{a(0)e^{\gamma_0 z}}{a(z)} \right). \quad (2.37b)$$

$\Delta T(z) = T(z) - T(0)$  is the shift in group delay accumulated due to nonlinear acceleration in a single pass through the OPA crystal. A schematic of simulton formation is illustrated in Fig. 2.11, showing the evolution of the pump and signal fields in an OPA from the linear to the simulton regimes. The signal is seen to undergo linear temporal walkoff due to group velocity mismatch and extract gain until the pump is depleted. Once depleted, the pump forms a co-propagating dark soliton, and the pair propagates at the simulton velocity.

Fig. 2.12 shows the dynamics of a simulton OPO. On each round trip, a new pump pulse enters the cavity through the input coupler, M1, and the signal accumulates a small group delay  $\Delta T_{\text{RT}}$  (Fig. 2.12(a)), due to the timing mismatch. After passing through the PPLN crystal, the signal is amplified, and accumulates a simulton group advance  $\Delta T$  (Fig. 2.12(b)). The signal is partially out-coupled through M4, with a fraction  $R$  of the power returning to M1. Simulton formation

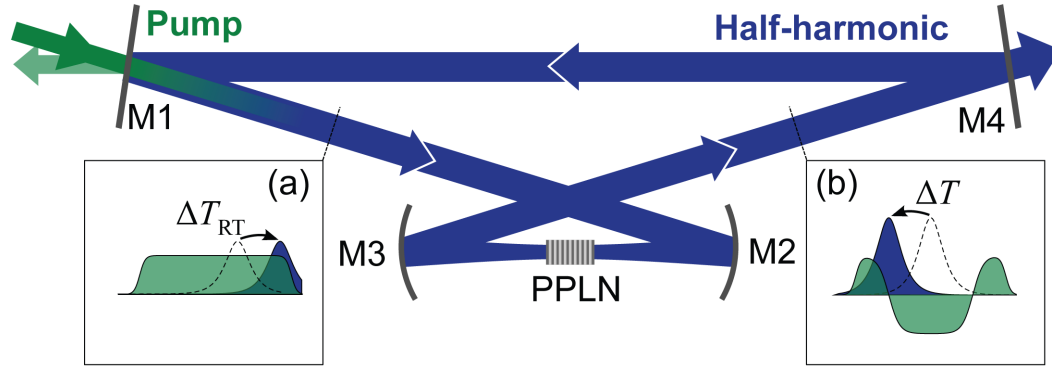


Figure 2.12: Simulton formation in a synchronously pumped OPO cavity. (a-b) Displacement of intracavity signal relative to a perfectly synchronous half-harmonic pulse undergoing linear propagation (dotted lines) (a) After M1 the signal acquires a small delay,  $\Delta T_{RT}$ , relative to the incoupled pump due to the timing mismatch. (b) After optical parametric amplification the signal acquires a nonlinear shift in group delay  $\Delta T$  due to simulton formation, which compensates the timing mismatch  $\Delta T_{RT}$ .

in an OPO is a double balance of energy and timing in which the gain extracted over an OPA crystal of length  $L$  balances the cavity loss,  $a^2(0) = Ra^2(L)$ , and the simulton acceleration balances the timing mismatch,  $\Delta T(L) = \Delta T_{RT}$ . When the timing condition is satisfied, the signal becomes synchronous with the pump and forms a half-harmonic pulse which inherits both its carrier-envelope offset frequency and comb spacing from the pump. The equations for steady state, with Eqs.(2.37a-2.37b) determine the simulton pulsewidth:

$$\tau = \frac{2\Delta T_{RT}}{2\gamma_0 L + \ln(R)}. \quad (2.38)$$

The pulsewidth of a simulton OPO is seen to shrink with increasing pump power, in contrast to the box pulse scaling developed in [59]. For positive detunings ( $\Delta T_{RT} > 0$ ), the simulton group advance allows for the formation of half-harmonic pulses which are synchronous with the pump at multiple cavity lengths. Negatively detuned ( $\Delta T_{RT} < 0$ ) simultons cannot form when  $\Delta k' > 0$  since pump depletion only provides a group advance for the signal pulse. Instead, the OPO operates in a non-degenerate regime analyzed in [59]. The timing mismatch is thus a critical design parameter which determines both the mode of operation and the bandwidth of the OPO.

The theoretical treatment of box pulses and simultons presented throughout this section is sufficient for many synchronously pumped OPOs. We summarize the main insights from this analysis here: i) threshold is given by the condition  $2\Gamma(L, 0) > (\ln(1/R))^2$ , where the gain clipping function  $\Gamma$  is defined in Eqn. 2.8. For flat-top pulses, this condition reduces to  $2\kappa A_{2\omega, 0} L > (\ln(1/R))^2$ , where

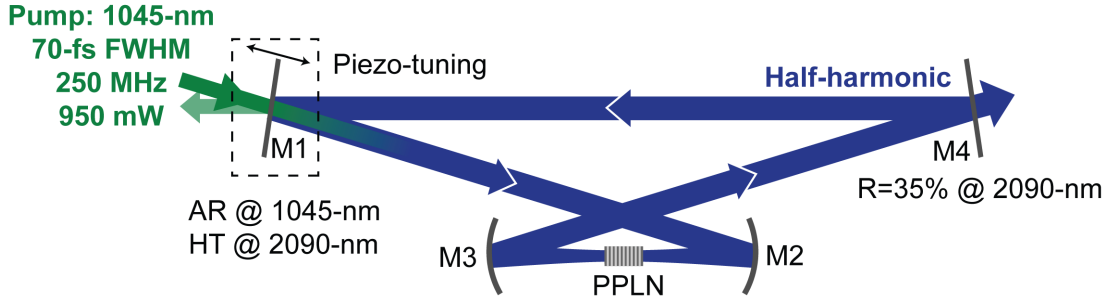


Figure 2.13: Design of the synchronously pumped OPOs used throughout this chapter[27, 60]. Pump pulses are in-coupled through M1, and the generated signal is out-coupled through M4. Mirrors M2 and M3 focus the pump and resonant signal into the PPLN crystal resulting in  $1/e^2$  beam-waists of  $10\text{-}\mu\text{m}$  and  $14\text{-}\mu\text{m}$ , respectively. Cavity length adjustments are made by mounting M1 on a piezo stage.

$A_{2\omega,0}$  is the peak field of the pump pulse. The peak gain is slightly reduced for sech pulses. ii) OPOs exhibit a transition from degenerate to non-degenerate operation, which depends on the relative sign of cavity length detuning and  $k''_{\omega}$ , as discussed in Sec. 2.1.4. iii) When an OPO achieves degenerate operation, the generated signal comb is frequency locked to the pump comb,  $f_{\text{ceo},s} = f_{\text{ceo},p}/2$ . iv) In steady state, degenerate OPOs form pulses due to an interplay of competing mechanisms. In the case where gain clipping and saturation are the dominant pulse formation mechanisms, we expect the generated bandwidth to decrease with increasing pump power (Sec. 2.2.1). In the limit where timing-mismatch and saturation are the dominant pulse formation mechanisms, we expect degenerate OPOs to achieve simulton operation for peaks where  $\Delta T_{\text{RT}}(\ell) > 0$ . In this limit, the generated bandwidth increases with increasing pump power (Sec. 2.2.2).

## 2.3 OPO Design and Experiment

Having established the key properties of OPOs, we now study these effects experimentally. We begin this section by discussing the design of the OPOs studied throughout the remainder of this chapter. Then, we characterize the OPO behavior in terms of threshold, conversion efficiency, and generated power spectral density. We will see that synchronization plays a key role in the OPO under study. The synchronous ( $\ell = 0$ ) peak exhibit behaviors that agree well with the box-pulse theory of Sec. 2.2.1. The asynchronous peaks exhibits qualitatively different spectral features and scaling laws, which agree well with the simulton theory of Sec. 2.2.2.

### 2.3.1 OPO Design

A schematic of the OPO used here is shown in Fig. 2.13. The OPO cavity consists of a bowtie resonator with a tunable round-trip delay around  $\sim 4$  ns. Cavity length adjustments are made by mounting the input coupler (M1) on a piezo stage (Newport NPM140). The cavity is pumped by  $\sim 70$  fs FWHM sech pulses at 250 MHz produced by 1045 nm modelocked Yb-fiber laser (Menlo Systems Orange A) with an average power of up to 950 mW. OPA occurs in a 1-mm-long Brewster-cut MgO-doped PPLN crystal placed at the focus between M2 and M3. The PPLN crystal has a poling period of  $31.8 \mu\text{m}$  to phase-match degenerate OPA of a signal at 2090 nm. The length is chosen heuristically to achieve a balance between threshold, efficiency, and bandwidth, with long crystals exhibiting lower threshold, less OPA bandwidth, and nonlinear loss due to saturation when  $\Delta k'L \gg \tau$ . A 1-mm-long PPLN crystal corresponds to a temporal walk-off of  $\Delta k'L = 100$  fs ( $\Delta k'L = 2.5\tau$ ), and a group delay dispersion (GDD) of  $k''L = -50 \text{ fs}^2$ .

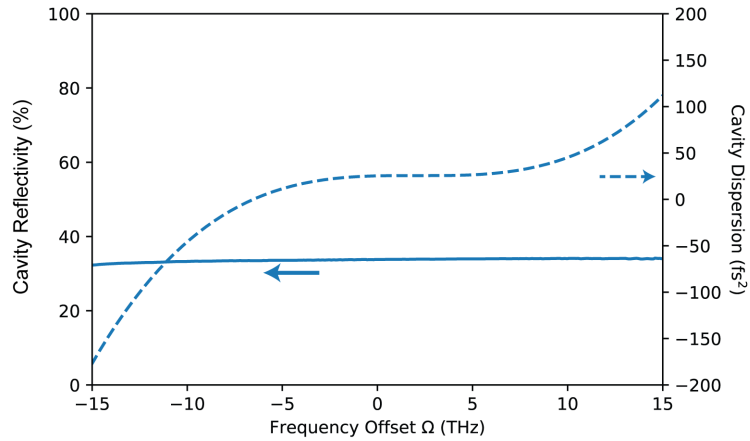


Figure 2.14: (Solid Line) The net reflection coefficient of the passive cavity optics and (Dotted Line) the associated group delay dispersion.

The cavity is designed to only resonate the signal, and comprises four mirrors (M1-M4). The input coupler is a dielectric mirror coated for high transmission ( $T > 96\%$ ) around the 1040 nm pump and high reflectivity ( $R > 99\%$ ) for signal wavelengths from 1758 nm to 2315 nm. Two concave gold mirrors (M2, M3) with  $R > 98\%$  and a radius of curvature of 38 mm focus the pump and signal to a  $1/e^2$  beam radius of  $10 \mu\text{m}$  and  $14 \mu\text{m}$  respectively. The output coupler (M4) is a dielectric mirror coated for broadband transmission ( $T = 65\%$ ) from 1400 nm to 2600 nm. Fig. 2.14(solid line) shows the net reflection coefficient of the dielectric mirrors, which is well described by a constant ( $R(\Omega) = 35\%$ ) from 1758 nm to 2315 nm. The net GDD of the dielectric mirrors is shown in Fig. 2.14 (dotted line), and the net phase deviation of the cavity is well approximated by  $\Delta\phi(\Omega) = -\sum_{m=2}^5 \frac{\phi_m}{m!} \Omega^m$ , where the  $\phi_m$  are given in Table 2.1. The mirror GDD of  $25 \text{ fs}^2$  half-compensates the GDD of the OPA. Given the low cavity finesse and high OPA gain, this

Table 2.1: Phase deviations due to higher order dispersion of the cavity mirrors

| $\phi_2$          | $\phi_3$          | $\phi_4$               | $\phi_5$               |
|-------------------|-------------------|------------------------|------------------------|
| $25 \text{ fs}^2$ | $76 \text{ fs}^3$ | $-13,000 \text{ fs}^4$ | $983,000 \text{ fs}^5$ |

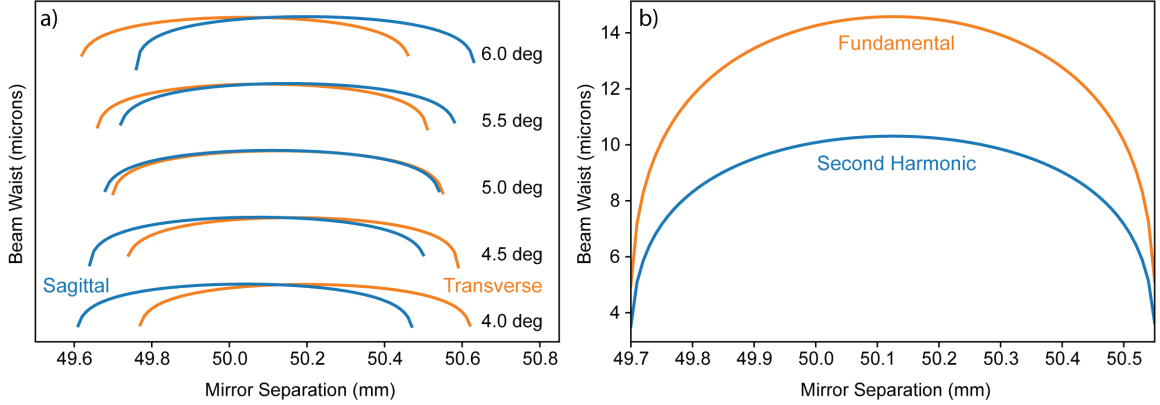


Figure 2.15: a) The  $1/e^2$  beam radius in the nonlinear crystal as a function of mirror separation and angle. Each angle is offset for clarity, and the cavity achieves a symmetric Gaussian beam for  $\theta = 5^\circ$ . Blue: sagittal, orange: transverse. b) The beam waist associated with the fundamental and second harmonic as a function of mirror separation for a  $5^\circ$  angle of incidence.

combination corresponds to noncritical operation where the OPO bandwidth given by Eqn. 2.14 is a weak function of the parametric gain.

We now consider the layout of the bowtie resonator. The cavity is subject to several constraints: i) the full optical path length of the cavity must correspond to a round-trip time of 4-ns to achieve synchronous pumping, ii) the separation of M2 and M3 is chosen to minimize the sensitivity of the signal waist with respect to mirror alignment, iii) the radius of curvature for M2 and M3 is chosen to achieve near-confocal focusing in the nonlinear crystal,  $L \sim 2z_R$ , and iv) the angle of incidence on the mirrors is chosen to compensate for astigmatism caused by the Brewster-cut PPLN crystal. The ABCD matrix for the cavity, with the reference point chosen in the middle of the nonlinear crystal, is given by

$$M = M_L(L_x/2)M_L(L_{\text{sep}}/2)M_R(R_{\text{eff}})M_L(L_F)M_R(R_{\text{eff}})M_L(L_{\text{sep}}/2)M_L(L_x/2), \quad (2.39)$$

where the propagation and reflection matrices, respectively, are given by

$$M_L(L) = \begin{bmatrix} 1 & L \\ 0 & 1 \end{bmatrix} \quad M_R(R) = \begin{bmatrix} 1 & 0 \\ -2/R & 1 \end{bmatrix}. \quad (2.40)$$

Each of the parameters input to the matrices varies depending on whether we consider the sagittal

or transverse plane, due to astigmatisms. For the transverse plane, a Brewster-cut crystal has an effective length given by  $L_{x,t} = L\sqrt{n^2 + 1}/n^2$ , whereas the effective length is  $L_{x,s} = L\sqrt{n^2 + 1}/n^4$  for the sagittal plane. Similarly, when considering reflections from a curved mirror, the effective radius of curvature is given by  $R_{\text{eff},t} = R\cos(\theta)$  in the transverse plane, and  $R_{\text{eff},s} = R\sec(\theta)$  in the sagittal plane.  $L_{\text{sep}}$  is the separation between the curved mirrors, and the length of the feedback section needed to achieve synchronous pumping is given by  $L_F = c/f_R - L_{\text{sep}} - L_{x,t}$ .

The beam waist ( $1/e^2$  radius) in the transverse and sagittal plane is plotted as a function of mirror separation and mirror angle for OPO under study here (Fig. 2.15(a)). Each angle is offset for clarity. For an angle of  $5^\circ$  the intracavity astigmatisms cancel, resulting in a symmetric Gaussian beam. Fig. 2.15(b) shows the beam waist of the fundamental and second harmonic as a function of mirror separation for a  $5^\circ$  angle of incidence. For a separation of 50.1 mm, the beam waists associated with the fundamental and second harmonic achieve local maxima of  $14.6\text{-}\mu\text{m}$  and  $10.3\text{-}\mu\text{m}$ , respectively. We operate the cavity near these parameters to reduce the sensitivity of the cavity modes to small misalignments of the mirrors.

In an experimental setting we choose to operate the OPO in one of two modes; swept and locked. Swept operation corresponds to the case where one of the mirrors of the OPO is continuously swept over a wide range of cavity lengths. For an NPM140 piezo stage, we use a 10-Hz 150-V peak-to-peak triangle wave to linearly sweep the length of the cavity  $\pm 70\text{ }\mu\text{m}$ . This mode is useful for finding the cavity length that achieves perfect synchronization, tuning of the alignment of the cavity, and measuring the relative conversion efficiency of each of the OPO resonances. Locked operation corresponds to the case where the cavity length is actively locked on a resonance using a dither-and-lock scheme, where a small ( $\sim 1\text{ mV}$  peak-to-peak) sine-wave is used to dither one of the piezo stages at frequency  $\omega_{\text{mod}}$ . This produces a small amplitude modulation of the output power,  $P_{\text{out}}$ , proportional to  $\partial_\ell P_{\text{out}} \cos(\omega_{\text{mod}}t)$ . We detect the amplitude of this modulation,  $\partial_\ell P_{\text{out}}$ , using lock-in detection. The output of the lock-in amplifier is then phase-flipped and fed back onto one of the piezo stages of the cavity, which locks the cavity length such that the output power is at a local maximum,  $\partial_\ell P_{\text{out}} = 0$ . In short, dither locking corresponds to feedback control of  $\partial_\ell P_{\text{out}}$  with a PI-controller, where the open-loop gain and open-loop pole are determined by the sensitivity and time constant of the lock-in amplifier. Once the OPO cavity length is locked, this mode of operation is used to characterize the beam quality, the conversion efficiency, and both the power spectral density and the coherence properties associated with the pulses generated by the OPO.

### 2.3.2 Experimental Results

We now study the behavior of an OPO as the timing mismatch is varied around perfect synchronization with the pump by sweeping the length of the feedback section of the cavity. The OPO is only resonant for the signal and oscillates around cavity lengths where the signal acquires a phase shift of  $0$  or  $\pi$  relative to the pump on each round trip, leading to a discrete set of resonances whose

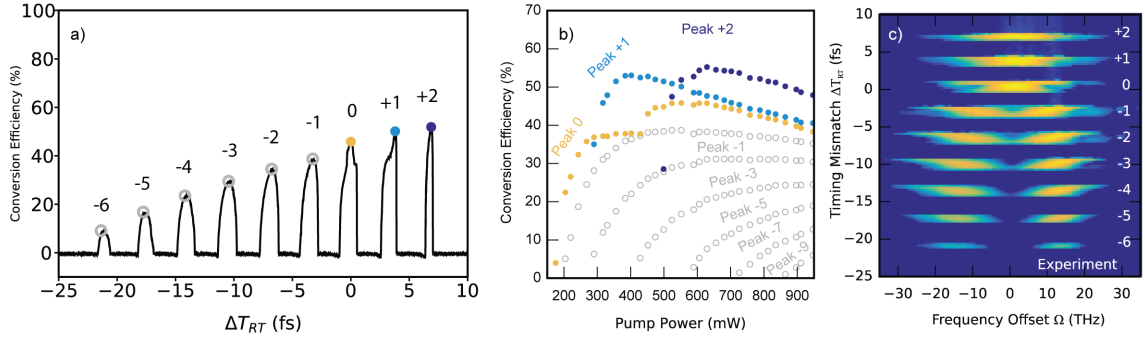


Figure 2.16: a) The conversion efficiency as a function of cavity length detuning for 550 mW of pump power. Each peak is labeled with  $\ell$  relative to the peak with lowest threshold. b) The conversion efficiency of each peak as a function of pump power. Peaks with  $\ell = 1$  and  $\ell = 2$  exhibit larger slope efficiencies and overall conversion efficiencies than the synchronous resonance. c) The power spectral density as a function of cavity length detuning. The synchronous resonance exhibits box-pulse behavior and transitions from degenerate to non-degenerate operation as the cavity is detuned through  $\ell = 0$ . Resonances with  $\ell > 0$  only exhibit degenerate operation.

behavior depends strongly on the timing mismatch.

The conversion efficiency is shown as a function of cavity length detuning in Fig. 2.16(a), with each peak labeled by the corresponding  $\ell$ . We assume  $\ell = 0$  corresponds to the lowest threshold resonance observed in the cavity, and use this as a reference point. We determine which peaks correspond to  $\ell < 0$  by comparing the piezo voltages of these peaks against  $\ell = 0$ , with voltages that result in a shorter cavity corresponding with increasingly negative  $\ell$ . Fig. 2.16(b) shows the conversion efficiency as a function of pump power for each resonance. The synchronous resonance ( $\ell = 0$ ) exhibits the lowest threshold, 175 mW, a slope efficiency of 158%, and a peak conversion efficiency of 46%. The “short cavity” resonances, where  $\ell < 0$ , are shown in grey with thresholds increasing monotonically with increasing  $|\ell|$ . Each of the short cavity resonances have similar slope efficiencies ( $\sim 40\%$ ), and achieve lower net conversion efficiencies than the synchronous resonance. The “long cavity” resonances, where  $\ell > 0$ , are shown in blue, and exhibit irregularly spaced thresholds as  $\Delta T_{RT}$  becomes increasingly positive. These resonances have measured slope efficiencies as high as 570%, with peak efficiencies of 55%. This asymmetry, in terms of threshold, slope efficiency, and peak efficiency, suggests that opposite signs of  $\ell$  correspond to distinct operating regimes, and confirms that the behavior of the OPO is extremely sensitive to the timing mismatch.

To better characterize these operating regimes in terms of the pulse formation mechanisms studied in Sec. 2.2, we consider the power spectral density output from the OPO as a function of cavity length detuning in Fig. 2.16(c). The synchronous peak exhibits behavior qualitatively similar to that predicted by the box pulse theory considered in Sec. 2.2.1. Half of the resonance ( $\ell < 0$ ) exhibits degenerate operation, with the spectrum peaked around  $\Omega = 0$ . This resonance transitions to non-degenerate operation, with a multi-peaked spectrum, for  $\ell > 0$ . The transition from degenerate

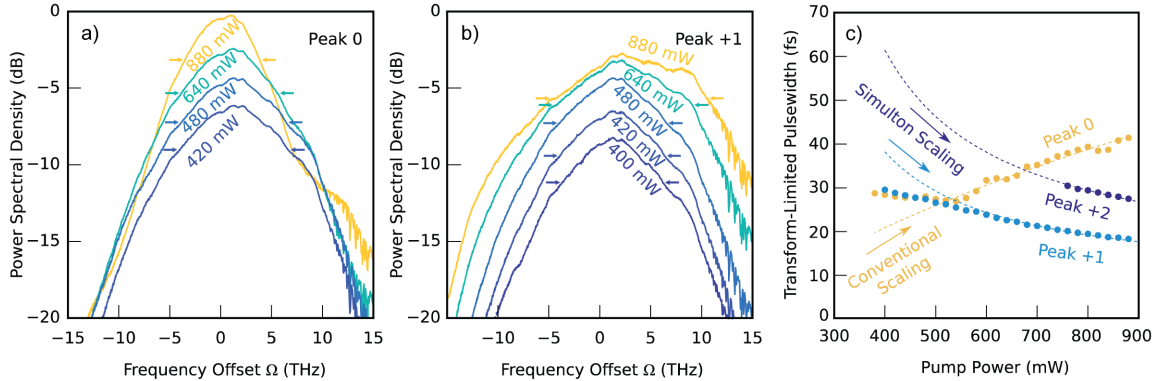


Figure 2.17: Power spectra recorded as a function of pump power for a) peak 0 and b) peak +1. Each curve is labeled with the corresponding pump power used in the experiment, with arrows denoting the 3dB bandwidth. c) The scaling with pump power of the transform limited pulsewidth (3 dB) for peaks 0-2, computed from spectra such as those shown in a-b. For large powers, peak 0 shows an increase in pulsewidth in accordance with Eqn. 2.28, while peaks +1 and +2 show a monotonic decrease in pulsewidth, in accordance with Eqn. 2.38.

to non-degenerate operation is not observed within the other resonances. Instead, short cavity resonances only exhibit non-degenerate operation, and long cavity resonances only exhibit degenerate operation.

We may further characterize these operating regimes by considering how the bandwidth output from the OPO scales with increasing pump power. The synchronous peak exhibits a spectrum that loses bandwidth with increasing power (Fig. 2.17(a,c)), in accordance with box-pulse scaling. The long cavity resonances, labeled Peak +1 and +2 in Fig. 2(a), exhibit  $\text{sech}^2$  spectra which monotonically increase in bandwidth as the pump power is increased (Fig. 2(b,d)) in accordance with the simulton scaling, Eqn. (2.38). The spectra deviate from the exponential tails of a  $\text{sech}^2$  spectrum beyond  $\pm 10$  THz due to atmospheric absorption around 1850 nm. Peak +1 achieves a 3dB bandwidth as high as 240 nm, which can support pulses as short as 19 fs. When the cavity is negatively detuned ( $\Delta T_{\text{RT}} < 0$ ) the OPO transitions to non-degenerate operation and the spectra split into a distinguishable signal and idler (Fig. 2(e)). We therefore identify three regimes of operation associated with the timing mismatch: synchronous ( $\Delta T_{\text{RT}} = 0$ ), non-degenerate ( $\Delta T_{\text{RT}} < 0$ ), and simulton ( $\Delta T_{\text{RT}} > 0$ ). We note here that while none of the models introduced in Sec. 2.2 are well suited for describing the nondegenerate resonances observed for  $\ell < 0$ , we may gain some insight from the simulton theory. Simulton formation, which is consistent with the behavior of the OPO for  $\ell > 0$ , suggests that the dominant pulse formation mechanisms for  $|\ell| \geq 1$  are gain saturation and timing mismatch. For  $\ell < 0$  these mechanisms cannot balance each other and no self-consistent half-harmonic pulse can form in the cavity. This suggests that resonances with  $\ell < 0$  are purely nondegenerate, as observed here.

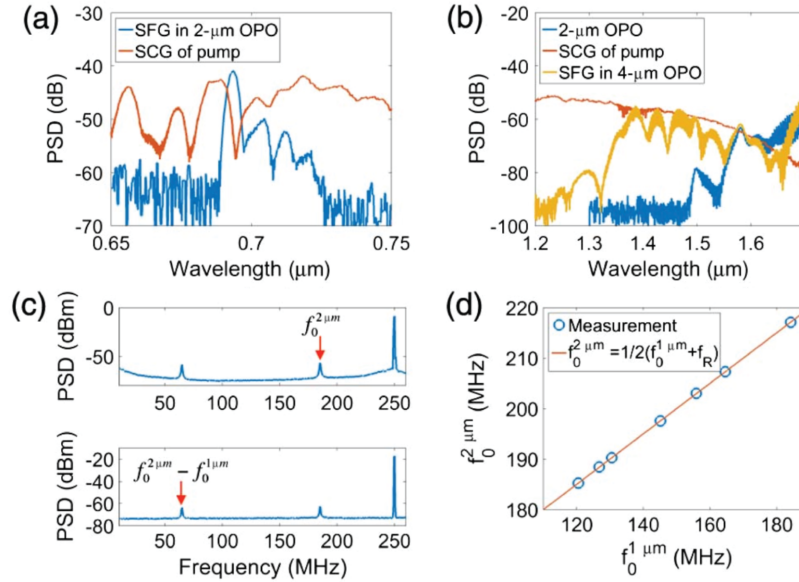


Figure 2.18: Carrier-envelope-offset detection of the pump comb and OPO. a,b) The overlap of the pump SCG with the parasitic SFG at 700 nm and with the OPO spectrum around 1600-nm, respectively. c) The resulting  $f_{\text{ceo}}$  beatnotes,  $f_0^{2\mu\text{m}}$  and  $f_0^{2\mu\text{m}} - f_0^{1\mu\text{m}}$ . d)  $f_0^{2\mu\text{m}}$  as a function of  $f_0^{1\mu\text{m}}$ , showing that a degenerate OPO achieves intrinsic frequency locking. Adapted from [27].

Having experimentally characterized the regimes of operation present in the OPO, we now study the coherence properties of a degenerate ( $\ell > 0$ ) resonance by measuring  $f_{\text{ceo}}$ . We extend the spectrum of the  $1\ \mu\text{m}$  pump laser by performing supercontinuum generation in a tapered photonic crystal fiber and measure the  $f_{\text{ceo}}$  of both the pump and the OPO using two heterodyne measurements. First, we interfere the pump supercontinuum with the parasitic SFG of the  $2\text{-}\mu\text{m}$  OPO with the  $1\text{-}\mu\text{m}$  pump, which produces a signal around 700 nm (Fig. 2.18(a)). The parasitic SFG has an  $f_{\text{ceo}} = f_0^{2\mu\text{m}} + f_0^{1\mu\text{m}}$ , and therefore interferes with the pump supercontinuum to produce a beatnote at  $f_0^{2\mu\text{m}}$ . Second, we interfere the pump supercontinuum with the tail of the OPO around 1600 nm (Fig. 2.18(b)). The interference of the OPO with the pump supercontinuum produces beatnotes at  $f_0^{2\mu\text{m}} - f_0^{1\mu\text{m}}$  (Fig 2.18(c)). Then, using these two measurements, we may plot  $f_0^{2\mu\text{m}}$  as a function of  $f_0^{1\mu\text{m}}$  as we vary the current used to drive the diode lasers pumping the modelocked laser. The result is shown in Fig 2.18(d), which confirms that the OPO comb is frequency-locked to the pump with  $f_0^{2\mu\text{m}} = (f_0^{1\mu\text{m}} + f_R)/2$ .

The results shown here confirm that the operating regimes of the OPO are consistent with the theoretical models introduced in Sec. 2.2, and that the degenerate resonances are intrinsically phase-locked to the pump laser as discussed in Sec. 2.1.2. Furthermore, we have shown that asynchronization is a resource that can improve the performance of an OPO. Resonances with  $\ell > 0$  operate in the simulton regime where they achieve larger conversion efficiencies than degenerate

resonances, and exhibit large bandwidths that increase with increasing times above threshold.

## 2.4 Numerical Simulations

The previous sections established the steady-state operating regimes present in an OPO both in theory and experiment. In this section, we study the dynamics associated with the three regimes of operation observed in the experiment using numerical methods. This allows us to understand how the OPO evolves from semi-classical vacuum noise to steady state, and better understand the pulses that form in steady state without making assumptions about the dominant pulse formation mechanisms.

The OPO is modeled as an OPA followed by a linear feedback loop. On each round trip, we solve the full coupled wave equations using the split-step Fourier methods described in Ch. 1, including dispersion to arbitrary order using the full Sellmeier form given in [65]. We model the feedback loop as a linear filter for the signal:

$$A_{\omega}^{(n+1)}(0, t) = \mathcal{F}^{-1}\{\sqrt{R(\Omega)}e^{-i\phi(\Omega)}\mathcal{F}\{A_{\omega}^{(n)}(L, t)\}\},$$

where  $A_{\omega}$  is the envelope of the signal pulse,  $1 - R$  is the round-trip power loss for the cavity, and the phase  $\phi(\Omega)$  is measured relative to a half-harmonic signal perfectly synchronous with the pump

$$\phi(\Omega) = -\phi_0 - \pi\ell - \Delta T_{\text{RT}}(\ell)\Omega - \Delta\phi(\Omega).$$

$\phi_0$  represents an offset between the cavity resonances and the cavity length that synchronizes the pump and signal,  $\Delta\phi(\Omega)$  represents the quadratic and higher order dispersion of the cavity mirrors,  $\ell$  is the resonance number, and the timing mismatch is  $\Delta T_{\text{RT}}(\ell) = 2\pi\ell/\omega_p$ .

The solid lines in Fig. 2.19(a) show the simulated conversion efficiency of the resonances in the synchronous and simulton regimes, and are shown to be in good agreement with the experimental thresholds and slope efficiencies. Deviations that occur at higher powers are likely due to radial variations in pump depletion, which are not included in our heuristic model of gain-induced diffraction discussed in Sec. A.1. Figs 2.19(b-c) compare the experimental and simulated power spectral density as a function of timing mismatch with parameters corresponding to the experiment. The three regimes of operation indicated by the dashed boxes. The simulations show excellent agreement with the experimental data in all three operating regimes.

Having shown agreement between the numerical model and experiment, we now use the model to better understand the femtosecond pulse formation dynamics in the OPO. In general, observing the buildup of a femtosecond pulse from noise is experimentally challenging, and these simulations provide a powerful tool for understanding how the pulses formed in an OPO achieve stable operation. The evolution of the signal pulse is shown in Fig. 2.20(a-c) for each of the three regimes

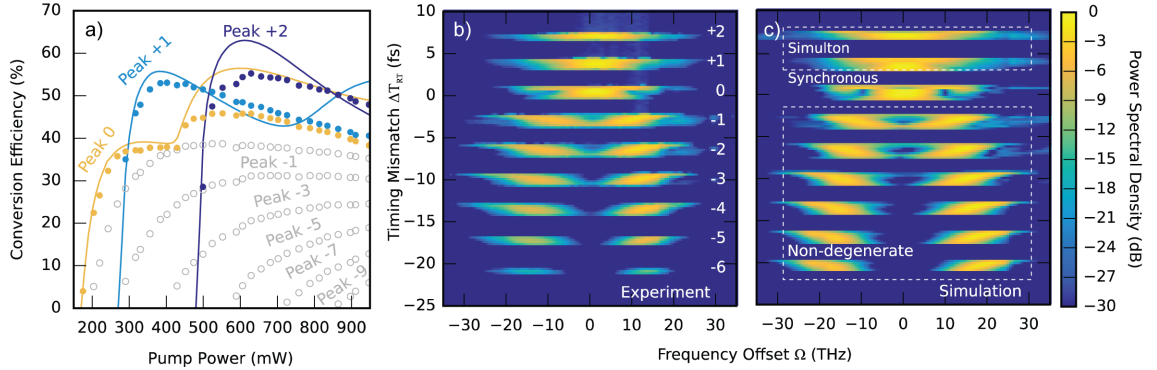


Figure 2.19: Comparison of simulation results to experiment. a) Simulated conversion efficiency (solid color lines) compared to experimental data (filled circles). Grey circles denote non-degenerate operation. b) Experimental and c) simulated power spectral density as a function of cavity length detuning.

of operation. Each round trip is recorded at the output of the OPA and normalized to its peak amplitude to visualize the pulse motion. The dotted white lines show the expected trajectory of a linearly propagating half-harmonic signal pulse, which acquires a delay  $\Delta T_{RT}$  on every round trip. In these figures, the time coordinates have been shifted such that a signal peaked at  $t = 0$  corresponds to a pulse walking symmetrically from the tail of the pump at  $\Delta k' L/2$  to the leading edge of the pump  $-\Delta k' L/2$ . For a negatively detuned peak (Fig. 2.20(a)), the pulse envelope shows a 10 THz modulation in time (vertical fringes), resulting from interference of a signal and idler split from degeneracy by  $\pm 10$  THz. The interference fringes are seen to shift on each round trip, corresponding to a  $\pm 10$  MHz offset of the signal and idler carrier-envelope-offset frequency  $f_{ceo}$  from that of a half-harmonic signal (horizontal fringes). When the cavity length is tuned into synchronization (Fig. 2.20(b)), the signal builds up without any motion relative to the pump until the pump saturates, shifting the signal forward in time until a new steady state is found on the leading edge of the pump. The evolution for a positively detuned cavity is shown in Fig. 2.20(c). The signal initially tracks the trajectory of a linearly propagating pulse, shifting towards the tail of the pump. Once the signal is intense enough to deplete the pump, it accelerates, becoming faster than would be possible under linear propagation, and thereby reaches a steady state, synchronous with the pump repetition rate.

The behavior exhibited by the long cavity resonances, namely a nonlinear acceleration of the signal pulses, again confirms that the OPO dynamics in this regime correspond to simulton formation. Furthermore, the full numerical model facilitates an intuitive picture of the behavior of the simulton peaks. The large thresholds and slope efficiencies of the simulton peaks are due to the short pulse duration of the pump. When  $a \ll a_{sim}$  the signal pulse will accumulate many successive group delays due to the timing mismatch, and experience a decrease in gain due to a reduction in the temporal overlap with the pump as determined by the gain clipping function,  $\Gamma(L, t)$ . Since simulton

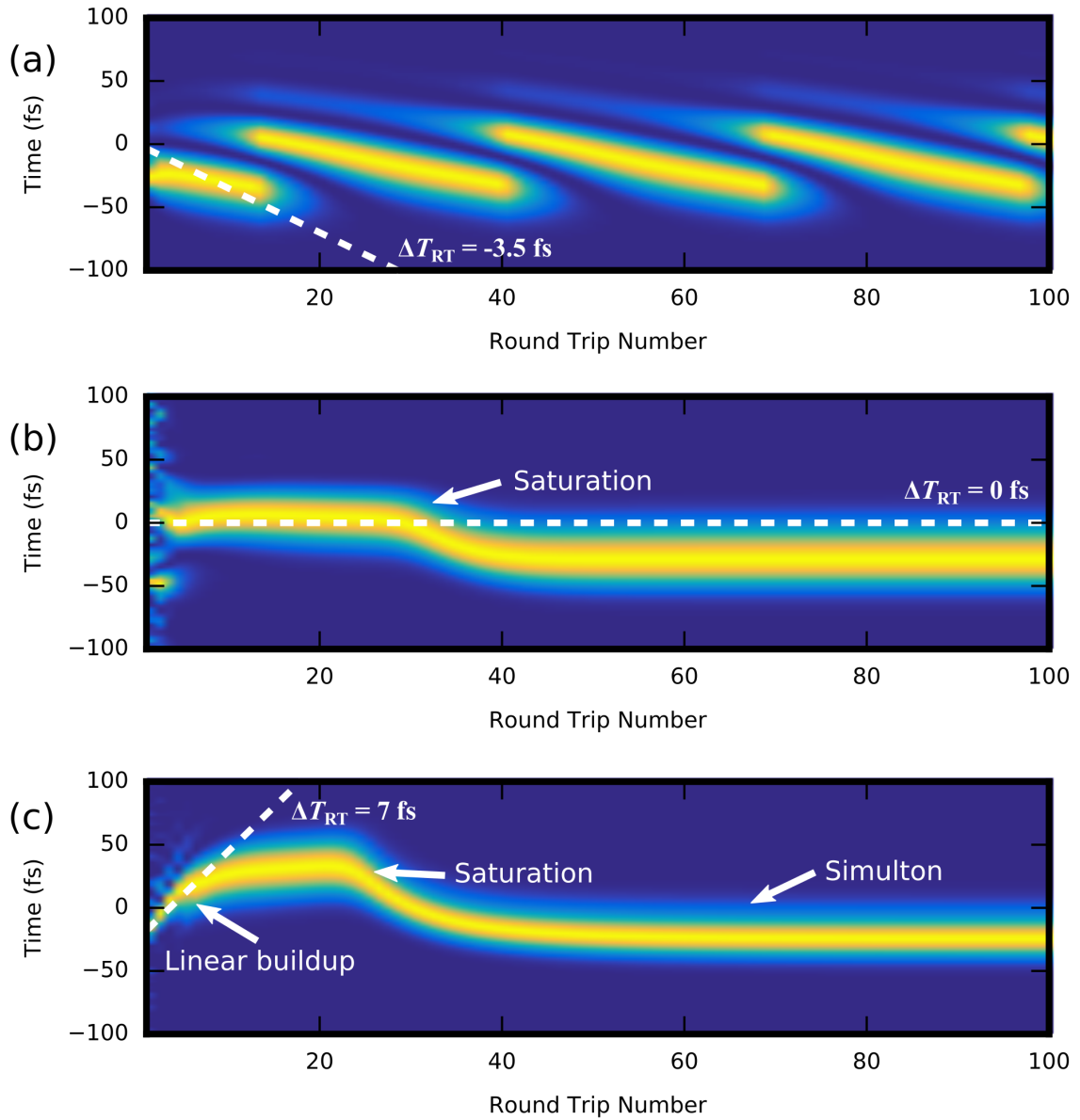


Figure 2.20: (a) Simulated evolution of the intracavity pulse intensity over many round trips for  $\Delta T_{RT} = -3.5$  fs showing the interference of a distinct signal and idler. The dotted line denotes the trajectory of a linearly propagating half-harmonic signal pulse. (b) Pulse evolution for  $\Delta T_{RT} = 0$  fs showing the formation of a half-harmonic pulse synchronized to the pump repetition rate. (c) Simulated pulse evolution for  $\Delta T_{RT} = 7$  fs showing the formation of a half-harmonic pulse which, upon depleting the pump, is able to accelerate forward in time and synchronize to the pump repetition rate.

operation requires the signal to be bright enough to deplete the pump, threshold then corresponds to the condition that the signal builds up from quantum noise to the simulton energy before the total accumulated time delay reduces the gain seen by the signal pulse below the cavity loss. Once this condition is satisfied, the signal accelerates back into the pump and depletes it, leading to large slope efficiencies observed in experiment.

## 2.5 The Bandwidth and Stability Limits of OPOs

The observed monotonic increase in bandwidth associated with simulton formation cannot be sustained for arbitrarily large times above threshold. There is an upper bound to the possible generated bandwidth, but to date this has not been characterized in an experiment, nor accounted for with corrections to the theory presented in Sec. 2.2.2. Furthermore, it can be shown that third order dispersion (TOD) plays a critical role in the stability of simultons, with moderate positive TOD necessary for stable simulton operation. These two topics are interconnected, and are the subject of ongoing research. We briefly summarize the attempts made to understand these effects here.

We begin by discussing the role of third order dispersion. Using the numerical methods discussed in Sec. 2.4, it can be shown that a small positive TOD is necessary for stable simulton operation. Simply truncating the dispersion operator to second order, we find that the OPO no longer achieves degenerate operation when  $\ell > 0$ . Furthermore, we can add an element to the cavity that contributes an adjustable amount of third order dispersion,  $\phi'''$ , and find that for a small positive TOD ( $\phi''' \sim 1000 \text{ fs}^3$ ) stable simulton operation occurs. We may incorporate this effect into the simulton ansatz using the time-domain equations of motion including TOD,

$$\partial_z A_\omega(z, t) = \kappa A_{2\omega} A_\omega^* + \frac{k_\omega'''}{6} \partial_t^3 A_\omega, \quad (2.41a)$$

$$\partial_z A_{2\omega}(z, t) = -\Delta k' \partial_t A_{2\omega} - \kappa A_\omega^2, \quad (2.41b)$$

and using the manifold projections discussed in Sec. 2.2.2. We find that the odd dispersion orders contribute to a shift in the centroid of the simulton and Eqn. 2.37b becomes

$$\Delta T = \Delta T_{RT} - \tau(\gamma_0 L + \ln(r)) + \frac{\phi'''}{10\tau^2}. \quad (2.42)$$

It is convenient to normalize time to the unperturbed simulton pulse duration,  $\tau_s = \Delta T_{RT}/(\gamma_0 L + \ln(r))$ , such that Eqn. 2.42 becomes

$$\Delta \bar{T} = \Delta \bar{T}_{RT} - \Delta \bar{T}_{RT} \bar{\tau} + \frac{\bar{\phi}'''}{10\bar{\tau}^2}.$$

In steady state ( $\Delta\bar{T} = 0$ ), we find a cubic equation for  $\bar{\tau}$ ,

$$\bar{\tau} = 1 + \frac{\bar{\phi}'''}{10\bar{\tau}^2\Delta\bar{T}_{\text{RT}}}.$$

Assuming a small perturbation  $\bar{\tau} = 1 + \delta\tau$ , we may estimate the change in pulse duration to first order in  $\delta\tau$ ,

$$\delta\tau = \frac{\bar{\phi}'''}{10(\gamma_0 L + \ln(r))}.$$

As an example, when the OPO is four times above threshold we have,

$$\delta\tau = \frac{\bar{\phi}'''}{10\ln(\frac{1}{r})}$$

Low finesse cavities tolerate more dispersion. For a cavity with  $R=0.35$  the third order dispersion stretches a 20-fs-long pulse by 2.4% when  $\phi''' = 1000 \text{ fs}^3$ .

While the third order dispersion necessary to achieve stable simultons slows the scaling of bandwidth with respect to pump power for pulses approaching a single cycle, Eqn. 2.42 still exhibits a monotonic increase in bandwidth with increasing pump power. In contrast, in the limit of large times above threshold the gain-clipping function spans a sufficiently large window in time that the timing mismatch should become negligible. In this case, the box-pulse theory should be sufficient to describe the behavior of the OPO. This argument suggests that there is a transition from simulton operation to box-pulses when the OPO is driven far above threshold, which should correspond to a local maximum in the bandwidth generated by the OPO. This transition has not yet been observed in experiment, and the theoretical tools to predict this transition point, and therefore the maximum obtainable bandwidth from an OPO, have not yet been developed. Possible approaches that may address both the role of third order dispersion in determining the stability of simultons and the transition from simulton operation to box-pulses include Legrangian methods[66] and the method of multiple moments[67]. Both of these analytic tools have been successfully used to treat the evolution and stability of solitons in nonlinear resonators.

## 2.6 Outlook and Future Work

The work discussed throughout this chapter shows that synchronously pumped OPOs are promising sources of broadband optical frequency combs in the mid-infrared. In particular, when an OPO is operated in the simulton regime it can achieve a total conversion efficiency  $> 60\%$ , and generate few-cycle pulses with a large optical bandwidth that increases with increasing pump power. Furthermore, the simulton regime exhibits the intrinsic phase-locking associate with degenerate operation. Therefore, when a simulton OPO is pumped by an optical frequency comb the light generated by the OPO is a stable mid-infrared frequency comb, without the need for additional f-2f interferometry.

We closed this chapter by discussing the bandwidth limits and stability requirements of simltons. There are still a number of unanswered questions regarding simltons, namely, why TOD is necessary to ensure stable operation and what the ultimate bandwidth limits of simlton OPOs are. New analytical tools to address these questions will be the subject of future work. Furthermore, we remark that there are still experimentally relevant operating regimes in OPOs that have not yet been explored analytically[68]. The extension of the techniques described here to these operating regimes may yield entirely new design rules for broadband OPO operation.

## Chapter 3

# Nonlinear Nanophotonic Devices

### Introduction

In this chapter we discuss next generation devices based on quasi-phasematched interactions in nonlinear nanophotonic waveguides. Until recently, the state-of-the-art photonics platforms for quasi-phasematched nonlinear devices were based on weakly-guiding diffused waveguides in periodically-poled ferroelectrics like lithium niobate[69], lithium tantalate[70], and potassium titanyl phosphate[71]. These waveguides are formed by a small refractive index modulation ( $\Delta n \sim 0.02$ ) due to in-diffused dopants and exhibit low-loss ( $\sim 0.1$  dB/cm) modes with field-diameters of  $\sim 5 \mu\text{m}$ , and quasi-phasematched interactions between these modes through periodic poling to pattern the  $\chi^{(2)}$  coefficient. To date, these devices have suffered largely from two limitations. The power requirements of such devices are set by the largest achievable normalized efficiencies (90%/W-cm<sup>2</sup> for SHG of 1560-nm light[72]), and the phase-matching bandwidths (and hence useful lengths for pulsed interactions) have ultimately been limited by the material dispersion that dominates over geometrical dispersion in weakly-guiding waveguides.

Recent efforts have focused on the development of  $\chi^{(2)}$  nanophotonics in platforms such as lithium niobate[73], aluminum nitride[74, 75] and gallium arsenide[76]. These systems allow for densely integrated nonlinear photonic devices, and achieve efficient frequency conversion due to the large field intensities associated with sub-wavelength mode confinement. This chapter focuses on our work developing nanophotonic PPLN devices, which exhibit low loss, large nonlinearities, and the potential for dispersion-engineered nonlinear interactions. This latter feature is unique to nanophotonic PPLN, and enables both the study of new dynamical regimes and extremely nonlinear interactions that occur when short pulses propagate over long lengths.

This chapter proceeds in seven sections. In Sec. 3.1, we briefly summarize the relevant aspects of optical waveguide theory, namely, the dispersion associated with waveguide modes, the nonlinear coupling between two waveguide modes, and the associated coupled wave equations. A more detailed

treatment of this material can be found in Appendix B. In Sec. 3.2, we discuss the fabrication of nanophotonic PPLN devices, and present an experimental characterization of CW SHG in this platform. These results confirm that this platform can achieve performance close to theoretical predictions, with power requirements 50x lower than diffused waveguides, and lays the groundwork for the experiments that follow. The second half of this chapter focuses on nonlinear interactions of short pulses in dispersion-engineered nanophotonic PPLN waveguides. Sec. 3.3 considers pulsed SHG in a dispersion-engineered ridge waveguide. We will show that a suitable choice of waveguide geometry facilitates at least an order of magnitude increase of the interaction length for pulsed interactions, thereby reducing the energy requirements of these devices by another two orders of magnitude. These devices achieve saturated SHG with 10's of fJ of pulse energy, where energy requirements of 10's - 100's of pJ were common with previous-generation diffused waveguides. Sec. 3.4 considers phase-mismatched SHG in the same structures studied in Sec. 3.3. In the limit of an undepleted fundamental, we are able to show that cascaded nonlinearities can achieve an effective nonlinear refractive index,  $n_2$ , that exceeds the  $n_2$  associated with  $\chi^{(3)}$  nonlinearities in state-of-the-art nanophotonic waveguides. Motivated by these results, in Sec. 3.5 we study the formation of a coherent supercontinuum spanning the full transparency window of our collection optics (400 - 2400 nm) using only 10-pJ of pulse energy. While this observed behavior can be interpreted with some success using conventional heuristics based on cascaded nonlinearities, we can gain more insight using a model based on saturated SHG. This model is presented in Sec. 3.6, and explains both the observed spectrum and its coherence properties. Finally, in Sec. 3.7, we summarize these results and discuss future work.

### 3.1 The Coupled Wave Equations in Nonlinear Waveguides

We begin by reviewing the relevant aspects of optical waveguide theory for the nonlinear devices considered throughout this chapter. This section begins with the definition of waveguide modes, as well as their orthogonality relations and dispersion relations[77]. We then establish a convenient mode normalization to derive the nonlinear coupling between two waveguide modes. This inter-modal coupling, when combined with the dispersion operators, yields the coupled wave equations for ultra-short pulses in nonlinear waveguides.

Typical nonlinear waveguides considered here comprise an LN ridge, an air top cladding, and a silica substrate as shown in Fig. 3.1 with the associated field distribution of the  $TE_{00}$  mode,  $E_{x,\mu}$ . We note for completeness that many other cross sections are possible, including multi-layer claddings and W-shaped ridges, but that the simple geometry shown here already allows for engineering of a wide variety of new devices. Waveguide modes arise as the solution to Maxwell's equations in the absence of a nonlinear polarization, with a dielectric constant  $\bar{\epsilon}(x, y, \omega)$  that varies in two spatial dimensions. Since  $\bar{\epsilon}(x, y, \omega)$  is translationally invariant in  $z$ , we may solve Maxwell's equations by



Figure 3.1: Schematic of typical ridge waveguide, with the associated electric field  $E_{x,\mu}$  of the waveguide mode for both the fundamental (left) and second harmonic (right). The top cladding is air, the etched thin film is X-cut MgO:LN, and we approximate the 2- $\mu\text{m}$ -thick silica adhesion layer as extending to infinity.

expanding the fields in a series of guided modes

$$\mathbf{E}(x, y, z, \omega) = \sum_{\mu} a_{\mu}(\omega) \mathbf{E}_{\mu}(x, y, \omega) e^{-ik_{\mu}(\omega)z}, \quad (3.1a)$$

$$\mathbf{H}(x, y, z, \omega) = \sum_{\mu} a_{\mu}(\omega) \mathbf{H}_{\mu}(x, y, \omega) e^{-ik_{\mu}(\omega)z}, \quad (3.1b)$$

where  $a_{\mu}$  represents the component of  $\mathbf{E}$  contained in mode  $\mu$  around frequency  $\omega$ . The transverse mode profiles,  $\mathbf{E}_{\mu}$  and  $\mathbf{H}_{\mu}$ , and their associated propagation constant,  $k_{\mu}$ , arise as solutions to an eigenvalue problem. The dispersion operator,  $\hat{D}$ , that describes the propagation of a short pulse in mode  $\mu$  can be found using  $\hat{D}(t) = \sum_{m=2}^{\infty} (-i)^{(m+1)} (k_{\mu}^{(m)} \partial_t^m) / m!$  by evaluating derivatives of  $k_{\mu}$  with respect to  $\omega$ . This chapter will focus predominantly on  $\text{TE}_{00}$  modes in X-cut films, which exhibit both large nonlinearities and allow for dispersion engineering at many wavelengths of interest. All of the eigenmodes satisfy an orthogonality relation,

$$\int_A \frac{1}{2} \text{Re}([\mathbf{E}_{\mu} \times \mathbf{H}_{\nu}^*] \cdot \hat{z}) dx dy = \int_A \frac{1}{2} \text{Re}([\mathbf{E}_{\nu}^* \times \mathbf{H}_{\mu}] \cdot \hat{z}) dx dy = P \delta_{\mu,\nu}, \quad (3.2)$$

where the fields are normalized such that  $P = 1$  W, and therefore the power contained in mode  $\mu$  is  $P|a_{\mu}|^2$ . For deriving the nonlinear coupling between two modes, it's convenient to express these mode profiles using dimensionless functions  $\mathbf{e}(x, y)$  and  $\mathbf{h}(x, y)$

$$\mathbf{E}_{\mu}(x, y) = \sqrt{\frac{2Z_0 P}{n_{\mu} A_{\text{mode},\mu}}} \mathbf{e}_{\mu}(x, y), \quad (3.3a)$$

$$\mathbf{H}_{\mu}(x, y) = \sqrt{\frac{2n_{\mu} P}{Z_0 A_{\text{mode},\mu}}} \mathbf{h}_{\mu}(x, y), \quad (3.3b)$$

where  $n_{\mu}$  is the effective index of mode  $\mu$ , and  $Z_0$  is the impedance of free space.  $\mathbf{e}(x, y)$  and  $\mathbf{h}(x, y)$  are normalized such that the peak value of  $\text{Re}(\mathbf{e}_{\mu} \times \mathbf{h}_{\mu}^*) \cdot \hat{z}$  is unity. As a consequence of Eqn. (3.2), the area of mode  $\mu$  is given by  $A_{\text{mode},\mu} = \int \text{Re}(\mathbf{e}_{\mu} \times \mathbf{h}_{\mu}^*) \cdot \hat{z} dx dy$ . The modal area is a measure of

how tightly confined a mode is and largely determines the strength of nonlinear interactions, with more tightly confined modes producing stronger nonlinear couplings.

Having established the waveguide modes and their normalization, we now discuss the nonlinear coupling between two waveguide modes and define the effective area,  $A_{\text{eff}}$ , associated with these interactions. The effective area provides a measure of the strength of a nonlinear interaction due to the tight confinement of the waveguide; small effective areas correspond to large field intensities and large normalized efficiencies. We focus on the case of SHG in a nonlinear waveguide, but the results presented here are readily generalized to three wave interactions. The treatment used here accounts for the fully-vectorial nature of the modes[78, 79], with each field component of the waveguide mode coupled together by the full nonlinear tensor,  $d_{ijk}$ , of the media that comprise the waveguide. Remarkably, these equations have the same form as the coupled wave equations for SHG in much simpler contexts, such as SHG of plane waves and, in the limit of no pump depletion, paraxial gaussian beams.

The presence of a nonlinear polarization at frequency  $\omega$  gives rise to driving terms that cause the content of each mode,  $a_\mu$ , to evolve in  $z$ . It can be shown (Appendix B) that  $a_\mu$  evolves as

$$\partial_z a_\mu(z, \omega) = \frac{-i\omega}{4P} e^{ik_\mu z} \int \mathbf{E}_\mu^* \cdot \mathbf{P}_{\text{NL},\omega} dx dy. \quad (3.4)$$

For second-harmonic generation in the limit where one pair of modes is close to phasematching, we consider use one mode of the fundamental at frequency  $\omega$  and one mode of the second harmonic at frequency  $2\omega$  to calculate  $\mathbf{P}_{\text{NL}}$ , without loss of generality. For the remainder of this section, the modes under consideration will be referred to as  $a_\omega$  and  $a_{2\omega}$  for the fundamental and second harmonic, respectively. In this case, the nonlinear polarization is given by

$$\mathbf{P}_{\text{NL},\omega} = 2\epsilon_0 d_{\text{eff}} a_{2\omega} a_\omega^* \sum_{jk} \bar{d}_{ijk} E_{j,2\omega} E_{k,\omega}^* e^{-i(k_{2\omega} - k_\omega)z} \quad (3.5a)$$

$$\mathbf{P}_{\text{NL},2\omega} = \epsilon_0 d_{\text{eff}} a_\omega^2 \sum_{jk} \bar{d}_{ijk} E_{j,\omega} E_{k,\omega} e^{-2ik_\omega z} \quad (3.5b)$$

where  $i, j, k \in \{x, y, z\}$ .  $d_{\text{eff}} = \frac{2}{\pi} d_{33}$  is the effective nonlinear coefficient for a 50% duty cycle periodically poled waveguide, and  $\bar{d}_{ijk}$  is the normalized  $\chi^{(2)}$  tensor. For lithium niobate, this is expressed using contracted notation[80] in the coordinates of the crystal as

$$\bar{d}_{iJ} = \frac{1}{d_{33}} \begin{bmatrix} 0 & 0 & 0 & 0 & d_{15} & d_{16} \\ d_{16} & -d_{16} & 0 & d_{15} & 0 & 0 \\ d_{15} & d_{15} & d_{33} & 0 & 0 & 0 \end{bmatrix}$$

where  $d_{15} = 3.67$  pm/V,  $d_{16} = 1.78$  pm/V, and  $d_{33} = 20.5$  pm/V for SHG of 2- $\mu\text{m}$  light. These values are found using a least squares fit of Miller's delta scaling to the values reported in [81, 82],

and have relative uncertainties of  $\pm 5\%$ . We therefore expect a relative uncertainty in any calculated normalized efficiency to be  $\pm 10\%$ .

We arrive at the coupled wave equations for SHG by substituting Eqns. (3.5a-3.5b) into Eqn. (3.4) and defining  $A_\omega = \sqrt{P}a_\omega$

$$\partial_z A_\omega = -i\kappa A_{2\omega} A_\omega^* e^{-i\Delta kz}, \quad (3.6a)$$

$$\partial_z A_{2\omega} = -i\kappa^* A_\omega^2 e^{i\Delta kz}. \quad (3.6b)$$

We remark here that while the coupling coefficient  $\kappa$  can be complex due to the overlap integral in Eqn. 3.4, the phase of  $\kappa$  can be treated as a phase offset of  $A_{2\omega}$ . Furthermore, in many experimentally relevant contexts such as interactions between  $\text{TE}_{00}$  modes in a waveguide aligned to the crystalline Y-axis,  $\kappa$  is purely real. For these reasons, we neglect the phase of  $\kappa$ . The nonlinear coupling and the associated effective area are given by

$$\kappa = \frac{\sqrt{2Z_0}\omega d_{\text{eff}}}{cn_\omega \sqrt{A_{\text{eff}}} n_{2\omega}}, \quad (3.7a)$$

$$A_{\text{eff}} = \frac{A_{\text{mode},\omega}^2 A_{\text{mode},2\omega}}{\left| \int \sum_{i,j,k} \bar{d}_{ijk} e_{i,2\omega}^* e_{j,\omega} e_{k,\omega} dx dy \right|^2}. \quad (3.7b)$$

Tight confinement enhances the strength of nonlinear interactions by reducing the effective area,  $A_{\text{eff}}$ . For  $\text{TE}_{00}$  modes, the overlap integral in the denominator of  $A_{\text{eff}}$  is comparable to the geometric mean of the mode areas,  $\sqrt{A_{\text{mode},\omega} A_{\text{mode},2\omega}}$ , and therefore  $A_{\text{eff}} \sim A_{\text{mode},\omega}$ . This approximation gives us an intuitive picture of the strength of a nonlinear interactions as the waveguide geometry is varied.  $A_{\text{mode},\omega}$  decreases with decreasing waveguide dimensions, and approaches a local minimum for waveguide geometries comparable to the wavelength of the fundamental,  $A_{\text{mode},\omega} \sim (\lambda/n_\omega)^2$ . For structures with dimensions much smaller than the wavelength of the fundamental, the  $\text{TE}_{00}$  mode expands into the cladding and the nonlinear interaction becomes weaker. Typical values for the effective area for doubling wavelengths around 2- $\mu\text{m}$  are  $A_{\text{eff}} \sim 1\text{-}\mu\text{m}^2$ , which is a 50-fold improvement over previous generation proton-exchanged waveguides. Finally, we remark that the scale invariance of Maxwell's equations gives the minimum effective area a quadratic scaling with wavelength,  $A_{\text{eff}} \propto \lambda^2$ . Therefore, the optimal nonlinear coupling has a quadratic scaling in frequency,  $\kappa \propto \omega^2$ , and the power requirements for such devices scale as  $\omega^{-4}$ .

## 3.2 Nanophotonic PPLN Waveguides

Having established the nonlinear coupling in a nanophotonic waveguide, we now consider the design, fabrication, and characterization of CW SHG devices, as described in [83]. The devices considered here are designed for doubling 1550-nm light to generate a 775-nm second harmonic, since all of the

components necessary for characterization are readily available at these wavelengths.

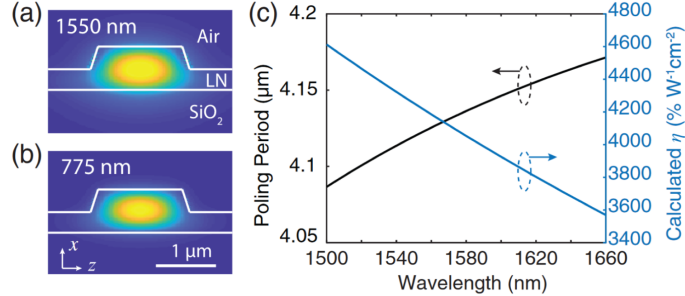


Figure 3.2: a) and b) Mode profiles ( $e_{\mu,Z}$ ) at 1550 nm and 775 nm, respectively. Here,  $X$  and  $Z$  denote the crystal axes of the MgO:LN thin film. c) Numerically calculated quasi-phasematching period (black) and theoretical conversion efficiency (blue) as a function of wavelength for a typical thin-film PPLN waveguide. Figure adapted from [83]

For CW interactions, designs typically take into account three quantities: i) the normalized efficiency,  $\eta_0 = \kappa^2$ , which is the typical figure of merit that determines the power requirements of a nonlinear device, ii) the poling period,  $\Lambda = 2\pi / (k_{2\omega} - 2k_\omega)$ , necessary to achieve quasi-phasematching, and iii) the sensitivity of the poling period with respect to fabrication errors. Most designs prioritize the latter; device geometries that minimize the sensitivity of poling period with respect to small variations in geometry often achieve performance comparable to theory. In this case, we find that the gradient of the poling period with respect to top width  $w$ , film thickness  $y$ , and etch depth  $h$ , is nearly constant over the range of geometries that we could fabricate,  $\partial_w \Lambda \sim 1$ , and  $\partial_h \Lambda \sim \partial_y \Lambda \sim 2$ . Therefore, we instead chose to prioritize both nonlinearity and ease of fabrication. A waveguide geometry of  $w \sim 1400$  nm,  $y \sim 600$  nm and  $h \sim 300$  nm yields low loss, poling periods greater than  $4 \mu\text{m}$ , and a calculated normalized efficiency of  $> 4000\%/W\text{-cm}^2$ . This design is summarized in Fig. 3.2, which shows the calculated TE<sub>00</sub> waveguide modes at 1550 nm and 775 nm (Fig. 3.2(a-b)), and their associated normalized conversion efficiency and poling period (Fig. 3.2(c)).

These waveguides are fabricated in three steps. First, we periodically pole an x-cut magnesium-oxide- (MgO-) doped lithium niobate thin film (NANOLN) (Fig. 3.3(a)). The metal electrodes consist of a 15-nm-thick Cr adhesion layer and a 150-nm-thick Au layer, deposited by electron-beam evaporation. We perform the periodic domain inversion by applying several 580 V, 5-ms-long pulses at room temperature with the sample submerged in oil, which corresponds to a poling electric field of  $\sim 7.6$  kV/mm. The inset shows a colorized 2-photon microscope image of the resulting inverted domains with a duty cycle of  $\sim 50\%$ . The poled region has a width of  $25 \mu\text{m}$  and a length of 4 mm. After periodic poling, we remove the electrodes using metal etchant. The second step is performed at the Harvard Center for Nanoscale Systems. Here, aligned electron-beam lithography is used to create waveguide patterns inside the poled region. Each poled region can accommodate multiple ridge waveguides (three in our case) without cross-talk due to the strong optical confinement, allowing

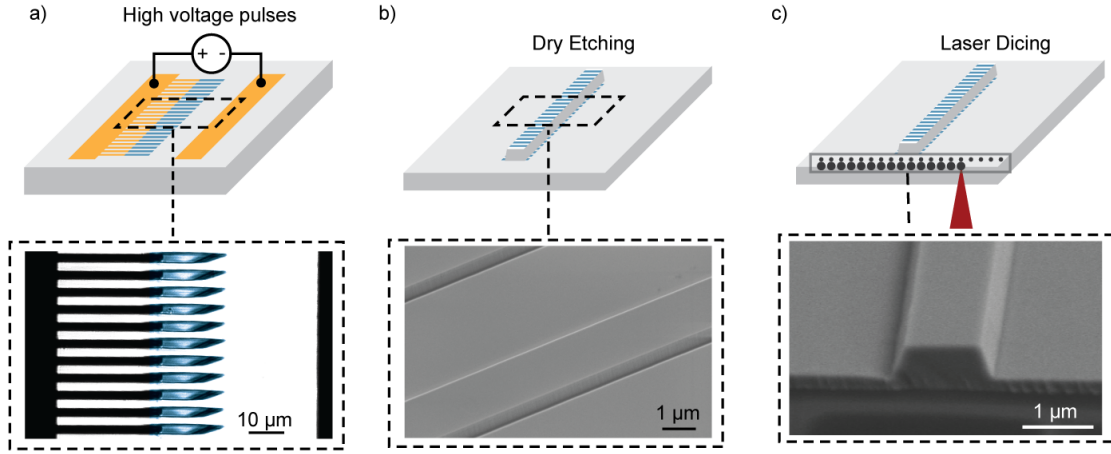


Figure 3.3: a) Schematic of the poling process, resulting in high fidelity domain inversion with a  $\sim 50\%$  duty cycle. b) Waveguides are patterned using an  $\text{Ar}^+$  assisted dry etch, resulting in smooth sidewalls. c) The samples are prepared using laser dicing, resulting in optical-quality end-facets.

for dense device integration. The patterns are then transferred to the LN device layer using an optimized  $\text{Ar}^+$ -based dry etching process to form ridge waveguides[73]. This yields low-loss ( $\sim 0.03$  dB/cm) ridge waveguides (Fig. 3.3(b)). The inset shows a scanning electron microscope (SEM) image of the ridge waveguides, showing smooth sidewalls. Finally, facet preparation is done using a DISCO DFL7340 laser saw (Fig. 3.3(c)). Here,  $\sim 10\text{-}\mu\text{J}$  pulses are focused into the substrate to create a periodic array of damage spots, which act as nucleation sites for crack propagation. The sample is then cleaved. The inset shows an SEM image of the resulting end-facets, which exhibit  $<10\text{-nm}$  facet roughness.

We remark here that the devices studied throughout the remainder of this section were among the first attempts at fabricating PPLN nanophotonic devices. Non-idealities in both poling and facet preparation yielded devices with poling duty cycles closer to 40% and rough facets with  $\sim 10$  dB loss per facet. Upon further revision, the techniques described above have yielded duty cycles close to 50%, and coupling efficiencies as high as 30%.

We characterize these devices by measuring the SHG transfer function,  $\text{sinc}^2(\Delta kL/2)$ , the normalized efficiency,  $\eta_0$ , and the maximum attainable conversion efficiency when the device is driven into saturation. We begin with the SHG transfer function, which determines the wavelength that achieves phasematching,  $\lambda_{\text{PM}}$ , and can help characterize inhomogeneities of the fabricated devices. A schematic of this experiment is shown in Fig. 3.4(a). Pump light from a continuous-wave telecom tunable laser source (Santec TSL-510, 1480-1680 nm) is end-fired into the waveguides using a lensed fiber, and the generated SH power is measured as a function of input wavelength. An in-line fiber

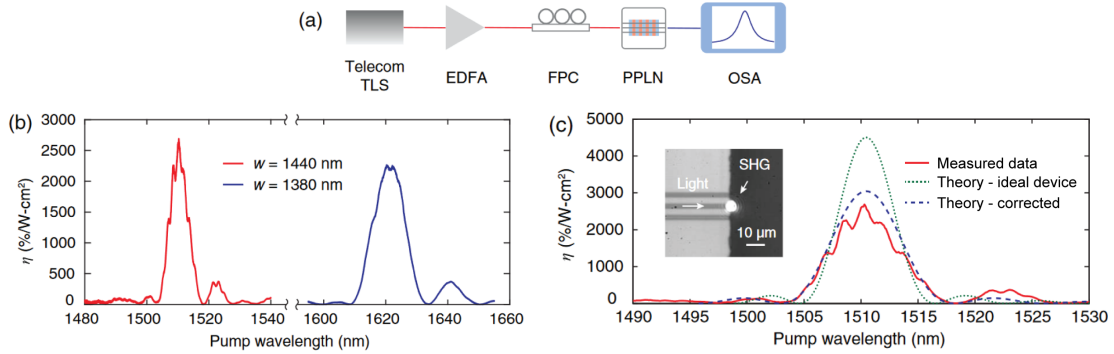


Figure 3.4: a) Schematic of the characterization setup. b) Measured SHG conversion efficiency versus pump wavelengths for two waveguides with the same poling period but different top widths. (c) Zoom-in view of the SHG spectral response of the 1440-nm-wide device (solid curve), together with the theoretically predicted responses. The green dotted and blue dashed curves correspond to the ideal and corrected transfer functions, respectively. Inset shows a CCD camera image of the scattered SHG light at the output waveguide facet. TLS, tunable laser source; EDFA, erbium-doped fiber amplifier; FPC, fiber polarization controller; OSA, optical spectrum analyzer.

polarization controller is used to ensure TE polarization at the input. When the pump laser is tuned to the QPM wavelength, strong scattered SH light can be observed at the waveguide output facet using a CCD camera from the top of the chip, as shown in the inset of Fig. 3.4(c). After passing through the waveguide, the generated SH light is collected using a second lensed fiber and sent to a visible photo detector (EO Systems) for further analysis. Fig. 3.4(b) shows the measured SHG responses of two waveguides with the same poling period and slightly different top widths of 1440 nm and 1380 nm. Here the fiber-to-chip coupling losses of  $\sim 10$  dB/facet have been calibrated and extracted by measuring the linear optical transmission at both FH and SH wavelengths. The differences between the coupling efficiencies of the input and output facets have been de-embedded by comparing the SHG efficiencies when pumping from different sides of the waveguide. The on-chip optical loss at telecom wavelengths is estimated to be  $< 1$  dB from the interference fringes of the optical transmission spectrum. The normalized conversion efficiency is determined for  $\lambda_{PM}$  by measuring the slope of conversion efficiency with respect to pump power,  $P_{2\omega}/P_{\omega} = \eta_0 P_{\omega} L^2$ .

The measured SHG spectral response and conversion efficiency can be well explained using a corrected transfer function model. Fig. 3.4(c) shows a zoom-in view of the SHG response of the 1440-nm-wide device. The green dotted curve corresponds to the theoretically calculated SHG transfer function,  $\text{sinc}(\Delta^2 k(\Omega)L/2)$ , in the ideal case showing a maximum normalized conversion efficiency of  $4500\%/W\text{cm}^2$ . In comparison, our measured SHG response shows a slightly broadened transfer function with a lowered maximum efficiency ( $2600\%/W\text{cm}^2$ ), likely due to inhomogeneity of the thin-film thickness causing axial variations of the phase-mismatch throughout the 4-mm-long

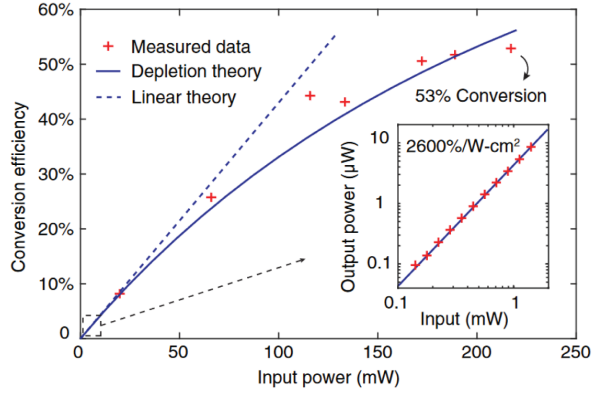


Figure 3.5: SHG conversion efficiency as a function of input power in the saturated limit. Inset shows the conversion efficiency in the undepleted limit.

waveguide. While a full characterization of device inhomogeneity would require a phase-sensitive measurement [84], we can verify that such inhomogeneity is responsible for the discrepancy between theory and experiment. In the absence of pump depletion, inhomogeneous broadening conserves the area of the transfer function; we therefore compare the areas under the measured and calculated transfer functions over the laser tuning bandwidth, which yields a correction factor of 1.28. Using this number, we obtain a corrected transfer function, shown as the blue dashed curve in Fig. 3.4(c). The corrected transfer function also takes into account the effect from the actual poling duty cycle of  $\sim 39\% \pm 3\%$ , which reduces  $d_{\text{eff}}$  by 7%. This non-ideal duty cycle is likely due to less-than-expected domain widening during the poling process, while the non-uniformity could result from variations in the thin-film thickness. After these corrections, the calculated transfer function shows good agreement with the measured curve in terms of maximum efficiency, QPM bandwidth, and side lobe position and shape. The remaining discrepancy between theory and experiment could be attributed to waveguide losses and unoptimized input polarization. Even with these non-idealities, the devices shown here exhibit a 30-fold improvement in normalized efficiency when compared to state of the art proton-exchanged waveguides.

Having characterized the behavior of these devices in the undepleted limit, we now consider the saturated regime, where the conversion efficiency scales as  $P_{2\omega}/P_{\omega} = \tanh^2(\kappa\sqrt{P_{\omega}}L)$ . The results are shown in Fig. 3.5. We use an erbium-doped fiber amplifier (EDFA, Amonics) to further increase the optical power from the pump laser. At the output end, we use an optical spectrum analyzer (OSA, Yokogawa) to simultaneously monitor the optical power at FH and SH wavelengths to measure the pump-depletion ratio. The highest measured absolute conversion efficiency in our devices is 53%, corresponding to the generation of  $\sim 117$  mW at 775 nm in the waveguide using a pump power of 220 mW (Fig.3.5). Even with the large generated SH optical intensity of  $\sim 10$  MW/cm<sup>2</sup> inside the waveguide, we do not observe photorefractive damage of the device after many

hours of optical pumping. The measured pump-depletion agrees well with the theoretical prediction based on the measured normalized conversion efficiency in the low-conversion limit (Fig. 3.5, inset).

These results confirm that quasi-phases-matched SHG in a direct-etched nanophotonic PPLN ridge waveguide achieves efficient nonlinear interactions with more than an order of magnitude less power than state-of-the-art diffused waveguides. While the measured transfer functions suggest that the fabricated devices exhibit some performance degradation due to film thickness variations, such problems will improve as geometries that achieve non-critical phasematching become more accessible.

### 3.3 Pulsed Second Harmonic Generation

We now consider pulsed SHG in nanophotonic PPLN devices. While CW nanophotonic devices exhibit qualitatively similar behavior to devices based on diffused waveguides, albeit with substantially larger nonlinearities, pulsed interactions can be substantially modified by the geometric dispersion of the waveguide. In particular, we will show that the dispersion of a nanophotonic PPLN device can be engineered to achieve long interaction lengths with femtosecond pulses, which can reduce the energy requirements of these devices by several orders of magnitude, from picojoules to femtojoules. This approach is not possible in devices that rely on modal phasematching[85, 86], where the waveguide geometry is constrained to achieve  $n_{2\omega} = n_\omega$  and cannot be varied to engineer higher dispersion orders. In the experiments considered here, we are able to suppress temporal walk-off between the interacting harmonics, as well as the group velocity dispersion of the fundamental, thereby enabling SHG of a 50-fs pulse in a 6-mm-long nanophotonic device. The combination of a short pulse, a long interaction length, and the large nonlinearity associated with sub-wavelength confinement results in conversion efficiencies in excess of 50% with as little as 60 fJ of input pulse energy (or 4.5  $\mu$ W of average power)[87]. The structure of this section mirrors that of Sec. 3.2. First, we discuss the design and fabrication of dispersion-engineered nanophotonic devices. Then, we characterize these devices in terms of their transfer function, normalized efficiency, and behavior in saturation.

We begin by revisiting the role of dispersion in pulsed nonlinear interactions. The coupled wave equations for second harmonic generation of an ultrafast pulse are

$$\partial_z A_\omega(z, t) = -i\kappa A_{2\omega} A_\omega^* \exp(-i\Delta k z) + \hat{D}_\omega A_\omega \quad (3.8a)$$

$$\partial_z A_{2\omega}(z, t) = -i\kappa A_\omega^2 \exp(i\Delta k z) - \Delta k' \partial_t A_{2\omega} + \hat{D}_{2\omega} A_{2\omega} \quad (3.8b)$$

where  $A_\omega$  and  $A_{2\omega}$  are the complex amplitudes of the modal fields, normalized so that  $|A(z, t)|^2$  the instantaneous power at position  $z$ . These equations are scale invariant; the solutions of Eqns. 3.8a-3.8b are unchanged by the transformation  $z \rightarrow sz$ ,  $\Delta k \rightarrow \Delta k/s$ ,  $\Delta k' \rightarrow \Delta k'/s$ ,  $\hat{D}_{\omega,2\omega} \rightarrow \hat{D}_{\omega,2\omega}/s$ ,  $A_{\omega,2\omega} \rightarrow A_{\omega,2\omega}/s$ . Therefore, reductions in the temporal walkoff, phase-mismatch, and the dispersion operators by a factor  $s$  allows for an increase of the length of the device by  $s$  and a corresponding

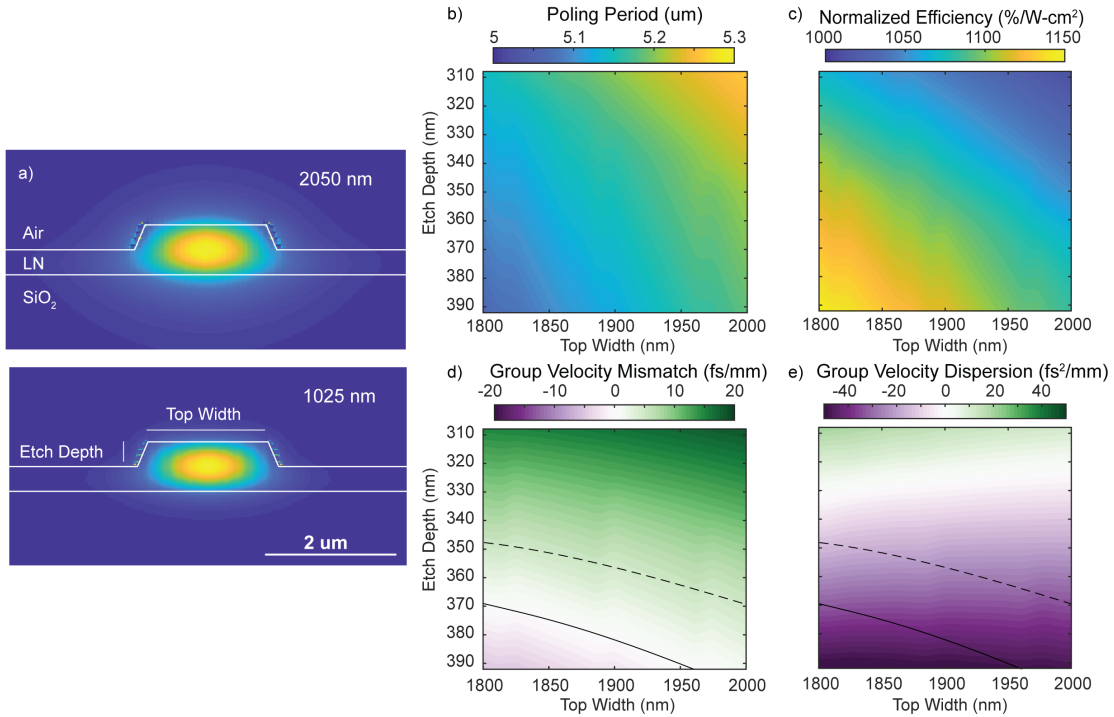


Figure 3.6: a) Waveguide cross-section, showing the normalized electric field associated with the simulated  $TE_{00}$  fundamental (above) and second harmonic (below) modes. The waveguides shown here correspond to a top width of 1850 nm, an etch depth of 350 nm, and a starting film thickness of 700 nm. b,c) Simulated poling period and normalized efficiency, respectively, as a function of waveguide geometry. d,e) Simulated  $\Delta k'$  and  $k''_{\omega}$ , respectively. The solid black line denotes  $\Delta k' = 0$ , and the dashed black contour line shows geometries that achieve  $|\Delta k'| < 5\text{fs/mm}$ .

$s^2$  reduction in the power requirements needed to achieve the same dynamics. A similar scaling law holds for the duration,  $\tau$ , of the short pulses input to the waveguide. Rescaling the time coordinates,  $t \rightarrow t/s$ ,  $\tau \rightarrow \tau/s$ ,  $A_{\omega,2\omega} \rightarrow A_{\omega,2\omega}/s^{1/2}$ ,  $\Delta k' \rightarrow \Delta k'/s$ , and  $k_{\omega,2\omega}^{(m)} \rightarrow k_{\omega,2\omega}^{(m)}/s^m$  yields the same dynamics with a compressed time-axis. In both of these cases, reducing the waveguide dispersion facilitates a reduction in the energy required to achieve efficient nonlinear interactions, either by allowing for longer interaction lengths or shorter pulses. While a simultaneous reduction of every dispersion order in accordance with the above scaling laws is difficult to achieve with simple ridge waveguides, we may still realize long interaction lengths of short pulses by reducing the leading dispersion orders. In our discussion of pulsed SHG in Sec. 1.4, we determined that the amount of bandwidth of the fundamental that can contribute to SHG,  $\Omega'$ , is determined to leading order by  $k''_{\omega}$ , and that the amount of bandwidth,  $\Omega$ , generated at the second harmonic is limited to leading order by the temporal walk-off between the waves,  $\Delta k'$ . We therefore focus on modifying these dispersion orders using the waveguide geometry.

The design of these waveguides is shown in Fig. 3.6. In this case, we consider SHG of short pulses centered around a wavelength of 2050-nm. A cross-section of the typical ridge waveguide under consideration is shown in Fig. 3.6(a), with the simulated  $TE_{00}$  modal field amplitude of the fundamental and second harmonic, respectively. We assume a 700-nm x-cut thin film, and examine the roles of etch depth and waveguide width on the performance of the waveguide in Figs. 3.6(b-e). The poling period is shown as a function of waveguide geometry in Fig. 3.6(b), and exhibits a linear scaling in width and etch depth, with larger waveguides having larger poling periods.  $\eta_0$  is shown in Fig. 3.6(c), and scales with the inverse of the area of the waveguide modes. The effective area,  $A_{\text{eff}}$ , is  $1.6 \mu\text{m}^2$  for SHG between the modes shown in Fig. 3.6(a).  $\Delta k'$  and  $k''_{\omega}$  are shown in Fig. 3.6(d) and Fig. 3.6(e) respectively. Temporal walkoff becomes negligible for etch depths  $> 350$ -nm, and anomalous dispersion occurs for etch depths  $> 330$ -nm.

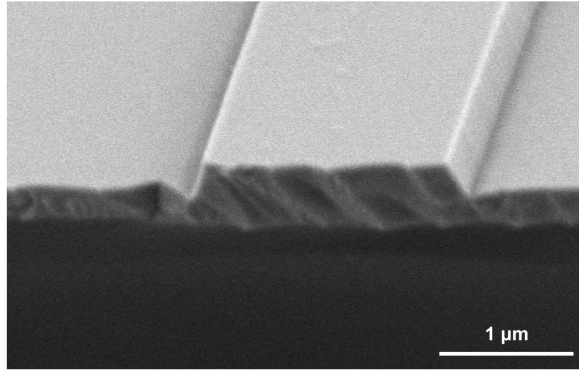


Figure 3.7: SEM image of one of the fabricated waveguides.

As a compromise between minimizing these dispersion orders, we choose a design with a top width of  $\sim 1850$  nm, and an etch depth of  $\sim 340$  nm. Using the methods described in Sec. 3.2, we fabricated 45 6-mm-long waveguides corresponding to three different top widths and 15 poling periods ranging from  $5.01\text{-}\mu\text{m}$  to  $5.15\text{-}\mu\text{m}$  (Fig. 3.7). We chose the 10-nm shift between consecutive poling periods to correspond to a shift of  $\Delta kL$  by  $4\pi$ , and use temperature for fine tuning of the phase-mismatch. The yield for poling and waveguide fabrication was 50% and 90%, respectively, and the coupling efficiency varied from 0.03% to 1% depending on the quality of the end-facet, with 10% of the waveguides exhibiting facet damage. We note here that theoretical coupling efficiencies in excess of 30% are possible with the  $\text{NA}=0.5$  optics used throughout this chapter, and that further refinements of both the facet preparation recipe and the in-coupled Gaussian beam have yielded devices with coupling efficiencies commensurate with theory. For the remainder of this paper we will report pulse energies internal to the waveguide and focus on waveguides with a top width of  $\sim 1850$  nm and an etch depth of  $\sim 340$  nm, which achieve phasematching near a period of  $5.11\text{-}\mu\text{m}$ .

The resulting theoretical normalized efficiency is 1100%/W-cm<sup>2</sup>,  $\Delta k' = 5$ -fs/mm, and  $k''_{\omega} = -15$ -fs<sup>2</sup>/mm. The calculated value of  $\Delta k'$  is 20 times smaller than that of bulk lithium niobate for 2- $\mu$ m doubling, which allows for substantially longer interaction lengths for femtosecond pulses.

We now characterize the performance of these devices in terms of their SHG transfer functions, normalized efficiency, and total achievable efficiency in saturation. For SHG in the limit where the fundamental wave is undepleted, Eqns. 3.8a-3.8b may be solved using the transfer function approach described in Sec. 1.4. Since  $k''_{\omega}$  is small, we compute the response of the second harmonic to the driving nonlinear polarization by filtering the driving polarization with the transfer function for CW SHG. We implement this approach analytically in two steps. First we calculate the second harmonic envelope that would be generated in the absence of dispersion,  $A_{2\omega}^{\text{ND}}(z, t) = -i\kappa A_{\omega}^2(0, t)z$ . Then, the power spectral density associated with this envelope is filtered in the frequency domain, using the CW transfer function for SHG

$$|A_{2\omega}(z, \Omega)|^2 = \text{sinc}^2(\Delta k(\Omega)z/2)|A_{2\omega}^{\text{ND}}(z, \Omega)|^2. \quad (3.9)$$

Here,  $A_{2\omega}(z, \Omega) = \mathcal{F}\{A_{2\omega}(z, t)\}(\Omega)$  is the Fourier transform of  $A_{2\omega}(z, t)$ , and  $\Omega$  is the frequency detuning around  $2\omega$ . The dispersion of a nonlinear waveguide modifies the bandwidth of the SHG transfer function through the frequency dependence of  $\Delta k(\Omega) = k(2\omega + 2\Omega) - 2k(\omega + \Omega) - 2\pi/\Lambda$ . In conventional quasi-phasematched devices, the bandwidth of the generated second harmonic is typically dominated by the group-velocity mismatch between the fundamental and second harmonic,  $\Delta k(\Omega) \approx 2\Delta k'\Omega$ , with corresponding scaling law for the generated second harmonic bandwidth  $\Delta\lambda_{\text{SHG}} \propto 1/|\Delta k'|L$ . As discussed previously, the geometric dispersion that arises due to tight confinement in a nanophotonic waveguide may substantially alter  $\Delta k'$ . Ultra-broadband interactions become possible when the geometric dispersion of a tightly confining waveguide balances the material dispersion, thus achieving  $\Delta k' = 0$ . For the waveguides fabricated here, both  $\Delta k'$  and  $k''_{\omega}$  are small. In this case the corresponding SHG bandwidth becomes dominated by higher order dispersion, and  $\Delta k(\Omega)$  must be calculated using the full dispersion relations of the TE<sub>00</sub> fundamental and second harmonic modes.

The experimental setup is shown in Fig. 3.8(a). We characterize the behavior of 6-mm-long nanophotonic PPLN waveguides using using nearly transform-limited 50-fs-long pulses from the synchronously pumped degenerate optical parametric oscillator described in [27]. We use reflective inverse-Cassegrain lenses (Thorlabs LMM-40X-P01) both to couple into the sample and to collect the output. This ensures that the in-coupled pulses are chirp-free, and that the collected harmonics are free of chromatic aberrations. To characterize the SHG transfer function, we record the spectrum input to the waveguide at the fundamental and output from the waveguide at the second harmonic. Then, we estimate  $A_{2\omega}^{\text{ND}}(z, \Omega) \propto A_{\omega}(z, \Omega) * A_{\omega}(z, \Omega)$  using the auto-convolution of the spectrum of the fundamental, shown in Fig. 3.8(b). The ratio of the measured second harmonic spectrum (Fig. 3.8(c)) with  $A_{2\omega}^{\text{ND}}$  yields the measured SHG transfer function (Fig. 3.8(d)), showing good

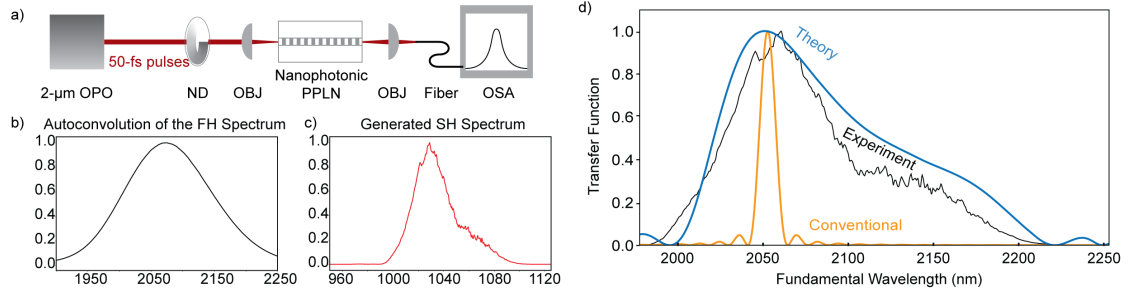


Figure 3.8: a) Schematic of experimental setup. ND- variable neutral density filter, OBJ- reflective objective lens, OSA- optical spectrum analyzer. b,c) Measured spectrum of the driving polarization ( $|A_\omega(0, \Omega) * A_\omega(0, \Omega)|^2$ ) and output second harmonic ( $|A_{2\omega}(L, \Omega)|^2$ ), respectively. d) Measured SHG transfer function (black) for a 6-mm-long nanophotonic waveguide, showing good agreement with theory (blue). The bandwidth of these waveguides exceeds that of bulk PPLN (orange) by more than an order of magnitude.

agreement between experiment and theory. These devices exhibit a bandwidth  $>250$  nm, when measured between the zeros of the transfer function, which outperforms bulk 2-μm SHG devices of the same length in PPLN by an order of magnitude. This broad transfer function confirms that the waveguide achieves quasi-static interactions of short pulses across the length of the device.

The conversion efficiency of the second harmonic and depletion of the fundamental input to the waveguide is shown as a function of input pulse energy in Fig. 3.9. The inset shows the undepleted regime, denoted by the dotted box. The dotted line is a theoretical fit of Eqn. 3.9, where we have accounted for a small degree of saturation at the peak of the pulse by using  $A_{2\omega}^{\text{ND}}(z, t) = -iA_\omega(0, t) \tanh(\kappa A_\omega(0, t)z)$ . The only fitting parameter used here is a peak CW normalized efficiency of  $1000\%/W\text{-cm}^2$ , which agrees well with the theoretically predicted value of  $1100\%/W\text{-cm}^2$ , and represents a 45-fold improvement over conventional 2-μm SHG devices based on proton-exchanged waveguides. When this large CW normalized efficiency is combined with the peak field associated with a 50-fs-long pulse these waveguides achieve 50% conversion efficiency for an input pulse energy of only 60 fJ, which is a 30-fold reduction compared to the state of the art[88].

These results represent the first demonstration of a quasi-phasematched device with co-engineered waveguide dispersion, and confirm that the interaction lengths of short pulses in a PPLN waveguide can be extended by more than an order of magnitude with a suitable choice of waveguide design. By suppressing both the temporal walk-off between the harmonics and the group velocity dispersion of the fundamental, we are able to perform SHG of 50-fs-long pulses in a 6-mm-long waveguide, which enables efficient nonlinear optics at the femtojoule level.

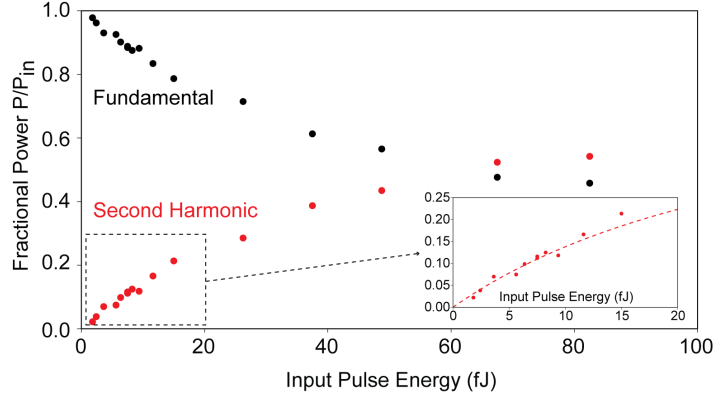


Figure 3.9: SHG conversion efficiency and pump depletion as a function of input pulse energy, showing 50% conversion efficiency with an input pulse energy of 60-fJ. Inset: Undepleted regime with fit given by Eqn. (3.9) and a heuristic model for saturation, as described in the text.

### 3.4 Cascaded Nonlinearities in Nanophotonic PPLN Devices

Having established the behavior of phase-matched SHG devices, we now consider the behavior of phase-mismatched devices. As discussed in section 1.4.2, it can be shown that in the limit of large phase-mismatch the coupled wave equations can be reduced to an effective nonlinear Schrödinger equation (NLSE) for the fundamental wave[89, 40],

$$\partial_z A_\omega = \frac{ik''_\omega}{2} \partial_t^2 A_\omega + i\gamma_{\text{SPM}} |A_\omega|^2 A_\omega, \quad (3.10)$$

where  $\gamma_{\text{SPM}} = -\eta_0/\Delta k$ . Here, self-phase modulation of the fundamental occurs due to back-action of the second harmonic on the fundamental.

Eqn. 3.10 is valid when the phase-mismatch is sufficiently large to satisfy two criteria:  $|\Delta k| \gg \kappa A_0$ , where  $A_0 = \max(|A_\omega(0, t)|)$ , and  $|\Delta k| \gg 4\pi|\Delta k'/\tau|$ , where  $\tau$  is the transform-limited duration of the pulse input to the waveguide. Typically the bounds of  $\Delta k$ , and thus the strength of the effective self-phase modulation, are set by the temporal walk-off. This constraint is lifted when  $\Delta k' \sim 0$ . For modest values of the phase mismatch ( $\Delta k \sim 1 \text{ mm}^{-1}$ ) and the CW normalized efficiency measured previously, the effective nonlinearity is  $\gamma_{\text{SPM}} = 100/\text{W-m}$ . This corresponds to an effective nonlinear refractive index of  $n_2 = 4.8 \times 10^{-17} \text{ m}^2/\text{W}$ . We may compare this to the  $n_2$  associated with Kerr nonlinearities in lithium niobate by scaling the values found in [90] with a two-band model[91]. We find  $n_2 = 2.6 \times 10^{-19} \text{ m}^2/\text{W}$  at 2050-nm, which is 185 times weaker than the self-phase modulation due to cascaded nonlinearities. For comparison, typical numbers for  $\gamma_{\text{SPM}}$  based on Kerr nonlinearities in silicon, silicon nitride, and lithium niobate are 38/W-m, 3.25/W-m, and 0.4/W-m respectively[92, 50, 93]. In addition to this large nonlinearity, we again note that the solutions of the effective NLSE are preserved by the transformation  $z \rightarrow sz$ ,  $k''_\omega \rightarrow k''_\omega/s$ ,  $\Delta k \rightarrow \Delta k/s$  and  $A_\omega \rightarrow A_\omega/s$ .

Longer waveguides with smaller dispersion achieve larger effective nonlinearities for SPM due to the smaller  $\Delta k$ , and correspondingly exhibit a quadratic decrease in the energy requirements to achieve spectral broadening. In contrast, waveguides based on true  $\chi^{(3)}$  nonlinearities are scale invariant under the transformation  $z \rightarrow sz$ ,  $k''_{\omega} \rightarrow k''_{\omega}/s$ ,  $A_{\omega} \rightarrow A_{\omega}/s^{1/2}$ , and therefore only exhibit a linear reduction in energy requirements as the waveguide is made longer. The large effective  $n_2$  calculated above, with the  $P \propto L^{(-2)}$  scaling associated with  $\chi^{(2)}$  interactions, suggests that cascaded  $\chi^{(2)}$  nonlinearities in dispersion-engineered nanowaveguides can be used to achieve dynamical processes such as supercontinuum generation with substantially lower pulse energies than approaches based on  $\chi^{(3)}$  nonlinearities. In practice, the full nonlinear polarization generates a cascade of mixing processes which leads to spectral broadening of several harmonics; a heuristic picture of this process is beyond the scope of the treatment presented here. A more general treatment that accounts for the effects of saturation and the broadening of the second harmonic is presented in Ch. 3.6.

### 3.5 Supercontinuum Generation

Having established the large effective  $\chi^{(3)}$  nonlinearity associated with cascaded  $\chi^{(2)}$  interactions in nonlinear nanophotonic devices, we now study supercontinuum generation in a dispersion-engineered PPLN waveguide. The performance of these waveguides, as characterized by the pulse energies required to generate an octave of bandwidth at multiple harmonics, is an improvement over previous demonstrations in lithium niobate by more than two orders of magnitude, from nanojoules to picjoules. We note here that while the analysis based on cascaded nonlinearities above motivated this experimental study, it was later determined that the dynamical processes responsible for the observed spectral broadening are dominated by amplitude modulations, rather than self-phase modulation. These processes will be discussed in section 3.6.

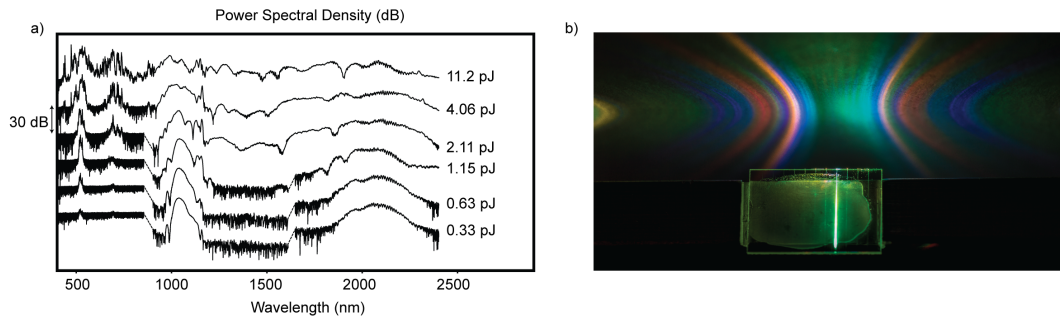


Figure 3.10: a) Evolution of power spectral density over an order of magnitude variation of pulse energy. Adjacent traces are displaced by 30 dB for clarity. The different noise floors correspond to the three spectrometers used, and dotted lines have been added to guide the eye where discontinuities in these noise floors are present. b) Photograph of supercontinuum produced with 11-pJ input to the waveguide.

We characterize SCG in a nanophotonic PPLN waveguide with the OPO source and waveguide geometry used in the SHG experiment, however the poling period is now chosen such that  $\Delta kL = 3\pi$ . We record the output spectrum from the waveguide using three spectrometers: the visible to near-infrared (400-900 nm) range is captured with a Ocean Optics USB4000, the near- to mid-infrared (900-1600 nm) is captured with a Yokogawa AQ6370C, and the mid-infrared (1600-2400 nm) is captured using a Yokogawa AQ6375. The results are shown in Fig. 3.10. The fundamental, second harmonic, and fourth harmonic are observed for input pulse energies as low as 0.5-pJ. For pulse energies  $>1$ -pJ, the first two harmonics undergo spectral broadening, and we observe buildup of the third harmonic. As the waveguide is driven with larger pulse energies, all of the observed harmonics undergo spectral broadening. The first two harmonics merge into a supercontinuum spanning more than an octave when driven with 2-pJ of pulse energy. When driven with pulse energies in excess of 10-pJ, the first five harmonics undergo spectral broadening and merge together to form a supercontinuum spanning  $>2.5$  octaves at the -30 dB level. The measured supercontinuum is limited to wavelengths  $> 400$  nm by the transparency window of our collection optics, and  $< 2400$  nm by our available spectrometers. A photograph of the multi-octave supercontinuum is shown in Fig. 3.10(b). The observed diffraction pattern is due to leakage of visible frequencies into slab-waveguide modes. The evanescent tails of these modes sample the periodic substrate damage from laser dicing, which acts as a diffraction grating.

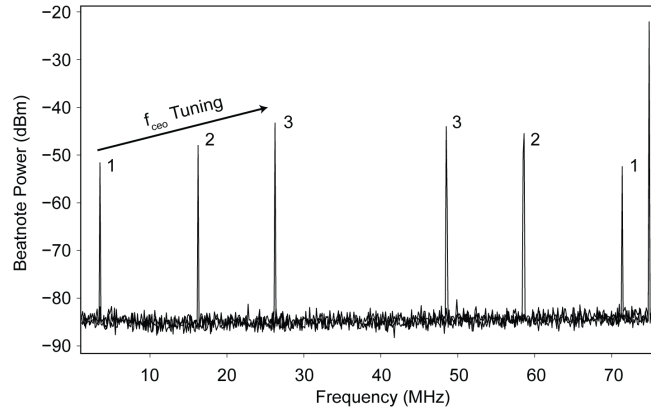


Figure 3.11: Measured carrier-envelope-offset beatnotes for three different values of intracavity dispersion in the laser used to pump the OPO.

To characterize the coherence of this multi-octave supercontinuum, we measure the carrier-envelope-offset frequency ( $f_{ceo}$ ) using beatnotes that arise due to the overlap of the fundamental and second harmonic. The experimental setup is the same as for SHG and SCG, except that the light output from the waveguide is filtered using a Thorlabs FELH-1350 longpass filter, and focused onto a Hamamatsu C12668-02 InGaAs photoreceiver. The recorded  $f_{ceo}$  beatnotes are shown in Fig. 3.11, alongside a 75 MHz beatnote corresponding to the repetition frequency of the OPO. We verify

that the observed beatnotes correspond to the  $f_{\text{ceo}}$  by tuning the  $f_{\text{ceo}}$  of the OPO in two steps: i) we tune the  $f_{\text{ceo}}$  of the laser used to pump the OPO by translating an intracavity prism, and ii) we monitor the spectrum of the OPO to verify that it maintains degenerate operation, and therefore remains phase-locked to the pump laser as the  $f_{\text{ceo}}$  is tuned. We achieve a 35-dB signal-to-noise ratio in a 3-kHz resolution bandwidth, limited by the noise floor of the photoreceiver. Furthermore, we remark that the intensity of the  $f_{\text{ceo}}$  beatnotes are only  $\sim 22$ -dB below the intensity of the repetition frequency beatnote. This bright relative intensity is due to the beatnotes remaining coherent and in-phase across the entire 400-nm-wide bandwidth incident on the photodetector.

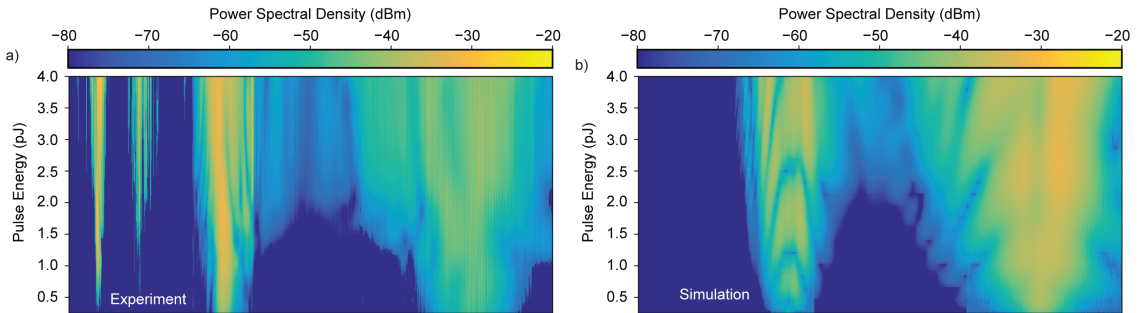


Figure 3.12: Power spectral density output from the chip as a function of input pulse energy a) Experiment, b) Simulation. The power in dBm is measured in 2-nm-wide spectral bins.

To better understand the dynamics and coherence properties of the generated supercontinuum, we simulate Eqns. (3.8a-3.8b) using the split-step fourier method described in Sec. 1.5, including dispersion to third order saturation. The experimentally measured and simulated spectra output from the waveguide are shown in Figs. 3.12(a) and 3.12(b), respectively. We note that the simulation includes semi-classical vacuum noise and that the results have been renormalized to account for outcoupling such that the simulation and experiment have the same peak power spectral density in the near-infrared band (900-1600 nm) when driven with a pulse energy of 4-pJ. The two-envelope model used here captures many of the features of the experiment except for the buildup of the higher harmonics, which have been explicitly neglected by only considering  $A_\omega$  and  $A_{2\omega}$  in the coupled wave equations.

We note here that the observed spectral broadening exhibits qualitative agreement with traditional heuristics derived from the nonlinear Schrödinger equation. If we define the soliton number as  $N^2 = \gamma_{\text{SPM}} U \tau_s / (2k''_\omega)$ , where  $U$  is the input pulse energy, and  $\tau_s = \tau / 1.76$ , then the soliton fission length is given by  $L_s = \tau_s^2 / N k''_\omega$ . The soliton fission length approaches the length of the device for an input pulse energy of 1 pJ, which is the energy at which the observed output spectra begin to exhibit spectral broadening. Supercontinuum generation occurs for pulse energies in excess of 2 pJ. As discussed earlier, a more rigorous heuristic model of spectral broadening in these devices is presented in Sec. 3.6.

Having shown strong agreement between the simulated and experimental spectral broadening, we now consider the coherence properties of the generated supercontinuum. Fig. 3.13 shows the simulated coherence function,  $|g^{(1)}(\lambda, 0)|$ [45], which has been calculated using an ensemble average of 100 simulations, for an input pulse energy of 4-pJ ( $N = 14$ ). The simulations shown here suggest that the spectra are coherent over the range of pulse energies considered, with a calculated  $\langle |g^{(1)}| \rangle = \int |g^{(1)}(\lambda, 0)| |A(\lambda)|^2 d\lambda / \int |A(\lambda)|^2 d\lambda$  of 0.9996 and 0.9990 for the fundamental and second harmonic, respectively. This suggests that decoherence mechanisms that arise due to SPM such as modulation instabilities, are absent for the devices under study. However, we note that the approach used here neglects many possible decoherence mechanisms, such as degenerate parametric fluorescence of the third harmonic. Remarkably, the results shown in 3.11, with the simulations considered here, suggest that these multi-octave supercontinua are coherent for soliton numbers as high as  $N = 20$ . Conventional approaches to SCG typically exhibit decoherence for soliton numbers as low as  $N = 10$ , which suggests that the process under study here has different decoherence mechanisms than traditional  $\chi^{(3)}$  devices.

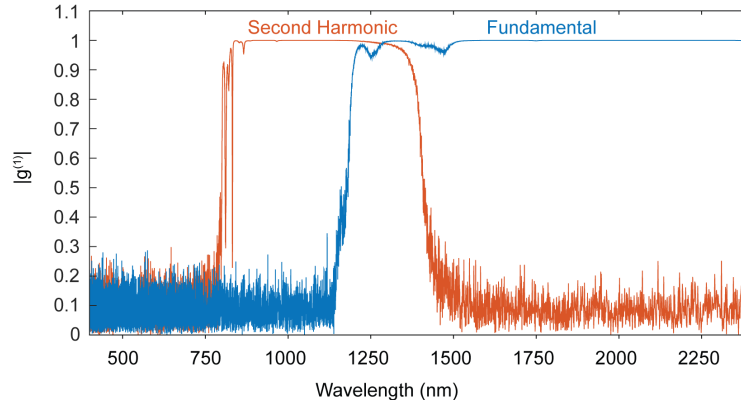


Figure 3.13: Simulated coherence of the fundamental and second harmonic generated by a 4-pJ pulse, showing  $|g^{(1)}| \sim 1$ .

We conclude this section by comparing these results to previous demonstrations in lithium niobate waveguides. In proton-exchanged PPLN waveguides utilizing cascaded nonlinearities, multiple coherent spectrally broadened harmonics were achieved using 5-nJ of pulse energy[90]. Substantial energy reductions were observed in nanophotonic lithium niobate waveguides using  $\chi^{(3)}$  nonlinearities, where spectral broadening of the first two harmonics was observed with 150-pJ of pulse energy[94]. The results presented here achieve a bandwidth comparable to [90], with less pulse energy than any previous demonstration in lithium niobate. The low energy requirements of the work presented here suggests that this is a promising approach for spectral broadening and  $f_{\text{ceo}}$  detection.

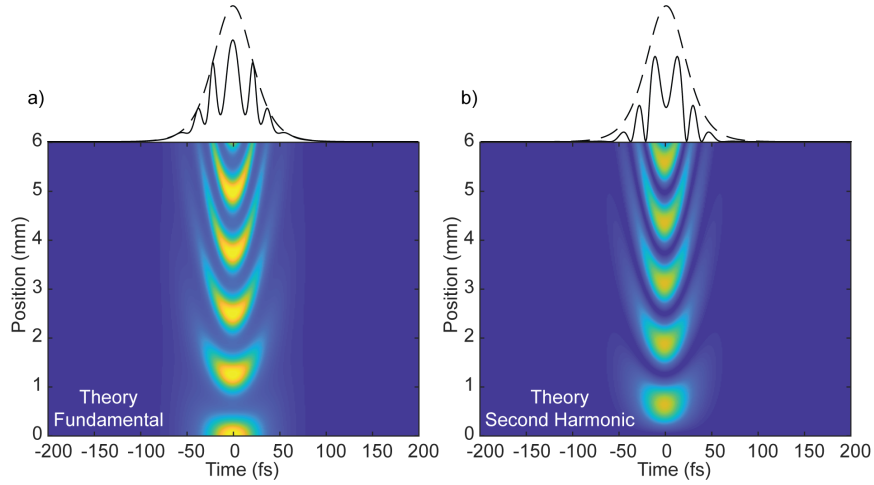


Figure 3.14: Theoretical evolution of a) the fundamental,  $|A_\omega|^2$  and b) the second harmonic  $|A_{2\omega}|^2$ . Dotted lines show the in-coupled fundamental pulse, and solid lines show the resulting pulse at the output of the waveguide for each harmonic.

### 3.6 Saturation Broadening in Nanophotonic PPLN Devices

In this section we develop a heuristic model for the evolution of the fundamental and second harmonic presented in Sec. 3.5. This model is motivated by several observations: i) the observed coherence for large soliton number suggests that the spectral broadening mechanisms may be different than an effective  $\chi^{(3)}$ , ii) the observed relative intensity of the second harmonic violates the assumption of an undepleted fundamental, iii) the amount of  $k''_\omega$  at the fundamental too small to cause significant self-focusing,  $L \sim z_D/20$  where  $z_D = 2\tau^2/k''_\omega$  is the characteristic dispersion length, and iv) the regular patterning of the spectra in Fig. 3.12, with sharp dips forming as the pulse energy is increased, is highly unusual for conventional SCG based on soliton fission. Based on these observations, and relatively small magnitude of all of the waveguide dispersion orders, we propose a model that accounts for saturation and neglects dispersion to arbitrary order. In this limit, the coupled wave equations are given by

$$\partial_z A_\omega(z, t) = -i\kappa A_{2\omega} A_\omega^* \exp(-i\Delta k z), \quad (3.11a)$$

$$\partial_z A_{2\omega}(z, t) = -i\kappa A_\omega^2 \exp(i\Delta k z). \quad (3.11b)$$

Eqns. 3.11a-3.11b may be solved for the local field intensity at each point in time using the Jacobi-Elliptic functions associated with CW SHG in the limit of a depleted pump[95]. The local instantaneous power of the fundamental and second harmonic are given by

$$|A_\omega(z, t)|^2 = (1 - \eta^2(z, t)) |A_\omega(0, t)|^2,$$

$$|A_{2\omega}(z, t)|^2 = \eta^2(z, t) |A_\omega(0, t)|^2,$$

where the instantaneous field conversion efficiency is given by  $\eta(z, t) = \nu(t) \text{sn}(\kappa A_\omega(0, t) z / \nu(t) | \nu^4(t))$ , the Jacobi elliptic sine is sn, and  $\nu(t) = \Delta k / (4\kappa A_\omega(0, t)) - \sqrt{1 + (\Delta k / (4\kappa A_\omega(0, t)))^2}$ .

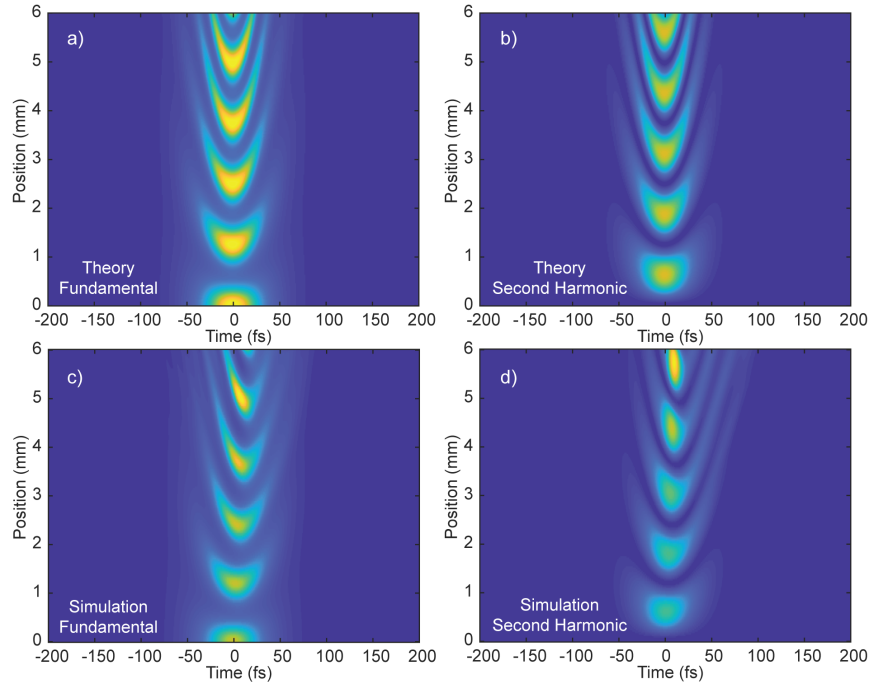


Figure 3.15: Comparison of theory with a full split-step Fourier simulation. a) Theoretical fundamental, b) theoretical second harmonic, c) simulated fundamental, and d) simulated second harmonic.

The Jacobi elliptic solutions found here bear many similarities to the sine-wave evolution that occurs during undepleted phase-mismatched SHG, namely, periodic oscillations of the fundamental and second harmonic power in  $z$ , and a conversion efficiency that increases with increasing pump power. However, the Jacobi-elliptic functions saturate at high power and exhibit a spatial period for back-conversion, hereafter referred to as the conversion period, that depends on the local field intensity. The resulting theoretical evolution of a short pulse in the 6-mm-long waveguides studied in Sec. 3.5 is shown in Fig. 3.14(a-b). Near the peak of the pulse the conversion period is the shortest and both harmonics undergo  $\sim 5$  conversion periods as the field propagates through the

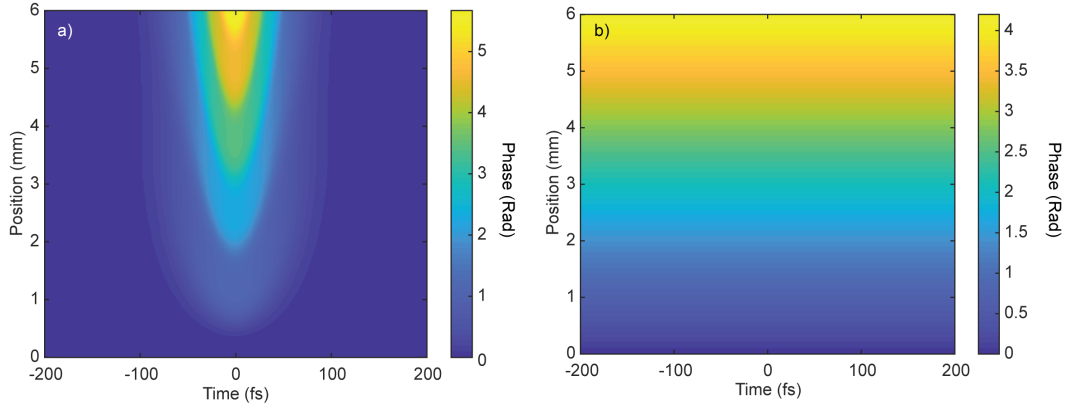


Figure 3.16: Theoretical phase of a) the fundamental and b) the second harmonic. The fundamental forms plateaus of  $\sim$  constant phase in time, and the second harmonic exhibits a phase that is independent of time.

waveguide. The oscillations in the tails of the pulse asymptotically approach a conversion period given by twice the coherence length associated with the phase-mismatch between the two harmonics,  $2z_{\text{coh}} = 2\pi/\Delta k = 2L/3$ . Remarkably, the peak undergoes more than three times as many oscillations as the tails of the pulse, which gives rise to a pulse shape with rapid amplitude variations as each part of the pulse cycles through a different number of conversion periods (Fig. 3.14, solid lines).

We now verify this analytic model against the full split-step Fourier model studied in Sec. 3.5 using the time-domain instantaneous power,  $|A_\omega|^2$  and  $|A_{2\omega}|^2$ . The results are shown in Fig. 3.15. While the simulated pulse envelopes do exhibit some distortion due to higher order dispersion, the key aspects of our Jacobi-elliptic approach such as the rapid amplitude modulations of the resulting pulses are largely preserved. Given this strong agreement, we now consider the phase evolution and spectral broadening of the harmonics.

Using the same quasi-static heuristic, the Jacobi elliptic solutions can be shown to predict phase envelopes for the fundamental and second harmonic,

$$\phi_\omega(z, t) = \frac{\Delta k}{2} \int_0^z \frac{\eta^2(z', t)}{1 - \eta^2(z', t)} dz',$$

$$\phi_{2\omega}(z, t) = \frac{\Delta k}{2} z,$$

respectively, and are plotted in Fig. 3.16. The rate of phase accumulation by the fundamental depends strongly on the degree of pump depletion, with large phase shifts accumulated at values of  $z$  and  $t$  that correspond to large  $\eta(z, t)$ . Remarkably, this behavior results in a saturable effective SPM for the fundamental, with the total accumulated phase plateauing across large time bins (Fig. 3.16(a)). The phase of the second harmonic is independent of time, and therefore can be neglected in the context of spectral broadening. These two behaviors suggest that the predominant broadening

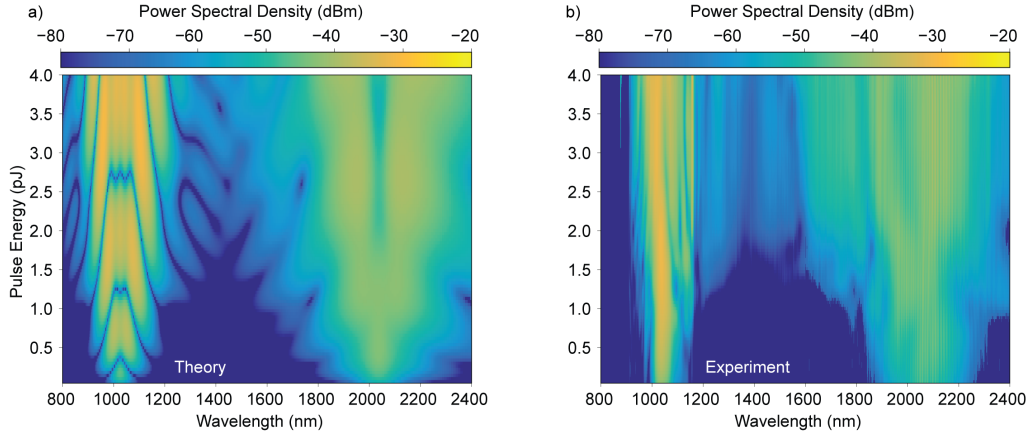


Figure 3.17: Comparison of a) theoretical and b) experimental power spectral density for phase-mismatched SHG in the saturated limit.

mechanisms for saturated SHG are not effective SPM. Instead, the observed spectral broadening of the harmonics is dominated by the rapid amplitude modulations in time accumulated by each pulse.

Having calculated both the amplitude and phase of each envelope, we may now Fourier transform these envelopes numerically to study the evolution of the power spectral density. The combined power spectral density associated with each harmonic,  $|\hat{A}_\omega(L, \Omega)|^2 + |\hat{A}_{2\omega}(L, \Omega)|^2$  is plotted in Fig. 3.17(a) as a function of pulse energy coupled into the waveguide, and compared to our experimental results in Fig. 3.17(b). The two spectra show reasonable agreement, with each harmonic broadening for pulse energies in excess of 1-pJ, and both harmonics merging together for pulse energies  $> 2$ -pJ. Deviations between the spectra for wavelengths shorter than 900-nm may be due to the avoided mode-crossing in this range, which strongly perturbs the dispersion of the waveguide mode.

Finally, we consider the carrier-envelope-offset beatnotes of these two harmonics. The beatnote power contained in each spectral bin is calculated using  $2\text{Re}\left(\hat{A}_\omega(L, \Omega)\hat{A}_{2\omega}^*(L, \Omega)\right)$ . Fig. 3.18 shows the calculated  $f_{\text{ceo}}$  beatnote current for the overlapping spectra as a function of pulse energy and wavelength. We note here that for a suitable choice of pulse energy, e.g. 3-, 3.5-, or 4-pJ, the  $f_{\text{ceo}}$  beatnotes remain in-phase across nearly a micron of bandwidth. This behavior simplifies  $f_{\text{ceo}}$  detection by allowing the output of the waveguide to be focused on a photoreceiver with minimal filtering, and improves the detected beatnote power by integrating the photocurrent over many comb lines. Furthermore, this periodic re-phasing of the beatnotes with pump power explains why we were able to obtain bright  $f_{\text{ceo}}$  beatnotes across a large optical bandwidth in Sec. 3.5.

We close this section by noting that the dynamical processes discussed here represent a completely new approach to spectral broadening and supercontinuum generation. In contrast with the effective self-phase modulation that occurs in the cascaded limit, here spectral broadening occurs due to rapid amplitude modulations across the pulse envelope of the fundamental and second harmonic.

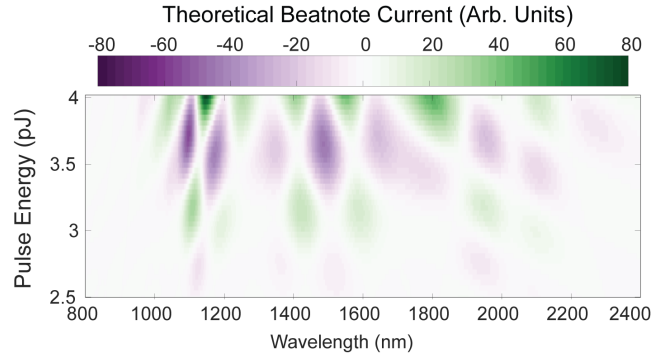


Figure 3.18: Beatnote photocurrent as a function of wavelength and pulse energy coupled into the waveguide. For in-coupled pulse energies of 3-, 3.5-, and 4-pJ, the generated beatnotes remain in-phase across 100's of nm of bandwidth.

This process allows for the generation of coherent octaves of bandwidth with record-low pulse energies. Furthermore, this process lacks many of the traditional decoherence mechanisms associated with supercontinuum generation, namely, modulation instabilities, stimulated raman scattering, and non-common-path noise. These first two processes only occur for pulse energies sufficiently strong to achieve supercontinuum generation with the pure electronic  $\chi^{(3)}$  of lithium niobate. Finally, saturation broadening can generate overlapping harmonics that interfere to produce beatnotes that remain in-phase across 100's of nm of bandwidth. This feature allows for efficient carrier-envelope-offset detection with low average powers since a larger portion of the optical bandwidth may be integrated to generate a large photocurrent.

### 3.7 Conclusions and Outlook

Nanophotonic PPLN waveguides are an extremely promising platform for nonlinear photonic devices, and the experiments shown here represent a small portion of the new devices that can be explored in this platform. The results presented throughout this chapter focused on SHG, and initial results showed that such devices exhibit CW normalized efficiencies nearly two orders of magnitude larger than state-of-the-art diffused waveguides. Then, we experimentally demonstrated both SHG and SCG in a dispersion-engineered nanophotonic PPLN waveguide. These waveguides are shown to exceed the performance of current-generation SHG devices by at least an order of magnitude in phasematching bandwidth and pulse energy requirements. Similarly, they produce multi-octave supercontinua comprised of multiple spectrally broadened harmonics with at least an order of magnitude lower pulse energies required than in previous demonstrations in lithium niobate waveguides. Remarkably, this process did not correspond to conventional self-phase modulation

based on cascaded nonlinearities, but instead amplitude modulations due to pump saturation. This dynamical regime represents a new approach to supercontinuum generation and carrier-envelope-offset detection. Finally, we note that these dramatic reductions in energy requirements are made possible by combining the dispersion engineering and large  $\eta_0$  available in nanophotonic waveguides with periodically poled  $\chi^{(2)}$  nonlinearities. When these techniques are combined they achieve highly efficient quasi-phasematched interactions with femtosecond pulses over long propagation lengths, thereby enabling a new class of nonlinear photonic devices and systems.

# Chapter 4

## Conclusions

### 4.1 Summary of this Dissertation

The two main topics addressed in this dissertation are the pulse formation mechanisms of synchronously pumped optical parametric oscillators, and second harmonic generation of femtosecond pulses in nonlinear nanophotonic devices. When studying pulse formation dynamics in OPOs, we developed heuristic models that were able to qualitatively predict the regimes of operation that occur in synchronously pumped OPOs. These regimes include non-degenerate operation, when the cavity length detuning relative to a resonance and group velocity dispersion have opposite signs, and degenerate operation when they have the same sign. The regimes of operation in degenerate OPOs were further distinguished by the timing mismatch between the pump laser and the cold-cavity round trip time, with perfect synchronization corresponding to the formation of box pulses, and long cavity resonances forming temporal simultons. We then studied the formation of temporal simultons experimentally, numerically, and analytically, and were able to show strong agreement between all of these studies. We found that the simulton regime that occurs when the OPO is not perfectly synchronized with the pump laser can yield higher conversion efficiencies than synchronous operation, and that the simulton regime exhibits a monotonic increase of the generated bandwidth with increasing pump power. This favorable scaling law allows for simulton OPOs to produce few-cycle pulses while achieving conversion efficiencies in excess of 50%.

In the context of nonlinear nanophotonic devices, we studied the dynamics of SHG in PPLN ridge waveguides driven by femtosecond pulses. We first studied phase-matched SHG in the undepleted regime, and established that the dominant dispersion orders that restrict the amount of bandwidth that can be input at the fundamental and generated at the second harmonic were determined by the group velocity dispersion of the fundamental and the temporal walk-off between the harmonics, respectively. We then showed that with a suitable choice of waveguide geometry, we may both eliminate the temporal walk-off between the fundamental and second harmonic, and suppress the

group velocity dispersion of the fundamental. This enabled an order of magnitude increase of the interaction lengths of few-cycle pulses, from  $\sim 0.5$  millimeters to  $\sim 6$  millimeters. In an experiment the fabricated waveguides achieved transfer functions that exhibited strong agreement with theory, and normalized efficiencies of  $\sim 1000\%/W\text{-cm}^2$ , which exceed the performance of previous generation diffuse waveguides 50-fold. When all of these features are combined, namely, large nonlinearities and long interaction lengths with few-cycle pulses, the fabricated waveguides were able to achieve saturated conversion efficiencies of 50% with only 60 femtojoules of in-coupled pulse energy.

We then studied phase-mismatched SHG of short pulses in the depleted regime. In this limit, we were able to develop an analytic model for the evolution of the fundamental and second harmonic pulses by adapting the Jacobi-Elliptic solutions typically associated with CW SHG. These analytic models exhibit strong agreement with experimental results, and we were able to show both experimentally and analytically that this effect may generate octaves of bandwidth at both harmonics with substantially lower pulse energies than traditional approaches based on  $\chi^{(3)}$  nonlinearities. Due to the low pulse energies involved, this method of spectral broadening appears to avoid many of the decoherence mechanisms associated with  $\chi^{(3)}$  nonlinearities, such as the noise generated by spontaneous Raman processes. Furthermore, for certain values of in-coupled pulse energy, the beatnotes produced by the interference of the two harmonics can fall in-phase across hundreds of nanometers of bandwidth. This dramatically simplifies f-2f interferometry by allowing for bright beatnotes to be detected across a broad bandwidth without the need for tunable narrowband filters, thereby simplifying any experimental realizations and producing substantially larger photocurrents. Together, these effects enabled an f-2f interferometer to be integrated into a single 6-mm-long waveguide that operated with 1 - 10 picojoules of in-coupled pulse energy, where 10's - 100's of picojoules is still common among state-of-the-art devices.

## 4.2 Future Work

In many regards the work discussed in this thesis represents the beginning of many of these topics. There is still a great deal that we do not understand about the simulton regime, including the amount of third-order dispersion needed to achieve stable simulton operation, the mechanisms that ultimately limit the bandwidth generated by an OPO operating in the simulton regime, and the operating conditions that can cause the OPO to transition to box-pulse operation for large amount of pump power. The manifold projection methods developed in Ch. 2 do not generalize well to include the chirp induced by group velocity dispersion, and therefore cannot be used to analyze the interplay of second- and third-order dispersion. Furthermore, by assuming the shape of the generated fundamental pulses these methods are not well suited for studying the transition from simulton to box-pulse operation, which exhibit rather different pulse shapes. Understanding these behaviors requires more sophisticated theoretical tools, such as Lagrangian methods[66] or the method of

moments[67].

Similarly, the treatment used here largely neglects many important spatial effects. We have only incorporated nonlinear lensing due to the large undepleted gain of the parametric amplifier. This treatment overlooks the non-trivial change in lensing that occurs during saturation, which undoubtedly determines the total conversion efficiency that the OPO can achieve above threshold. Furthermore, experimental studies have qualitatively suggested that the OPO can oscillate in many spatial modes. Often these modes are suppressed in an ad-hoc manner, where the nonlinear crystal is slightly displaced from the focus of the cavity and an intracavity iris is used to introduce loss for higher order spatial modes. The treatment used here assumes the resonant spatial modes of the OPO are predominantly fundamental Hermite-Gauss modes, neglects inter-modal scattering, and cannot make any predictions about the quality of the generated beam. To date, a full model of spatio-temporal effects in OPOs that addresses the role of nonlinear lensing in the saturated limit and the coupling between multiple resonant spatial modes has not been used to understand these behaviors in more detail.

There is, of course, an extraordinary amount of work left to be done regarding the dynamics of few-cycle pulses in nonlinear waveguides. Current work is focused on scaling the results discussed in Ch. 3 to wavelengths around 1560 nm, where pump sources are more readily accessible. Numerical simulations of the waveguide dispersion have suggested that group velocity matching may occur at wavelengths as short as 1300 nm, but many of these designs are more challenging to fabricate. Furthermore, the normalized efficiency associated with SHG in nanophotonic devices exhibits a quartic scaling with frequency. As a result, the experimental realization of group-velocity-matched SHG devices at 1560-nm should correspond to the first generation of devices that achieve SCG with 100's of femtojoules, rather than 1-10 picojoules.

There are a number of exciting future directions for this work, including developing new approaches to dispersion engineering using more complicated waveguide geometries, and co-engineering aperiodic gratings to either improve the performance of traditional devices or enable new dynamical processes entirely. Recent theoretical work has been intensely focused on the dynamical regimes of dispersion engineered PPLN resonators, with several papers suggesting that a number of new dynamical regimes corresponding to different varieties of quadratic solitons may exist in these systems[96, 97, 98]. In principle, experimental realizations of these regimes could potentially combine many of the features of Kerr microresonators, such as the ability to generate a short pulse from a resonant CW wave, with the features of simulton OPOs, such as intrinsic phase-locking between the interacting harmonics.

Finally, a natural extension of the work discussed in this thesis would be the realization of a chip-integrated synchronously pumped OPO. Assuming we can suppress the dispersion of the fundamental and the temporal walk-off using designs similar to those discussed in Ch. 3, then we may model such an OPO by assuming quasi-static interactions of short pulses. In this limit, we may

solve the coupled wave equations using the CW equations of motion for each time bin,

$$\eta(t) = \frac{4P_{\text{th}}}{|A_p(t)|^2} \left( \frac{|A_p(t)|}{\sqrt{P_{\text{th}}}} - 1 \right), \quad (4.1)$$

where  $P_{\text{th}} = \ln(R)^2 / (4\kappa^2 L^2)$ . The threshold of oscillation is determined by the peak intensity of the pulse used to drive the OPO,  $|A_p(0)| = \sqrt{U/2\tau}$ . Using somewhat ambitious experimental numbers, namely,  $R = 0.99$ ,  $L = 7$  mm,  $\kappa^2 = 6000\%/W\text{-cm}^2$ , and  $\tau = 28$  fs, corresponding to a 10-GHz ring resonator pumped by a commercially available 780-nm Ti:Sapphire, we obtain a threshold pulse energy of 0.05 aJ. For comparison, the energy associated with a single photon at 780-nm is 0.25 aJ, or five times larger. Using more conservative numbers such as  $R = 0.9$ , and the  $\kappa = 1000\%/W\text{-cm}^2$  corresponding to pumping at 1030-nm, we obtain a threshold of 32 aJ, or 166 photons. An experimental demonstration of these systems would represent the first example of quadratic nonlinear photonic devices that can achieve saturated nonlinearities at the few- or single-photon level. Further enhancements to the energy requirements of these systems may be achieved with a resonant second harmonic, which would again reduce the threshold of oscillation by a factor of  $\sim 1/(1 - R)$ . In principle, systems with such large nonlinearities may potentially be used to realize the types of behavior typically associated with strongly coupled atom-cavity systems and superconducting circuits, such as vacuum Rabi splitting[99], photon blockading[100], and Schrödinger cat states[101, 102]. While the work we have done throughout this thesis has predominantly focused on efficiently generating, frequency converting, and broadening optical frequency combs, the application of the design principles discussed here to realizing novel quantum optical systems is an extremely promising direction for the field.

## Appendix A

# The Coupled Wave Equations for Gaussian Beams

While the plane-wave approach treated in Ch. 1 is a convenient method of deriving the coupled wave equations, plane-waves never occur in a laboratory setting. A far more common case is to drive a nonlinear interaction using the Gaussian beams naturally formed in laser cavities. We treat this case here, first by considering interactions between fundamental Gaussian modes, and then by generalizing to an arbitrary admixture of Gaussian beams using the methods described in [62]. While it is possible to further generalize the methods used here to account for spatial walk-off and orbital angular momentum, our analysis is greatly simplified by assuming that all of the beams input to, and output from our nonlinear medium are azimuthally symmetric. These simplifications are often sufficient for the types of devices studied here.

We begin by considering SHG, where the fundamental harmonic input to the nonlinear medium is given by a Gaussian beam in the fundamental spatial mode,

$$E_\omega = (A_\omega(z)u_\omega(z, r) \exp(i\omega t - ik_\omega z) + c.c.) / 2, \quad (\text{A.1})$$

$$u_\omega(z, r) = \sqrt{\frac{2}{\pi w_\omega^2(z)}} \exp\left(\frac{-r^2}{w_\omega(z)^2}\right) \exp\left(-i\left(\frac{k_\omega r^2}{2R_\omega(z)} - \phi_\omega(z)\right)\right), \quad (\text{A.2})$$

where the beam parameters are given by

$$\begin{aligned} w_\omega(z) &= w_{0,\omega} \sqrt{1 + (z/z_{R,\omega})^2}, \\ R_\omega(z) &= z \left[ 1 + \left( \frac{z_{R,\omega}}{z} \right)^2 \right], \\ \phi_\omega(z) &= -\tan^{-1}(z/z_{R,\omega}), \\ z_{R,\omega} &= \pi w_{0,\omega}^2 n_\omega / \lambda. \end{aligned}$$

Here,  $w_\omega$  is the beam waist,  $R_\omega$  is the radius of curvature, and  $\phi_\omega$  is the Guoy phase. The beam profile defined by  $u_\omega(z, r)$  is normalized such that  $\int |u_\omega|^2 r dr d\theta = 1$ , and for convenience we define  $A_{\text{mode},\omega} = \pi w_{0,\omega}^2 / 2$ . The nonlinear polarization envelope generated by the fundamental has a waist given by  $2w_{2\omega}^2 = w_\omega^2$ , and the generated second harmonic has nearly the same Rayleigh length,  $z_R = 2\pi w_{2\omega}^2 n_{2\omega} / \lambda$ . Therefore, a natural choice for the generated second harmonic mode is

$$u_{2\omega}(z, r) = \sqrt{\frac{2}{\pi w_{2\omega}^2(z)}} \exp\left(\frac{-r^2}{w_{2\omega}^2(z)}\right) \exp\left(-i\left(\frac{k_{2\omega} r^2}{2R_{2\omega}(z)} - \phi_{2\omega}(z)\right)\right),$$

where all of the beam parameters used in  $u_{2\omega}$  are evaluated using  $w_{0,2\omega}$ ,  $n_{2\omega}$ , and  $\lambda/2$ . The derivation of the coupled wave equations from this choice of field distribution follows the same sequence of steps as the plane-wave case, with  $A_\omega(z)u_\omega(z, r)$  and  $A_{2\omega}(z)u_{2\omega}(z, r)$  in place of  $A_\omega(z)$  and  $A_{2\omega}(z)$ . The resulting coupled wave equations, with  $A_\omega$  normalized to units of  $W^{1/2}$ , are

$$u_\omega(z, r) \partial_z A_\omega(z) = -i\omega \chi^{(2)} \sqrt{Z_0} / (n_\omega c \sqrt{2n_{2\omega}}) A_{2\omega}(z) A_\omega^*(z) \exp(-i\Delta k z) u_{2\omega}(z, r) u_\omega^*(z, r) \quad (\text{A.4a})$$

$$u_{2\omega}(z, r) \partial_z A_{2\omega}(z) = -i\omega \chi^{(2)} \sqrt{Z_0} / (n_\omega c \sqrt{2n_{2\omega}}) A_\omega^2(z) \exp(i\Delta k z) u_\omega^2(z, r). \quad (\text{A.4b})$$

Finally, we multiply Eqn. A.4a and A.4b by  $u_\omega^*(z, r)$  and  $u_{2\omega}^*(z, r)$ , respectively, and integrate over  $r$  and  $\theta$  to find the evolution of  $A_\omega(z)$  and  $A_{2\omega}(z)$ . Assuming the two envelopes have the same Rayleigh length, we find

$$\partial_z A_\omega(z) = \frac{-i\kappa}{\sqrt{1 + (z/z_R)^2}} A_{2\omega}(z) A_\omega^*(z) \exp(-i\Delta k z) \exp(-i\phi_\omega(z)), \quad (\text{A.5a})$$

$$\partial_z A_{2\omega}(z) = \frac{-i\kappa}{\sqrt{1 + (z/z_R)^2}} A_\omega^2(z) \exp(i\Delta k z) \exp(i\phi_\omega(z)). \quad (\text{A.5b})$$

Here, the nonlinear coupling is given by  $\kappa = \omega \chi^{(2)} \sqrt{Z_0} / (n_\omega c \sqrt{2n_{2\omega} A_{\text{eff}}})$ . The effective area of the interaction is  $A_{\text{mode},\omega}^2 A_{\text{mode},2\omega} / \mathcal{O}^2$ , where  $A_{\text{mode},\omega} = \pi w_{0,\omega}^2 / 2$  is the area of the mode, and  $\mathcal{O} = \int \exp(-2r^2/w_{0,\omega}) \exp(-r^2/w_{0,2\omega}) r dr d\theta$  is the overlap of the modes. These equations resemble the coupled wave equations for plane-wave SHG, but with a nonlinear coupling that decays as

$\sqrt{1 + (z/z_R)^2}$  and a small phase-mismatch induced by the Guoy phase. For the approximations made here, these two modifications to the coupled wave equations effectively apodize the nonlinear interaction, and may be analyzed using the methods described in [36]. Finally, we note that when  $z \ll z_R$ , we recover the plane-wave coupled wave equations, with  $\Delta k = k_{2\omega} - 2k_\omega - 1/z_R$ .

We now consider the general case, where the waves are expanded in a series of Laguerre-Gaussian modes. For simplicity, we consider only the radial number,  $p$ , and ignore the azimuthal number,  $l = 0$ . This is equivalent to assuming that the beams input to and output from the nonlinear crystal are azimuthally symmetric, which is often a good approximation to the behavior observed in experiments. In this case, the field is given by

$$E_\omega = \sum_p (A_{\omega,p}(z) u_{\omega,p}(z, r) \exp(i\omega t - ik_\omega z) + c.c.) / 2, \quad (\text{A.6})$$

$$u_{\omega,p}(z, r) = L_p(2r^2/w_\omega(z)^2) u_\omega(z, r) \exp(2pi\phi_\omega(z)), \quad (\text{A.7})$$

where  $L_p$  are the Laguerre polynomials. The  $u_{\omega,p}$  satisfy an orthogonality relation,  $\int u_{\omega,l}^* u_{\omega,m} r dr d\theta = \delta_{lm}$ , where  $\delta_{lm}$  is the Kronecker delta function. Following the same steps as above, we find

$$\sum_l u_{\omega,l} \partial_z A_{\omega,l} = -i\omega \chi^{(2)} \sqrt{Z_0} / (n_\omega c \sqrt{2n_{2\omega}}) \exp(-i\Delta k z) \sum_{m,n} A_{2\omega,n} A_{\omega,m}^* u_{2\omega,n} u_{\omega,m}^* \quad (\text{A.8a})$$

$$\sum_n u_{2\omega,n} \partial_z A_{2\omega,n} = -i\omega \chi^{(2)} \sqrt{Z_0} / (n_\omega c \sqrt{2n_{2\omega}}) \exp(i\Delta k z) \sum_{l,m} A_{\omega,l} A_{\omega,m} u_{\omega,l} u_{\omega,m}, \quad (\text{A.8b})$$

and can use orthogonality to extract the evolution of each mode. We consider two illustrative cases here. First, if we assume that  $A_\omega$  is input in the fundamental Gaussian mode and remains in this mode, which is equivalent to assuming that the fundamental is undepleted, then  $\int u_{\omega,0}^2 u_{2\omega,l}^* = \delta_{l0}$ . That is,  $A_{\omega,0}$  only couples to the fundamental Gaussian mode of the second harmonic, and we recover the case discussed above. Second, if we assume that an incoupled second harmonic remains entirely in the fundamental Gaussian mode, then each of the spatial modes of  $A_{\omega,l}$  evolve as

$$\partial_z A_{\omega,l}(z) = \frac{-i\kappa \exp(-i\Delta k z)}{\sqrt{1 + (z/z_R)^2}} \sum_{m,n} \frac{(l+m)!}{l!m!2^{l+m}} A_{2\omega,0}(z) A_{\omega,m}^*(z) \exp(-2i(l+m+1/2)\phi_\omega(z)). \quad (\text{A.9})$$

This corresponds to the case where a bright second harmonic is amplifying the spatial modes of the fundamental without becoming depleted. This coupling between the modes of the fundamental causes the shape of  $E_\omega$  to change as it propagates in the nonlinear medium. Remarkably, these distortions can be well approximated as a lens that transforms  $E_\omega$  into a different fundamental Gaussian beam. This effective lensing is referred to as gain-induced diffraction, and will become important when we study high-gain optical parametric oscillators. We close this section by remarking that the full coupled-wave approach, where we place no restrictions on  $l$  and  $m$ , can incorporate both saturation and gain-induced lensing.

## A.1 Gain Induced Diffraction in OPOs

In this section we derive simple analytic models for the evolution of a degenerate signal undergoing gain-induced diffraction, where the gain is treated as a nonlinear lens which scatters light into higher order cavity modes. This effect will become significant when we study high-gain low-finesse optical parametric oscillators, where the spatial gain narrowing in the OPA contributes a power dependent loss by scattering power from the resonant TEM<sub>00</sub> mode into higher order spatial modes. The Guoy phase accumulated by these higher order modes shifts their resonances and timings from that of the TEM<sub>00</sub> mode, and the power scattered into these modes radiates out of the cavity. This effect can be comparable to the large outcoupling of the cavity and may cause significant shifts to the threshold of an OPO.

A full spatio-temporal treatment of the OPO is beyond the scope of the treatment presented here. Instead, we can account for this nonlinear loss to first order by considering the spatial gain narrowing due to an undepleted near-field pump. Under these conditions, we assume that the electric field of the signal wave is given by

$$E_\omega = (A_\omega(z, r) \exp(i\omega t - ik_\omega z) + c.c.) / 2, \quad (\text{A.10})$$

where  $A_\omega(z, r)$  corresponds to an envelope that varies slowly in  $z$ . The field envelope at the output of an OPA of length  $L$  is given by

$$A_\omega(L, r) = A_\omega(0, r) \exp\left(\gamma_0 L \exp\left(-\frac{r^2}{w_{2\omega}^2}\right)\right)$$

where  $\gamma_0$  is the small signal gain coefficient,  $w_{2\omega}$  is the pump waist, and  $w_\omega$  is the waist of the signal. The effective feedback coefficient of the cavity is given by the projection of the signal onto the amplified TEM<sub>00</sub> cavity mode

$$R(\gamma_0) = R(0) \frac{\int dr \exp\left(\gamma_0 L \exp\left(-\frac{r^2}{w_{2\omega}^2}\right)\right) \exp\left(-\frac{r^2}{w_\omega^2}\right)}{\exp(\gamma_0 L) \int dr \exp\left(-\frac{2r^2}{w_\omega^2}\right)}.$$

In the absence of gain-induced diffraction, threshold is given by  $\gamma_{\text{th}} L = -\ln\left(\sqrt{R(0)}\right)$ . With the effects of gain-induced diffraction, the condition for threshold becomes a transcendental equation  $\gamma_{\text{th}}^{\text{GID}} L = -\ln\left(\sqrt{R(\gamma_{\text{th}}^{\text{GID}})}\right)$ . As an example, for a cavity with beam waists of  $w_\omega = \sqrt{2}w_{2\omega} = 14\mu\text{m}$ , and a threshold of 120 mW corresponding to  $R(0) = 35\%$ , then gain-induced diffraction increases the threshold of the OPO to 180 mW. We close this section by noting that gain-induced diffraction largely leaves the theoretical treatment of OPOs unchanged; insights gained from assuming  $R = R(0)$  are valid, provided that the power dependence of  $R(\gamma_0)$  is properly accounted for. E.g. threshold still corresponds to the condition that the unsaturated gain balances the total loss,

$\gamma_{\text{th}}^{\text{GID}} L = -\ln\left(\sqrt{R(\gamma_{\text{th}}^{\text{GID}})}\right)$ , and perfect depletion still occurs when the unsaturated gain is twice the total loss  $\gamma_{\text{dep}}^{\text{GID}} L = -2\ln\left(\sqrt{R(\gamma_{\text{dep}}^{\text{GID}})}\right)$ . The times above threshold now becomes a nonlinear function of power,  $\sqrt{M(\gamma_0)} = \gamma_0 L / \ln\left(\sqrt{R(\gamma_0)}\right)$ .

## Appendix B

# A Brief Review of Optical Waveguide Theory

In this appendix, we review the relevant aspects of optical waveguide theory for the nonlinear devices considered throughout chapter 3. The main purpose of this section is to derive the dispersion operator,  $\hat{D}$ , for a waveguide mode and the nonlinear coupling,  $\kappa$ , between two waveguide modes. This section begins with a review of the key aspects of linear optical waveguide theory, include the derivation of waveguide modes, as well as their orthogonality relations and dispersion relations. We conclude this section by establishing the relevant mode normalization necessary to derive the nonlinear coupling between two waveguide modes. Sec. B.1 derives the nonlinear coupling between two waveguide modes, which yield the coupled wave equations for ultra-short pulses in nonlinear waveguides when combined with the dispersion relations found here.



Figure B.1: Schematic of typical ridge waveguide studied in Ch. 3, with the associated electric field  $E_{x,\mu}$  of the waveguide mode for both the fundamental (left) and second harmonic (right). The top cladding is air, the etched thin film is X-cut MgO:LN, and we approximate the 2- $\mu\text{m}$ -thick silica adhesion layer as extending to infinity.

A typical nonlinear waveguide, which comprises an LN ridge, an air top cladding, and a silica substrate, is shown in Fig. B.1, with the associated field distribution,  $H_{x,\mu}$ , of the  $\text{TE}_{00}$  mode. We note that many other cross sections are possible, including multi-layer claddings and W-shaped

ridges, but that the simple geometry shown here already allows for one to engineer a wide variety of new devices. Waveguide modes correspond to solutions of Maxwell's equations that propagate in  $z$  in the absence of a nonlinear polarization, with a dielectric constant that varies in  $x$  and  $y$ ,

$$\nabla \cdot [\bar{\epsilon}(x, y, \omega)\mathbf{E}(x, y, z, \omega)] = 0 \quad (\text{B.1a})$$

$$\nabla \cdot \mathbf{H}(x, y, z, \omega) = 0 \quad (\text{B.1b})$$

$$\nabla \times \mathbf{H}(x, y, z, \omega) = i\omega\bar{\epsilon}(x, y, \omega)\mathbf{E}(x, y, z, \omega), \quad (\text{B.1c})$$

$$\nabla \times \mathbf{E}(x, y, z, \omega) = -i\omega\mu_0\mathbf{H}(x, y, z, \omega). \quad (\text{B.1d})$$

We note that the media considered here are uniaxial, with the crystal coordinates aligned to the waveguide coordinates such that  $\bar{\epsilon}(x, y, \omega)$  is a second rank diagonal tensor

$$\bar{\epsilon}(x, y, \omega) = \begin{bmatrix} \epsilon_{xx}(x, y, \omega) & 0 & 0 \\ 0 & \epsilon_{yy}(x, y, \omega) & 0 \\ 0 & 0 & \epsilon_{zz}(x, y, \omega). \end{bmatrix} \quad (\text{B.2})$$

Throughout this section, we will use capital letters  $(X, Y, Z)$  to denote crystal coordinates, and lower-case letters  $(x, y, z)$  to denote waveguide coordinates. In typical straight waveguides, the direction of propagation ( $z$ ) is taken along the crystalline Y-axis of the lithium niobate. There are two cases of interest: X-cut lithium niobate films, which have their crystalline Z-axis aligned with the waveguide x-axis ( $\epsilon_{xx} = \epsilon_{ZZ}$ ,  $\epsilon_{yy} = \epsilon_{XX}$ ,  $\epsilon_{zz} = \epsilon_{XX}$ ) and Z-cut lithium niobate films, which have their crystalline Z-axis aligned with the waveguide y-axis ( $\epsilon_{xx} = \epsilon_{XX}$ ,  $\epsilon_{yy} = \epsilon_{ZZ}$ ,  $\epsilon_{zz} = \epsilon_{XX}$ ). This chapter will focus predominantly on TE<sub>00</sub> modes in X-cut films, which exhibit both large nonlinearities and allow for dispersion engineering at many wavelengths of interest.

Since  $\bar{\epsilon}(x, y, \omega)$  is translation-invariant in  $z$ , we may solve Maxwell's equations by expanding the fields in a series of guided modes

$$\mathbf{E}(x, y, z, \omega) = \sum_{\mu} a_{\mu}(\omega)\mathbf{E}_{\mu}(x, y, \omega)e^{-ik_{\mu}(\omega)z}, \quad (\text{B.3a})$$

$$\mathbf{H}(x, y, z, \omega) = \sum_{\mu} a_{\mu}(\omega)\mathbf{H}_{\mu}(x, y, \omega)e^{-ik_{\mu}(\omega)z}, \quad (\text{B.3b})$$

where  $a_{\mu}$  represents the component of  $\mathbf{E}$  contained in mode  $\mu$  around frequency  $\omega$ . The transverse mode profiles,  $\mathbf{E}_{\mu}$  and  $\mathbf{H}_{\mu}$ , and their associated propagation constant,  $k_{\mu}$ , may be found as solutions to an eigenvalue problem. The treatment presented here will largely follow that of [103]. To cast Maxwell's equations as an eigenvalue problem, we first combine Maxwell's curl equations into a system of homogeneous partial differential equations for the components of the magnetic field

$$\nabla \times (\bar{\epsilon}^{-1}\nabla \times \mathbf{H}_{\mu}) = \omega^2\mu_0\mathbf{H}_{\mu}. \quad (\text{B.4})$$

Then, we use  $\partial_z \mathbf{H}_\mu = -ik_\mu \mathbf{H}_\mu$  and the divergence relation  $\nabla \cdot \mathbf{H}_\mu = 0$  to reduce this to a system of equations for the transverse field components. Since  $\bar{\epsilon}$  is a diagonal tensor, Eqn. B.4 becomes

$$\partial_x^2 H_{x,\mu} + \frac{\epsilon_{yy}}{\epsilon_{zz}} \partial_y^2 H_{x,\mu} + \left(1 - \frac{\epsilon_{yy}}{\epsilon_{zz}}\right) \partial_x \partial_y H_{y,\mu} + \frac{\omega^2}{c^2} \epsilon_{yy} H_{x,\mu} = k_\mu^2 H_{x,\mu}, \quad (\text{B.5a})$$

$$\partial_y^2 H_{y,\mu} + \frac{\epsilon_{xx}}{\epsilon_{zz}} \partial_x^2 H_{y,\mu} + \left(1 - \frac{\epsilon_{xx}}{\epsilon_{zz}}\right) \partial_x \partial_y H_{x,\mu} + \frac{\omega^2}{c^2} \epsilon_{xx} H_{y,\mu} = k_\mu^2 H_{y,\mu}. \quad (\text{B.5b})$$

Eqns. B.5a-B.5b take the familiar form of an eigenvalue problem once the left hand side is expressed using matrix representations

$$A \begin{bmatrix} H_{x,\mu} \\ H_{y,\mu} \end{bmatrix} = \begin{bmatrix} A_{xx} & A_{xy} \\ A_{yx} & A_{yy} \end{bmatrix} \begin{bmatrix} H_{x,\mu} \\ H_{y,\mu} \end{bmatrix} = k_\mu^2 \begin{bmatrix} H_{x,\mu} \\ H_{y,\mu} \end{bmatrix}, \quad (\text{B.6})$$

where  $A_{xx} = \partial_x^2 + \epsilon_{yy}/\epsilon_{zz} \partial_y^2 + \omega^2 \epsilon_{yy}/c^2$  and  $A_{xy} = (1 - \epsilon_{yy}/\epsilon_{zz}) \partial_x \partial_y$ .  $A_{yy}$  and  $A_{yx}$  are obtained by interchanging the subscripts  $x$  and  $y$  in  $A_{xx}$  and  $A_{xy}$ .

The eigenmodes resulting as solutions to equation B.6 satisfy an orthogonality relation. This property of the waveguide modes will be a crucial tool throughout this section, and the following; it will be necessary both to derive the nonlinear coupling between waveguide modes, and to efficiently calculate the dispersion of the waveguide modes. We begin by considering a pair of eigenmodes,  $\mathbf{E}_1 = \mathbf{E}_\mu \exp(-ik_\mu z)$ ,  $\mathbf{H}_1 = \mathbf{H}_\mu \exp(-ik_\mu z)$ ,  $\mathbf{E}_2 = \mathbf{E}_\nu \exp(-ik_\nu z)$ , and  $\mathbf{H}_2 = \mathbf{H}_\nu \exp(-ik_\nu z)$ , such that  $\mathbf{H}_\nu$  and  $\mathbf{H}_\mu$  independently satisfy Eqn. B.6. Substituting  $\mathbf{E}_1$  and  $\mathbf{H}_1$  into Maxwell's curl equations, taking the dot product with  $-\mathbf{H}_2^*$  and  $\mathbf{E}_2^*$ , respectively, and adding them together yields

$$-\mathbf{H}_2^* \cdot (\nabla \times \mathbf{E}_1) + \mathbf{E}_2^* \cdot (\nabla \times \mathbf{H}_1) = i\omega\mu_0 \mathbf{H}_2^* \cdot \mathbf{H}_1 + i\omega\epsilon_0 \mathbf{E}_2^* \cdot \epsilon \mathbf{E}_1. \quad (\text{B.7})$$

Taking the complex conjugate of Eqn. B.7, interchanging the indices, and adding them together (assuming real  $\bar{\epsilon}$ ) yields

$$-\mathbf{H}_2^* \cdot (\nabla \times \mathbf{E}_1) + \mathbf{E}_2^* \cdot (\nabla \times \mathbf{H}_1) - \mathbf{H}_1 \cdot (\nabla \times \mathbf{E}_2^*) + \mathbf{E}_1 \cdot (\nabla \times \mathbf{H}_2^*) = 0. \quad (\text{B.8})$$

We rewrite Eqn. B.8 using  $\nabla \cdot (\mathbf{A} \times \mathbf{B}) = \mathbf{B} \cdot \nabla \times \mathbf{A} - \mathbf{A} \cdot \nabla \times \mathbf{B}$  to arrive at the complex reciprocity relation for  $\mathbf{E}_1$  and  $\mathbf{E}_2$

$$\nabla \cdot (\mathbf{E}_1 \times \mathbf{H}_2^* + \mathbf{E}_2^* \times \mathbf{H}_1) = 0. \quad (\text{B.9})$$

Substituting  $\mathbf{E}_1 = \mathbf{E}_\mu \exp(-ik_\mu z)$ ,  $\mathbf{E}_2 = \mathbf{E}_\nu \exp(-ik_\nu z)$ , integrating Eqn. B.9 over all space, and apply the divergence theorem, we find

$$i(k_\mu - k_\nu) \int (\mathbf{E}_\mu \times \mathbf{H}_\nu^* + \mathbf{E}_\nu^* \times \mathbf{H}_\mu) \cdot \hat{z} dA = 0. \quad (\text{B.10})$$

For  $\mu \neq \nu$  the integral must vanish. For  $\mu = \nu$  the integral is related to the power contained in the

mode. Applying Poynting's Theorem, we arrive at

$$\int_A \frac{1}{4} ([\mathbf{E}_\mu \times \mathbf{H}_\nu^* + \mathbf{E}_\nu^* \times \mathbf{H}_\mu] \cdot \hat{z}) dx dy = P\delta_{\mu,\nu}. \quad (\text{B.11})$$

We may simplify Eqn. B.11 by repeating the derivation where  $\mathbf{E}_2 = \mathbf{E}_{-\nu} \exp(ik_\nu z)$  is now the backwards propagating counterpart to mode  $\nu$ . In this case, equation (B.10) becomes

$$i(k_\mu + k_\nu) \int ((\mathbf{E}_\mu \times \mathbf{H}_\nu^* - \mathbf{E}_\nu^* \times \mathbf{H}_\mu) \cdot \hat{z}) dA = 0. \quad (\text{B.12})$$

Combining equations B.10 and B.12 yields the orthogonality relation between modes  $\mu$  and  $\nu$

$$\int_A \frac{1}{2} \text{Re}([\mathbf{E}_\mu \times \mathbf{H}_\nu^*] \cdot \hat{z}) dx dy = \int_A \frac{1}{2} \text{Re}([\mathbf{E}_\nu^* \times \mathbf{H}_\mu] \cdot \hat{z}) dx dy = P\delta_{\mu,\nu}. \quad (\text{B.13})$$

The fields, as defined, are normalized such that  $P = 1 \text{ W}$ , and therefore the power contained in mode  $\mu$  is  $P|a_\mu|^2$ . For deriving the nonlinear coupling between two modes, it's convenient to express these mode profiles using dimensionless functions  $e(x, y)$  and  $h(x, y)$

$$\mathbf{E}_\mu(x, y) = \sqrt{\frac{2Z_0P}{n_\mu A_{\text{mode},\mu}}} \mathbf{e}_\mu(x, y), \quad (\text{B.14a})$$

$$\mathbf{H}_\mu(x, y) = \sqrt{\frac{2n_\mu P}{Z_0 A_{\text{mode},\mu}}} \mathbf{h}_\mu(x, y), \quad (\text{B.14b})$$

where  $n_\mu$  is the effective index of mode  $\mu$ , and  $Z_0$  is the impedance of free space. The peak value of  $(\mathbf{e}_\mu \times \mathbf{h}_\mu^*) \cdot \hat{z}$  is chosen to be unity. As a consequence of Eqn. (B.13), the area of mode  $\mu$  is given by  $A_{\text{mode},\mu} = \int \text{Re}(\mathbf{e}_\mu \times \mathbf{h}_\mu^*) \cdot \hat{z} dx dy$ . The modal area is a measure of how tightly confined a mode is and largely determines the strength of nonlinear interactions, with more tightly confined modes producing stronger nonlinear couplings.

Before we discuss the numerical calculation of the eigenmodes we briefly remark on their symmetry properties, which often allow for a number of analytical and numerical simplifications. Most of these properties are discussed in [77], and we summarize them here. First, we note that for each mode  $\mu$ , there is a backwards propagating mode  $-\mu$ , such that  $k_\mu = -k_{-\mu}$ . The fields associated with the backward propagating mode are related to those of the forward propagating mode by the following relationships:

$$H_{x,-\mu} = -H_{x,\mu} \quad E_{x,-\mu} = E_{x,\mu} \quad (\text{B.15a})$$

$$H_{y,-\mu} = -H_{y,\mu} \quad E_{y,-\mu} = E_{y,\mu} \quad (\text{B.15b})$$

$$H_{z,-\mu} = H_{z,\mu} \quad E_{z,-\mu} = -E_{z,\mu}. \quad (\text{B.15c})$$

The waveguides under study throughout this chapter are also well approximated as lossless. In this case, the dielectric tensor is real and symmetric, and assuming the dielectric tensor is also diagonal, we may always choose the field components of the bound modes to satisfy the following convention:

$$H_{x,\mu}, E_{x,\mu}, H_{y,\mu}, E_{y,\mu} \in \text{Real} \quad (\text{B.16a})$$

$$H_{z,\mu}, E_{z,\mu} \in \text{Imaginary}. \quad (\text{B.16b})$$

Finally, all of the waveguides presented here have an axis of symmetry in their cross-section,  $\bar{\epsilon}(x, y, \omega) = \bar{\epsilon}(-x, y, \omega)$ . As a result,  $E_x$ ,  $H_y$ , and  $H_z$  all share the same parity. Similarly,  $H_x$ ,  $E_y$ , and  $E_z$  all share the same parity. This allows us to heuristically describe the modes as TE-like and TM-like, as with a planar waveguide. For a  $\text{TE}_{mn}$  mode, in which the field is predominantly polarized along the waveguide x-axis, the parity of  $E_x$  is the same as the evenness of  $m$ , e.g., for a  $\text{TE}_{00}$  mode  $E_x(-x, y) = E_x(x, y)$ , while for a  $\text{TE}_{10}$  mode  $E_x(-x, y) = -E_x(x, y)$ .

To solve Eqn. B.6 numerically, we discretise the transverse coordinates  $x$  and  $y$  using  $n_x$  and  $n_y$  grid points, respectively. We represent the magnetic field,  $H_{x,\mu}$ , using a vector

$$\bar{H}_{x,\mu} = [H_{x,\mu}(x_1, y_1), H_{x,\mu}(x_2, y_1), \dots, H_{x,\mu}(x_{n_x}, y_1), H_{x,\mu}(x_1, y_2), \dots, H_{x,\mu}(x_{n_x}, y_{n_y})]^T. \quad (\text{B.17})$$

A similar expression,  $\bar{H}_{y,\mu}$ , can be defined for  $H_{y,\mu}$ . The spatial derivatives  $\partial_x$  and  $\partial_y$  may be represented using centered finite differences, thereby converting the linear operators  $A_{xx}$ ,  $A_{xy}$ ,  $A_{yx}$ , and  $A_{yy}$  to N-by-N sparse matrices  $\bar{A}_{xx}$ ,  $\bar{A}_{xy}$ ,  $\bar{A}_{yx}$ , and  $\bar{A}_{yy}$ , where  $N = n_x n_y$ . We note that the form of equation B.6 is unchanged by this process,

$$\bar{A} \begin{bmatrix} \bar{H}_{x,\mu} \\ \bar{H}_{y,\mu} \end{bmatrix} = \begin{bmatrix} \bar{A}_{xx} & \bar{A}_{xy} \\ \bar{A}_{yx} & \bar{A}_{yy} \end{bmatrix} \begin{bmatrix} \bar{H}_{x,\mu} \\ \bar{H}_{y,\mu} \end{bmatrix} = k_\mu^2 \begin{bmatrix} \bar{H}_{x,\mu} \\ \bar{H}_{y,\mu} \end{bmatrix}, \quad (\text{B.18})$$

except that the matrix representation  $\bar{H}_{x,\mu}$  is a real vector, whereas the field  $H_{x,\mu}$  is a real function of space. Throughout the remainder of this section, barred variables will be used to denote matrix representations. The fields  $\bar{H}_{x,\mu}$  and  $\bar{H}_{y,\mu}$ , and their associated propagation constant  $k_\mu$ , may be found efficiently using standard eigenvalue solvers.

The operator  $A$  is not self-adjoint and therefore admits a distinct set of left-eigenmodes, which we will refer to as  $L_{x,\mu}$  and  $L_{y,\mu}$ ,

$$\bar{A}^\dagger \begin{bmatrix} \bar{L}_{x,\mu} \\ \bar{L}_{y,\mu} \end{bmatrix} = (k_\mu^2)^* \begin{bmatrix} \bar{L}_{x,\mu} \\ \bar{L}_{y,\mu} \end{bmatrix}. \quad (\text{B.19})$$

$L_{x,\mu}$  and  $L_{y,\mu}$  are related to the electric fields associated with the waveguide mode,  $E_{y,\mu}$  and  $E_{x,\mu}$ , respectively. The eigenvectors ( $\bar{H}_\mu = [\bar{H}_{x,\mu}, \bar{H}_{y,\mu}]^T$ ) and their associated left-eigenvectors ( $\bar{L}_\mu =$

$[\bar{L}_{x,\mu}, \bar{L}_{y,\mu}]^T$ ) form a biorthogonal system,

$$\bar{L}_\nu^\dagger \bar{H}_\mu = \delta_{\mu,\nu}, \quad (\text{B.20})$$

where  $\delta_{i,j}$  is the Kronecker delta. We remark here that the orthogonality relation established here, Eqn. B.20, is the same as that derived using Maxwell's equations, Eqn. B.13. This correspondence allows us to establish the relationship between  $L_\mu$  and the electric fields associated with mode  $\mu$ . We begin by approximating Eqn. B.13 as a Riemann sum,

$$\int \frac{1}{2} \text{Re}([\mathbf{E}_\nu^* \times \mathbf{H}_\mu] \cdot \hat{z}) dx dy \rightarrow \frac{1}{2} \left( [-\bar{E}_{y,\nu}^*, \bar{E}_{x,\nu}^*] \begin{bmatrix} \bar{H}_{x,\mu} \\ \bar{H}_{y,\mu} \end{bmatrix} \right) \Delta x \Delta y. \quad (\text{B.21})$$

Equating the two orthogonality relations we have

$$\bar{L}_\nu^\dagger \bar{H}_\mu = \frac{1}{2} \left( [-\bar{E}_{y,\nu}^*, \bar{E}_{x,\nu}^*] \begin{bmatrix} \bar{H}_{x,\mu} \\ \bar{H}_{y,\mu} \end{bmatrix} \right) \Delta x \Delta y, \quad (\text{B.22})$$

which implies  $\bar{L}_\nu = [-\bar{E}_{y,\nu}, \bar{E}_{x,\nu}]^T \Delta x \Delta y / 2$ .

The orthogonality relations established above act as projection operators that enable a number of useful computational techniques. For notational simplicity, we use the matrix representations throughout the remainder of this section. First, we remark that the projection operator,  $L_\mu$ , is a powerful computational tool for calculating the dispersion orders of mode  $\mu$ . Given  $\bar{L}_\nu$ ,  $\bar{H}_\mu$ , and the matrix representation of Maxwell's equations,  $\bar{A}$ , the dispersion orders of the waveguide may be evaluated using the Hellmann-Feynman theorem,

$$\frac{\bar{L}_\mu^\dagger (\partial_\omega^n \bar{A}) \bar{H}_\mu}{\bar{L}_\mu^\dagger \bar{H}_\mu} = \partial_\omega^n (k_\mu^2). \quad (\text{B.23})$$

This allows us solve for the dispersion operator,  $\hat{D}_\mu$ , to arbitrary order for mode  $\mu$  by solving two eigenvalue problems instead of solving for  $k_\mu(\omega)$  across many frequencies.

Having established orthogonality relations for waveguide modes and how to calculate the dispersion operator,  $\hat{D}_\mu$ , we are now equipped to derive the nonlinear coupling between two waveguide modes. When combined with the dispersion relations found here these results yield the coupled wave equations for SHG in the nanophotonic waveguides studied throughout Ch. 3.

## B.1 The Coupled Wave Equations in Nonlinear Waveguides

In this section, we derive the nonlinear coupling between two waveguide modes and define the effective area,  $A_{\text{eff}}$ , associated with these interactions. The effective area provides a measure of the

strength of a nonlinear interaction due to the tight confinement of the waveguide; small effective areas correspond to large field intensities and large normalized efficiencies. We focus on the case of SHG in a nonlinear waveguide, but the results presented here are easily generalized to three wave interactions. The treatment used here accounts for the fully-vectorial nature of the modes[78, 79], with each field component of the waveguide mode coupled together by the full nonlinear tensor,  $d_{ijk}$ , of the media that comprise the waveguide. Remarkably, these equations have the same form as the coupled wave equations for SHG in much simpler contexts, such as SHG of plane waves and paraxial gaussian beams. The effective area arises naturally when calculating the normalized conversion efficiency of the power in the second harmonic,  $P_{2\omega}/P_\omega$ .

The presence of a nonlinear polarization at frequency  $\omega$  gives rise to driving terms that cause the content of each mode,  $a_\mu$ , to evolve in  $z$ . The derivation of the coupled wave equations under the influence of a nonlinear polarization mirrors that of the orthogonality relations in the previous section, where Maxwell's equations now include the nonlinear polarization,

$$\nabla \times \mathbf{H}(x, y, z, \omega) = i\omega\bar{\epsilon}(x, y, \omega)\mathbf{E}(x, y, z, \omega) + i\omega\mathbf{P}_{\text{NL}}(x, y, \omega). \quad (\text{B.24})$$

Repeating the previous derivation, Eqn. (B.9) becomes

$$\nabla \cdot (\mathbf{E}_1 \times \mathbf{H}_2^* + \mathbf{E}_2^* \times \mathbf{H}_1) = -(i\omega\mathbf{E}_2^* \cdot \mathbf{P}_{\text{NL},1} - i\omega\mathbf{E}_1^* \cdot \mathbf{P}_{\text{NL},2}). \quad (\text{B.25})$$

We now select a pair of modes  $\mathbf{E}_1 = a_\mu(z)\mathbf{E}_\mu(x, y)\exp(-ik_\mu z)$ ,  $\mathbf{E}_2 = a_\nu\mathbf{E}_\nu(x, y)\exp(-ik_\nu z)$ , and integrate over all space. Using the orthogonality relations, we find that  $a_\mu$  evolves as

$$\partial_z a_\mu(z, \omega) = \frac{-i\omega}{4P} e^{ik_\mu z} \int \mathbf{E}_\mu^* \cdot \mathbf{P}_{\text{NL},2} dx dy. \quad (\text{B.26})$$

For second-harmonic generation in the limit where one pair of modes is close to phasematching, we consider one mode for the fundamental at frequency  $\omega$  and for the second harmonic at frequency  $2\omega$  without loss of generality. For the remainder of this section, the modes under consideration will be referred to as  $a_\omega$  and  $a_{2\omega}$  for the fundamental and second harmonic, respectively. In this case, the nonlinear polarization is given by

$$\mathbf{P}_{\text{NL},\omega} = 2\epsilon_0 d_{\text{eff}} a_{2\omega} a_\omega^* \sum_{jk} \bar{d}_{ijk} E_{j,2\omega} E_{k,\omega}^* e^{-i(k_{2\omega}-k_\omega)z} \quad (\text{B.27a})$$

$$\mathbf{P}_{\text{NL},2\omega} = \epsilon_0 d_{\text{eff}} a_\omega^2 \sum_{jk} \bar{d}_{ijk} E_{j,\omega} E_{k,\omega} e^{-2ik_\omega z} \quad (\text{B.27b})$$

where  $i, j, k \in \{x, y, z\}$ .  $d_{\text{eff}} = \frac{2}{\pi} d_{33}$  is the effective nonlinear coefficient for a 50% duty cycle periodically poled waveguide, and  $\bar{d}_{ijk}$  is the normalized  $\chi^{(2)}$  tensor. For lithium niobate, this is

expressed using contracted notation[80] in the coordinates of the crystal as

$$\bar{d}_{iJ} = \frac{1}{d_{33}} \begin{bmatrix} 0 & 0 & 0 & 0 & d_{15} & d_{16} \\ d_{16} & -d_{16} & 0 & d_{15} & 0 & 0 \\ d_{15} & d_{15} & d_{33} & 0 & 0 & 0 \end{bmatrix}$$

where  $d_{15} = 3.67$  pm/V,  $d_{16} = 1.78$  pm/V, and  $d_{33} = 20.5$  pm/V for SHG of 2- $\mu\text{m}$  light. These values are found using a least squares fit of Miller's delta scaling to the values reported in [81, 82], and have relative uncertainties of  $\pm 5\%$ . We therefore expect a relative uncertainty in any calculated normalized efficiency to be  $\pm 10\%$ .

We arrive at the coupled wave equations for SHG by substituting Eqns. (B.27a-B.27b) into Eqn. (B.26) and defining  $A_\omega = \sqrt{P}a_\omega$

$$\partial_z A_\omega = -i\kappa A_{2\omega} A_\omega^* e^{-i\Delta kz} \quad (\text{B.28a})$$

$$\partial_z A_{2\omega} = -i\kappa^* A_\omega^2 e^{i\Delta kz} \quad (\text{B.28b})$$

We remark here that the coupling coefficient  $\kappa$  is complex in a nanophotonic waveguide. This is due to coupling between the purely real transverse components of the fields associated with the waveguide mode with the purely imaginary z-component of the fields.  $\phi_\kappa$  ultimately contributes a constant phase shift to the nonlinear process. For example, the second harmonic generated in the presence of a complex  $\kappa$  will have a phase of  $-\pi/2 - \phi_\kappa$  relative to the fundamental.  $\kappa$  and the associated effective area are given by

$$\kappa = \frac{\sqrt{2Z_0}\omega d_{\text{eff}}}{cn_\omega \sqrt{A_{\text{eff}} n_{2\omega}}} \exp(-i\phi_\kappa) \quad (\text{B.29a})$$

$$A_{\text{eff}} = \frac{A_{\text{mode},\omega}^2 A_{\text{mode},2\omega}}{\left| \int \sum_{i,j,k} \bar{d}_{ijk} e_{i,2\omega}^* e_{j,\omega} e_{k,\omega} dx dy \right|^2} \quad (\text{B.29b})$$

For most waveguide modes under consideration in this thesis  $\phi_\kappa$ , which is given by the phase of the overlap integral in Eqn. (B.29b), is small or zero. As an example, we consider SHG in which both  $e_\omega$  and  $e_{2\omega}$  correspond to  $\text{TE}_{00}$  modes. In this case,  $e_x$  is even, and both  $e_y$  and  $e_z$  are odd. In this case, all of the  $d_{ijk} e_{i,\omega} e_{j,\omega} e_{k,2\omega}$  terms that contribute an imaginary component to the overlap integral ( $d_{16} e_{y,\omega}^2 e_{z,2\omega}^*$ ,  $d_{16} e_{z,\omega} e_{y,\omega} e_{y,2\omega}^*$ , and  $-d_{16} e_{z,\omega}^2 e_{z,2\omega}^*$ ) have odd parity and integrate to zero. However for SHG in which  $e_{2\omega}$  corresponds to a  $\text{TM}_{00}$  mode, all of these terms have even parity, and contribute a nonzero phase shift to the overlap integral. This nonzero phase of the nonlinear coefficient imparts a small phase shift between each of the interacting envelopes, but does not contribute any meaningful change in the resulting nonlinear dynamics. We can remove this phase from the coupled wave equations by phase-shifting the second harmonic,  $A_{2\omega}(z, t) \rightarrow A_{2\omega}(z, t) \exp(-i\phi_k)$ .

Eqns. B.28a-B.28b, with  $\hat{D}$  evaluated using Eqn. B.23 in principle contain all of the properties

of the waveguides mode necessary to understand the nonlinear behavior of nanophotonic devices. The dynamics described by the associated coupled wave equations (Eqns. 1.31a-1.31b) are the topic of chapter 3.

# Bibliography

- [1] H. A. Haus, “Mode-locking of lasers,” *IEEE J. Sel. Top. Quantum Electron.* 6, 1173 (2000)
- [2] P. Grelu, and N. Akhmediev, “Dissipative solitons for mode-locked lasers,” *Nature Photonics* 6, 84-92 (2012)
- [3] S. A. Diddams, “The evolving optical frequency comb [Invited],” *J. Opt. Soc. Am. B* 27, B51-B62 (2010)
- [4] I. Coddington, N. Newbury, and W. Swann, “Dual-comb spectroscopy,” *Optica* 3, 414-426 (2016)
- [5] N. Picqué and T. W. Hänsch, “Frequency comb spectroscopy,” *Nature Photonics* 13, 146157 (2019)
- [6] M. Suh, X. Yi, Y. Lai, S. Leifer, I. S. Grudinin, G. Vasisht, E. C. Martin, M. P. Fitzgerald, G. Doppmann, J. Wang, D. Mawet, S. B. Papp, S. A. Diddams, C. Beichman, and K. Vahala, “Searching for exoplanets using a microresonator astrocomb,” *Nature Photonics* 13, 2530 (2019)
- [7] T. Kato, H. Ishii, K. Terada, T. Morito, K. Minoshima, “Fully non-scanning three-dimensional imaging using an all-optical Hilbert transform enabled by an optical frequency comb,” *arXiv:2006.07801* (2020)
- [8] P. Marin, J. N. Kemal, M Karpov, A Kordts, J Pfele, M. H. P. Pfeiffer, P. Trocha, S. Wolf, V. Brasch, M. H. Anderson, R. Rosenberger, K. Vijayan, W. Freude, T. J. Kippenberg, and C. Koos, “Microresonator-based solitons for massively parallel coherent optical communications,” *Nature* 546, 274-279 (2017)
- [9] M. Hentschel, R. Kienberger, Ch. Spielmann, G. A. Reider, N. Milosevic, T. Brabec, P. Corkum, U. Heinzmann, M. Drescher, and F. Krausz, “Attosecond metrology,” *Nature* 414, 509-513 (2001)
- [10] P. Corkum, and F. Krausz, “Attosecond Science,” *Nature Physics* 3, 381-387 (2007)

- [11] S. A. Diddams, L. Hollberg, L. S. Ma, and L. Robertsson, “Femtosecond-laser-based optical clockwork with instability  $\leq 6.3 \times 10^{-16}$  in 1 s,” *Opt. Lett.* 27, 58-60 (2002)
- [12] R. N. Bracewell, “The Fourier Transform and Its Applications,” McGraw-Hill (1986)
- [13] A. Schliesser, N. Picque, and T. W. Hansch, “Mid-Infrared frequency combs,” *Nature Photonics* 6, 440-449 (2012)
- [14] C. Wang and P. Sahay, “Breath Analysis Using Laser Spectroscopic Techniques: Breath Biomarkers, Spectral Fingerprints, and Detection Limits,” *Sensors* 2009, 9(10), 8230-8262 (2009)
- [15] B. Henderson, A. Khodabakhsh, M. Metsälä, I. Ventrillard, F. M. Schmidt, D. Romanini, G. A. D. Ritchie, S. te Lintel Hekkert, R. Briot, T. Risby, N. Marczin, F. J. M. Harren, and S. M. Cristescu, “Laser spectroscopy for breath analysis: towards clinical implementation,” *Applied Physics B* volume 124, (2018)
- [16] G. Imeshev and M. E. Fermann, “230-kW peak power femtosecond pulses from a high power tunable source based on amplification in Tm-doped fiber,” *Opt. Express* 13, 7424-7431 (2005)
- [17] B. Bernhardt, E. Sorokin, P. Jacquet, R. Thon, T. Becker, I. T. Sorokina, N. Picqué, and T. W. Hänsch, “Mid-infrared dual-comb spectroscopy with  $2.4 \mu\text{m}$   $\text{Cr}^{2+}:\text{ZnSe}$  femtosecond lasers,” *Appl. Phys. B* 100, 3-8 (2010)
- [18] T. Herr, V. Brasch, J. D. Jost, C. Y. Wang, N. M. Kondratiev, M. L. Gorodetsky, and T. J. Kippenberg, “Temporal solitons in optical microresonators,” *Nature Photonics* 8, 145-152 (2014)
- [19] V. Brasch, M. Geiselmann, T. Herr, G. Lihachev, M. H. P. Pfeiffer, M. L. Gorodetsky, and T. J. Kippenberg, “Photonic chipbased optical frequency comb using soliton Cherenkov radiation,” *Science* 351, 357-360 (2016).
- [20] A. G. Griffith, R. K.W. Lau, J. Cardenas, Y. Okawachi, A. Mohanty, R. Fain, Y. H. D. Lee, M. Yu, C. T. Phare, C. B. Poitras, A. L. Gaeta and M. Lipson, “Silicon-chip mid-infrared frequency comb generation” *Nature Communications* 6, 6299 (2015)
- [21] K. L. Vodopyanov, O. Levi, P. S. Kuo, T. J. Pinguet, J. S. Harris, M. M. Fejer, B. Gerard, L. Becouarn, and E. Lallier, “Optical parametric oscillation in quasi-phase-matched GaAs,” *Opt. Lett.* 29, 1912-1914 (2004)
- [22] N. Leindecker, A. Marandi, R. L. Byer, K. L. Vodopyanov, J. Jiang, I. Hartl, M. Fermann, and P. G. Schunemann, “Octave-spanning ultrafast OPO with  $2.6\text{-}6.1 \mu\text{m}$  instantaneous bandwidth pumped by femtosecond Tm-fiber laser,” *Opt. Express* 20, 7046-7053 (2012)

- [23] E. Sorokin, A. Marandi, P. G. Schunemann, M. M. Fejer, R. L. Byer, and I. T. Sorokina, “Efficient half-harmonic generation of three-optical-cycle mid-IR frequency comb around 4  $\mu\text{m}$  using OP-GaP,” *Opt. Express* 26, 9963-9971 (2018)
- [24] A. S. Mayer, C. R. Phillips, C. Langrock, A. Klenner, A. R. Johnson, K. Luke, Y. Okawachi, M. Lipson, A. L. Gaeta, M. M. Fejer, and U. Keller, “Offset-Free Gigahertz Midinfrared Frequency Comb Based on Optical Parametric Amplification in a Periodically Poled Lithium Niobate Waveguide,” *Phys. Rev. Applied* 6, 054009 (2016)
- [25] A. V. Muraviev, V. O. Smolski, Z. E. Loparo, and K. L. Vodopyanov, “Massively parallel sensing of trace molecules and their isotopologues with broadband subharmonic mid-infrared frequency combs,” *Nature Photonics* 12, 209214 (2018)
- [26] R. A. McCracken and D. T. Reid, “Few-cycle near-infrared pulses from a degenerate 1 GHz optical parametric oscillator,” *Opt. Lett.* 40, 4102-4105 (2015)
- [27] A. Marandi, K. A. Ingold, M. Jankowski, and R. L. Byer, A. Marandi, K. A. Ingold, M. Jankowski, and R. L. Byer, “Cascaded half-harmonic generation of femtosecond frequency combs in the mid-infrared,” *Optica* 3, 324-327 (2016),” *Optica* 3, 324-327 (2016)
- [28] L. E. Myers and W. R. Bosenberg, “Periodically poled lithium niobate and quasiphase-matched optical parametric oscillators,” *IEEE J. Quantum. Electron.* 33 (10): 1663-1672, (1997)
- [29] F. Adler, K. C. Cossel, M. J. Thorpe, I. Hartl, M. E. Fermann, and J. Ye, “Phase-stabilized, 1.5 W frequency comb at 2.8–4.8  $\mu\text{m}$ ,” *Opt. Lett.* 34, 1330-1332 (2009)
- [30] P. G. Schunemann, K. T. Zawilski, L. A. Pomeranz, D. J. Creeden, and P. A. Budni, “Advances in nonlinear optical crystals for mid-infrared coherent sources,” *J. Opt. Soc. Am. B* 33, D36-D43 (2016)
- [31] A. Marandi, N. C. Leindecker, V. Pervak, R. L. Byer, K. L. Vodopyanov, “Coherence properties of a broadband femtosecond mid-IR optical parametric oscillator operating at degeneracy,” *Opt. Express* 20 (7), 7255-7262 (2012)
- [32] Y. R. Shen, “The Principles of Nonlinear Optics,” Wiley-Interscience (2002)
- [33] M. M. Fejer, G.A. Magel, D.H. Jundt, and R. L. Byer, “Quasi-phase-matched second harmonic generation: tuning and tolerances,” *IEEE Journal of Quantum Electronics*, 28 (11), 2631-2654 (1992)
- [34] P. S. Kuo, “Thick film, orientation-patterned gallium arsenide for non-linear optical frequency conversion,” PhD dissertation, Stanford University, Stanford, CA, 2008.

- [35] G. D. Miller, “Periodically poled lithium niobate: modeling, fabrication, and nonlinear-optical performance,” PhD dissertation, Stanford University, Stanford, CA, 1998
- [36] C. R. Phillips, C. Langrock, D. Chang, Y. W. Lin, L. Gallmann, and M. M. Fejer, “Apodization of chirped quasi-phases-matching devices,” *J. Opt. Soc. Am. B* 30, 1551-1568 (2013)
- [37] S. R. Vangala, D. Brinegar, V. L. Tassev, and M. Snure, “Thick hydride vapor phase epitaxial growth of ZnSe on GaAs (1 0 0) vicinal and orientation patterned substrates,” *Journal of Crystal Growth*, 2019
- [38] M. L. Bortz, S. J. Field, M. M. Fejer, D. W. Nam, R. G. Waarts, and D. F. Welch, “Noncritical quasi-phase-matched second harmonic generation in an annealed proton-exchanged LiNbO<sub>3</sub> waveguide,” *IEEE Journal of Quantum Electronics* 30 (12), 2953-2960 (1994)
- [39] R. DeSalvo, D. J. Hagan, M. Sheik-Bahae, G. Stegeman, E. W. Van Stryland, and H. Vanherzeele, “Self-focusing and self-defocusing by cascaded second-order effects in KTP,” *Opt. Lett.* 17, 28-30 (1992)
- [40] C. Conti, S. Trillo, P. Di Trapani, J. Kilius, A. Bramati, S. Minardi, W. Chinaglia, and G. Valiulis, “Effective lensing effects in parametric frequency conversion,” *J. Opt. Soc. Am. B* 19, 852-859 (2002)
- [41] M. Bache, “Cascaded nonlinearities for ultrafast nonlinear optical science and applications,” DTU-Department of Photonics Engineering (2017)
- [42] G. Imeshev, M. A. Arbore, S. Kasriel, and M. M. Fejer, “Pulse shaping and compression by second-harmonic generation with quasi-phase-matching gratings in the presence of arbitrary dispersion,” *J. Opt. Soc. Am. B* 17, 1420-1437 (2000)
- [43] G. Imeshev, M. A. Arbore, M. M. Fejer, A. Galvanauskas, M. Fermann, and D. Harter, “Ultrashort-pulse second-harmonic generation with longitudinally nonuniform quasi-phase-matching gratings: pulse compression and shaping,” *J. Opt. Soc. Am. B* 17, 304-318 (2000)
- [44] G. P. Agrawal, “Nonlinear Fiber Optics,” Academic Press; 6th edition (2019)
- [45] J. M. Dudley, G. Genty, and S. Coen, “Supercontinuum generation in photonic crystal fiber,” *Rev. Mod. Phys.* 78, 1135 (2006)
- [46] N. Akhmediev and M. Karlsson, “Cherenkov radiation emitted by solitons in optical fibers,” *Phys. Rev. A* 51, 2602 (1995)
- [47] J. P. Gordon, “Theory of the soliton self-frequency shift,” *Opt. Lett.* 11, 662-664 (1986)
- [48] S. V. Chernikov, E. M. Dianov, D. J. Richardson, and D. N. Payne, “Soliton pulse compression in dispersion-decreasing fiber,” *Opt. Lett.* 18, 476-478 (1993)

- [49] Y. Kodama, and A. Hasegawa, "Nonlinear pulse propagation in a monomode dielectric guide," *IEEE Journal of Quantum Electronics* 23 (5), 510-524 (1987)
- [50] A. S. Mayer, A. Klenner, A. R. Johnson, K. Luke, M. R. E. Lamont, Y. Okawachi, M. Lipson, A. L. Gaeta, and U. Keller, "Frequency comb offset detection using supercontinuum generation in silicon nitride waveguides," *Opt. Express* 23, 15440-15451 (2015)
- [51] J. Hult, "A Fourth-Order RungeKutta in the Interaction Picture Method for Simulating Supercontinuum Generation in Optical Fibers," *J. Lightwave Technol.* 25, 3770-3775 (2007)
- [52] Rick Trebino, "Frequency-Resolved Optical Gating: The Measurement of Ultrashort Laser Pulses," Springer (2000)
- [53] S. Longhi, "Ultrashort-pulse generation in degenerate optical parametric oscillators," *Opt. Lett.* 20, 695-697 (1995)
- [54] L. A. Lugiato, C. Oldano, C. Fabre, E. Giacobino, and R. J. Horowicz, "Bistability, self-pulsing and chaos in optical parametric oscillators," *Il. Nuovo Cimento D* 10, 959 (1988)
- [55] T. Hansson, F. Leo, M. J. Erkintalo, J. Anthony, S. Coen, I. Ricciardi, M. De Rosa, and S. Wabnitz, "Single envelope equation modeling of multi-octave comb arrays in microresonators with quadratic and cubic nonlinearities," *J. Opt Soc. Am. B* 33, 1207-1215 (2016)
- [56] F. Leo, T. Hansson, I. Ricciardi, M. De Rosa, S. Coen, S. Wabnitz, and M. Erkintalo, "Walk-off-induced modulation instability, temporal pattern formation, and frequency comb generation in cavity-enhanced second-harmonic generation," *Phys. Rev. Lett.* 116, 033901 (2016)
- [57] V. Ulvila, C. R. Phillips, L. Halonen, and M. Vainio, "Frequency comb generation by a continuous-wave-pumped optical parametric oscillator based on cascading quadratic nonlinearities," *Opt. Lett.* 38, 4281-4284 (2013)
- [58] V. Ulvila, C. R. Phillips, L. Halonen, and M. Vainio, "High-power mid-infrared frequency comb from a continuous-wave-pumped bulk optical parametric oscillator," *Opt. Express*, 22, 10535-10543 (2014)
- [59] R. Hamerly, A. Marandi, M. Jankowski, M. M. Fejer, Y. Yamamoto, and H. Mabuchi, "Reduced models and design principles for half-harmonic generation in synchronously pumped optical parametric oscillators," *Phys. Rev. A* 94, 063809 (2016)
- [60] M. Jankowski, A. Marandi, C.R. Phillips, R. Hamerly, K. A. Ingold, R. L. Byer, and M. M. Fejer, "Temporal Simultons in Optical Parametric Oscillators", *Phys. Rev. Lett.* 120, 053904 (2018)

- [61] A. La Porta and R. E. Slusher, "Squeezing limits at high parametric gains," *Phys. Rev. A* 44, 2013-2022 (1991)
- [62] M. Annamalai, N. Stelmakh, M. Vasilyev, and P. Kumar, "Spatial modes of phase-sensitive parametric image amplifiers with circular and elliptical Gaussian pumps," *Opt. Express* 19, 26710-26724 (2011)
- [63] S. A. Akhmanov, A. Chirkin, K. Drabovich, A. Kovrigin, R. Khokhlov, A. Sukhorukov, "Non-stationary nonlinear optical effects and ultrashort light pulse formation," *IEEE J. Quantum Electron.* 4, 598-605 (1968)
- [64] S. Trillo, "Bright and dark solitons in second-harmonic generation," *Opt. Lett.* 21, 1111-1113 (1996)
- [65] O. Gayer, Z. Sacks, E. Galun, and A. Arie, "Temperature and wavelength dependent refractive index equations for MgO-doped congruent and stoichiometric LiNbO<sub>3</sub>," *Appl. Phys. B* 91, 343-348 (2008)
- [66] B. A. Malomed, "Variational methods in nonlinear fiber optics and related fields," *Progress in optics* (2002)
- [67] C. Jirauschek and F. Ö. Ilday, "Semianalytic theory of self-similar optical propagation and mode locking using a shape-adaptive model pulse," *Phys. Rev. A* 83, 063809 (2011)
- [68] Q. Ru, T. Kawamori, P. G. Schunemann, S. Vasilyev, S. B. Mirov, and K. L. Vodopyanov, "Two-octave-wide (3-12  $\mu\text{m}$ ) mid-infrared frequency comb produced as an optical subharmonic in a nondispersive cavity," arXiv:2007.02496 (2020)
- [69] M. Stefszky, V. Ulvila, Z. Abdallah, C. Silberhorn, and M. Vainio, "Towards optical-frequency-comb generation in continuous-wave-pumped titanium-indiffused lithium-niobate waveguide resonators," *Phys. Rev. A* 98, 053850 (2018)
- [70] S. Matsumoto, E. J. Lim, H. M. Hertz, and M. M. Fejer, "Quasiphase-matched second harmonic generation of blue light in electrically periodically-poled lithium tantalate waveguides," *Electronics Letters* 27, 22 (1991)
- [71] M. Fiorentino, S. M. Spillane, R. G. Beausoleil, T. D. Roberts, P. Battle, and M. W. Munro, "Spontaneous parametric down-conversion in periodically poled KTP waveguides and bulk crystals," *Opt. Express* 15, 7479-7488 (2007)
- [72] C. Langrock, S. Kumar, J. E. McGeehan, A. E. Willner and M. M. Fejer, "All-optical signal processing using  $\chi^{(2)}$  nonlinearities in guided-wave devices," in *Journal of Lightwave Technology*, vol. 24, no. 7, pp. 2579-2592, July 2006.

- [73] M. Zhang, C. Wang, R. Cheng, A. Shams-Ansari, and M. Lončar, “Monolithic ultra-high-Q lithium niobate microring resonator,” *Optica* 4, 1536-1537 (2017)
- [74] A. W. Bruch, X. Liu, X. Guo, J. B. Surya, Z. Gong, L. Zhang, J. Wang, J. Yan, and H. X. Tang, “17000%/W second-harmonic conversion efficiency in single-crystalline aluminum nitride ring resonators,” *Appl. Phys. Lett.* 113, 131102 (2018)
- [75] X. Liu, A. W. Bruch, Z. Gong, J. Lu, J. B. Surya, L. Zhang, J. Wang, J. Yan, and H. X. Tang, “Ultra-high-Q UV microring resonators based on a single-crystalline AlN platform,” *Optica* 5, 1279-1282 (2018)
- [76] L. Chang, A. Boes, X. Guo, D. T. Spencer, M. J. Kennedy, J. D. Peters, N. Volet, J. Chiles, A. Kowligy, N. Nader, D. D. Hickstein, E. J. Stanton, S. A. Diddams, S. B. Papp, J. E. Bowers, “Heterogeneously Integrated GaAs Waveguides on Insulator for Efficient Frequency Conversion,” *Laser and Photonics Reviews* 2018, 12, 1800149
- [77] A.W. Snyder, J.D. Love, “Optical Waveguide Theory”, Chapman and Hall, London, UK (1983)
- [78] M. M. Fejer, “Single Crystal Fibers: Growth Dynamics and Nonlinear Optical Interactions,” PhD dissertation, Stanford University, Stanford, CA, (1986)
- [79] M. Kolesik and J. V. Moloney, “Nonlinear optical pulse propagation simulation: From Maxwells to unidirectional equations,” *Phys. Rev. E* 70, 036604 (2004)
- [80] J. F. Nye, “Physical Properties of Crystals: Their Representation by Tensors and Matrices,” Oxford University Press (1985).
- [81] I. Shoji, T. Kondo, A. Kitamoto, M. Shirane, and R. Ito, “Absolute scale of second-order nonlinear-optical coefficients,” *J. Opt. Soc. Am. B* 14, 2268-2294 (1997)
- [82] M. M. Choy, and R. L. Byer, “Accurate second-order susceptibility measurements of visible and infrared nonlinear crystals,” *Phys. Rev. B* 14, 4 (1976)
- [83] C. Wang, C. Langrock, A. Marandi, M. Jankowski, M. Zhang, B. Desiatov, M. M. Fejer, and M. Lončar, “Ultrahigh-efficiency wavelength conversion in nanophotonic periodically poled lithium niobate waveguides,” *Optica* 5, 1438-1441 (2018)
- [84] D. Chang, C. Langrock, Y. W. Lin, C. R. Phillips, C. V. Bennett, and M. M. Fejer, “Complex-transfer-function analysis of optical-frequency converters,” *Opt. Lett.* 39, 5106-5109 (2014)
- [85] R. Luo, Y. He, H. Liang, M. Li, J. Ling, and Q. Lin, “Optical Parametric Generation in a Lithium Niobate Microring with Modal Phase Matching,” *Phys. Rev. Applied* 11, 034026 (2019)

- [86] L. Chang, Y. Li, N.s Volet, L. Wang, J. Peters, and J. E. Bowers, "Thin film wavelength converters for photonic integrated circuits," *Optica* 3, 531-535 (2016)
- [87] M. Jankowski, C. Langrock, B. Desiatov, A. Marandi, C. Wang, M. Zhang, C. R. Phillips, M. Lončar, and M. M. Fejer, "Ultrabroadband nonlinear optics in nanophotonic periodically poled lithium niobate waveguides," *Optica* 7, 40-46 (2020)
- [88] Z. Zheng, A. M. Weiner, K. R. Parameswaran, M. H. Chou, and M. M. Fejer, "Femtosecond second-harmonic generation in periodically poled lithium niobate waveguides with simultaneous strong pump depletion and group-velocity walk-off," *J. Opt. Soc. Am. B* 19, 839-848 (2002)
- [89] M. Bache, J. Moses, and F. W. Wise, "Scaling laws for soliton pulse compression by cascaded quadratic nonlinearities," *J. Opt. Soc. Am. B* 24, 2752-2762 (2007)
- [90] C. R. Phillips, C. Langrock, J. S. Pelc, M. M. Fejer, I. Hartl, and M. E. Fermann, "Supercontinuum generation in quasi-phaseshifted waveguides," *Opt. Express* 19, 18754-18773 (2011)
- [91] M. Sheik-Bahae, D. J. Hagan, and E. W. Van Stryland, "Dispersion and band-gap scaling of the electronic Kerr effect in solids associated with two-photon absorption," *Phys. Rev. Lett.* 65, 96 (1990)
- [92] B. Kuyken, T. Ideguchi, S. Holzner, M. Yan, T. W. Hnsch, J. Van Campenhout, P. Verheyen, S. Coen, F. Leo, Roel Baets, Gunther Roelkens, and Nathalie Picqué, "An octave-spanning mid-infrared frequency comb generated in a silicon nanophotonic wire waveguide," *Nature Communications* 6, 6310 (2015)
- [93] J. Lu, J. B. Surya, X. Liu, Y. Xu, and H. X. Tang, "Octave-spanning supercontinuum generation in nanoscale lithium niobate waveguides," *Opt. Lett.* 44, 1492-1495 (2019)
- [94] M. Yu, *et al*, "Coherent two-octave-spanning supercontinuum generation in lithium-niobate waveguides," *Opt. Lett.* 44, 1222-1225 (2019)
- [95] J. A. Armstrong, N. Bloembergen, J. Ducuing, and P. S. Pershan, "Interactions between Light Waves in a Nonlinear Dielectric," *Phys. Rev.* 127, 1918 (1962)
- [96] A. W. Bruch, X. Liu, Z. Gong, J. B. Surya, M. Li, C. L. Zou, H. X. Tang, "Pockels Soliton Microcomb," *arXiv:2004.07708* (2020)
- [97] Y. He, Q. F. Yang, J. Ling, R. Luo, H. Liang, M. Li, B. Shen, H. Wang, K. Vahala, and Q. Lin, "Self-starting bi-chromatic LiNbO<sub>3</sub> soliton microcomb," *Optica* 6, 1138-1144 (2019)
- [98] M. Nie and S. W. Huang, "Quadratic soliton mode-locked degenerate optical parametric oscillator," *Opt. Lett.* 45, 2311-2314 (2020)

- [99] G. S. Agarwal, “Strong Coupling Induced Splitting of Dynamical Response of the Optical Parametric Oscillator,” *Phys. Rev. Lett.* 73, 522 (1994)
- [100] M. Li, Y. L. Zhang, H. X. Tang, C. H. Dong, G. C. Guo, and C. L. Zou, “Photon-Photon Quantum Phase Gate in a Photonic Molecule with  $\chi^{(2)}$  Nonlinearity,” *Phys. Rev. Applied* 13, 044013 (2020)
- [101] T. Onodera, E. Ng, N. Lörch, A. Yamamura, R. Hamerly, P. L. McMahon, A. Marandi, H. Mabuchi, “Nonlinear Quantum Behavior of Ultrashort-Pulse Optical Parametric Oscillators,” arXiv:1811.10583v2 (2019)
- [102] M. D. Reid and L. Krippner, “Macroscopic quantum superposition states in nondegenerate parametric oscillation”, *Phys. Rev. A* 47, 552 (1993)
- [103] A. B. Fallahkhair, K. S. Li and T. E. Murphy, “Vector Finite Difference Modesolver for Anisotropic Dielectric Waveguides,” *J. Lightw. Technol.* 26(11) 1423-1431 (2008)